# ABSTRACT

# UNDERSTANDING BULK BEHAVIOR OF PARTICULATE MATERIALS FROM PARTICLE SCALE SIMULATIONS

**by**
**Xiaoliang Deng**

Particulate materials play an increasingly significant role in various industries, such as pharmaceutical manufacturing, food, mining, and civil engineering. The objective of this research is to better understand bulk behaviors of particulate materials from particle scale simulations.

Packing properties of assembly of particles are investigated first, focusing on the effects of particle size, surface energy, and aspect ratio on the coordination number, porosity, and packing structures. The simulation results show that particle sizes, surface energy, and aspect ratio all influence the porosity of packing to various degrees. The heterogeneous force networks within particle assembly under external compressive loading are investigated as well. The results show that coarse-coarse contacts dominate the strong network and coarse-fine contacts dominate the total network. Next, DEM models are developed to simulate the particle dynamics inside a conical screen mill (comil) and magnetically assisted impaction mixer (MAIM), both are important particle processing devices. For comil, the mean residence time (MRT), spatial distribution of particles, along with the collision dynamics between particles as well as particle and vessel geometries are examined as a function of the various operating parameters such as impeller speed, screen hole size, open area, and feed rate. The simulation results can help better understand dry coating experimental results using comil. For MAIM system, the magnetic force is incorporated into the contact model, allowing to describe the interactions between magnets.

The simulation results reveal the connections between homogeneity of mixture and particle scale variables such as size of magnets and surface energy of non-magnets. In particular, at the fixed mass ratio of magnets to non-magnets and surface energy the smaller magnets lead to better homogeneity of mixing, which is in good agreement with previously published experimental results. Last but not least, numerical simulations, along with theoretical analysis, are performed to investigate the interparticle force of dry coated particles. A model is derived and can be used to predict the probabilities of hose-host (HH), host-guest (HG), and guest-guest (GG) contacts. The results indicate that there are three different regions dominated by HH, HG, and GG contacts, respectively. Moreover, the critical SAC for the transition of HG to GG contacts is lower than previously estimated value.

In summary, particle packing, particle dynamics associated with various particle processing devices, and interparticle force of dry coated particles are investigated in this thesis. The results show that particle scale information such as coordination number, collision dynamics, and contact force between particles from simulation results can help better understand bulk properties of assembly of individual particles.

# UNDERSTANDING BULK BEHAVIOR OF PARTICULATE MATERIALS FROM PARTICLE SCALE SIMULATIONS

by
Xiaoliang Deng

A Dissertation
Submitted to the Faculty of
New Jersey Institute of Technology
in Partial Fulfillment of the Requirements for the Degree of
Doctor of Philosophy in Materials Science and Engineering

Materials Science and Engineering

January 2016

# APPROVAL PAGE

# UNDERSTANDING BULK BEHAVIOR OF PARTICULATE MATERIALS FROM PARTICLE SCALE SIMULATIONS

**Xiaoliang Deng**

Dr. Rajesh N. Davé, Dissertation Advisor Date
Distinguished Professor of Chemical, Biological and Pharmaceutical Engineering, NJIT

Dr. Ecevit Bilgili, Committee Member Date
Associate Professor of Chemical, Biological and Pharmaceutical Engineering, NJIT

Dr. Edward Dreizin, Committee Member Date
Professor of Chemical, Biological and Pharmaceutical Engineering, NJIT

Dr. N.M. Ravindra, Committee Member Date
Professor of Physics, NJIT

Dr. Xiaoyang Xu, Committee Member Date
Assistant Professor of Chemical Biological and Pharmaceutical Engineering, NJIT

# BIOGRAPHICAL SKETCH

**Author:** Xiaoliang Deng

**Degree:** Doctor of Philosophy

**Date:** January 2016

**Undergraduate and Graduate Education:**

- Doctor of Philosophy in Materials Science and Engineering,
  New Jersey Institute of Technology, Newark, NJ, 2016

- Master of Science in Condensed Physics,
  Sichuan University, Sichuan, P. R. China, 2006

- Bachelor of Science in Condensed Physics,
  HeFei University of Technology, Anhui, P. R. China, 2001

**Major:** Materials Science and Engineering

**Presentations and Publications:**

Journals:

X. Deng, R. Davé, Dynamic simulation of particle packing influenced by size, aspect ratio and surface energy, Granular Matter, 15, 2013

X. Deng, J. Scicolone, R. Davé, Discrete element method simulation of cohesive particles mixing under magnetically assisted impaction, Powder Technology, 243, 2013

X. Deng, J. Scicolone, X. Han, R. Davé, Discrete element method simulation of a conical screen mill: A continuous dry coating device, Chemical Engineering Science, 125, 2014

X. Deng, Z. Huang, W. Wang, R. Davé, Mechanical and morphological properties of fractal agglomerates of nanoparticles, Powder Technology, under review.

X. Deng, R. Davé, Breakage of fractal agglomerates, in preparation

X. Deng, R. Davé, Adhesion and friction of dry-coated particles, in preparation

X. Deng, R. Davé, Properties of force networks in jammed granular media, in preparation

Z. Huang, W. Xiong, X. Deng, S. Bhaumik, R. Davé, Improved content uniformity of a low dose blend containing a micronized drug after cohesion reduction via dry particle coating, European Journal of Pharmaceutical Sciences, in preparation.

Conference Proceedings:

X. Deng, R. Davé, J. Scicolone, The investigation of cohesive particle mixing at sub-agglomerate scale using discrete element method, AICHE, Conference Proceedings (2013).

X. Deng, J. Scicolone, X. Han, R. Davé, Particle dynamics in a conical screen mill, AICHE, Conference Proceedings (2014).

X. Deng, Z. Huang, W. Wang, R. Davé, Investigation of nano-agglomerates properties via Monte Carlo simulation, AICHE, Conference Proceedings (2014).

Z. Huang, W. Xiong, X. Deng, R. Davé, Effect of surface modified micronized acetaminophen on the content uniformity of a low dose drug blend, AICHE, Conference Proceedings (2014).

X. Deng, R. Davé, Adhesion and friction between dry coated particles, AICHE, Conference Proceedings (2015).

To my families
致家人

# ACKNOWLEDGMENT

I would like to express my sincere gratitude to my supervisor, Dr. Rajesh N. Davé, for providing me with the continuous guidance and financial support to assist me in conducting a successful research. I appreciate all of his time, energy, and ideas that he has invested during my whole process of studying for a PhD.

My special thanks to Dr. Ecevit Bilgili, Dr. Edward Dreyzin, Dr. N. M. Ravindra, and Dr. Xiaoyang Xu for accepting to serve on my committee and their helpful suggestions.

I would like to extend my acknowledgement to the members of our group: Dr. Catharina Knieke, Dr. James Scicolone, Dr. Bhavesh Kevadiya, Dr. Laila Jallo, Dr. Ramani Susarla, Dr. Daniel To, Dr. Xi Han, Dr. Christian Beck, Dr. Lauren Beach, Dr. Maxx Capece, Dr. Mohammad Azad, Dr. Anagha Bhakay, and Dr. Afolawemi Afolabi.

I am grateful to my peers: Zhonghui Huang, Meng Li, Lu Zhang, Liang Chen, Yidong Li, Kai Zhen, Anna Owasit, Kuriakose Kunnath for all your help and being great companions.  A special thanks to Scott Matthew Krull, my office-mates throughout last 4 years and 6 months. I always enjoy our little talks about everything and it is a great pleasure to have your advice on my research and other issues.

Finally, I want to express my graduate to my families. Without their help, I cannot do what I have done.

## TABLE OF CONTENTS

**Chapter** **Page**

## TABLE OF CONTENTS
## (Continued)

**Chapter** **Page**

# TABLE OF CONTENTS
(Continued)

**Chapter** **Page**

# LIST OF TABLES

# LIST OF FIGURES

**Figure** **Page**

## LIST OF FIGURES
## (Continued)

# LIST OF FIGURES
# (Continued)

**Figure** **Page**

# CHAPTER 1

# INTRODUCTION

## 1.1 Background

Particle materials play an increasingly significant role in various industries, such as pharmaceutical manufacturing, food, mining, and civil engineering. However, it remains a challenge to understand their properties since they behave differently from any of other conventional solids, liquids, and gases [1]. Macroscopic properties of particle materials are dependent on the interaction between individual particles as well as the interaction with boundaries. Therefore, it is important to achieve a fundamental understanding of bulk behavior at individual particle level.

Discrete element method (DEM) can offer useful information in understanding particle behavior, particularly, at the single particle level. DEM was first proposed by Cundall and Strack, in 1979 [2]. Nowadays, with the rapid progress of computer science and technology, it is possible to simulate the motion of large amount of particles using DEM. DEM is a powerful tool to study the motion of particles and is widely used in understanding many processes such as mixing of particles [3-9], packing of particles [10-15], and dry coating of powders [16, 17] and so on. With the help of the well-established particle contact model, the force exerted on individual particle can be calculated, then the trajectory and velocity of single particle can be obtained by numerically resolving Newton’s law of motion. Based on the dynamic information about particles, important parameters such as average number of collisions and collision energy can be calculated which can help analyze and explain the experimental results. One of the main advantages of using a DEM simulation is that it can provide the dynamic information, which is normally difficult to obtain by traditional experimental methods. Therefore, the combined DEM simulations and experimental studies have gained increased interest.

The governing equations for individual particles can be written as follow:

$$m_i \frac{d\vec{v}_i}{dt} = \sum_{j\neq i}^{k} \vec{F}_{ij} + m_i \vec{g} \tag{1.1}$$

$$I_i \frac{d\vec{\omega}_i}{dt} = \sum_{j\neq i}^{k} \vec{T}_{ij} \tag{1.2}$$

$$\vec{F}_{ij} = \vec{F}_{ij}^{n} + \vec{F}_{ij}^{t} \tag{1.3}$$

$$\vec{T}_{ij} = \vec{R}_i \times \vec{F}_{ij}^{t} - \vec{\tau}_{ij}^{r} \tag{1.4}$$

where $m_i, \vec{v}_i, \vec{\omega}_i, \vec{R}_i, I_i$ represent the mass, translational velocity, rotational velocity, vector connecting the center of particle *i* and the contact point, and the moment of inertia of particle $i$. $\vec{F}_{ij}$ is the contact force induced by particle $j$ and it can be divided into two parts: normal contact force $\vec{F}_{ij}^{n}$ and tangential contact force $\vec{F}_{ij}^{t}$. $\vec{T}_{ij}$ represents the torque induced by particle $j$ due to tangential contact force and rolling friction force($\vec{\tau}_{ij}^{r}$). The total contact force and torque are the summation over the *k* particles contacting with particle *i*. The Hertz-Mindlin contact model is used in this work to describe the interaction between particles, and particle-vessel geometry. Further details about contact model can be found in [18, 19].

DEM simulation is also capable of simulating behavior of cohesive particles, by including approximate cohesive models into the contact force. Based on the material properties, there are different types of cohesive models available, such as Johnson-Kendall-Roberts (JKR) [20], Derjaguin-Muller-Toporov (DMT) [21], and Maugis models [22]. It is well known that the JKR, DMT, and Maugis models are complementary and apply to different situations characterized by a non-dimensional transition parameter μ or $\lambda$ [23]

$$\mu = \left(\frac{R_e w^2}{E^{*2} z_0^3}\right)^{1/3} = \frac{\lambda}{1.16} \tag{1.5}$$

where $\frac{1}{R_e} = \frac{1}{r_i} + \frac{1}{r_j}$, $w$, $E^* = \left(\frac{1-v_i^2}{E_i} + \frac{1-v_j^2}{E_j}\right)^{-1}$ are equivalent radius, work of adhesion and combined elastic modulus. $z_0$ is equilibrium separation distance of the surfaces in contact ($z_0 \approx 0.165$nm) [24]. $v_i$, $v_j$, $E_i$, $E_j$ represent the Poisson's ratios, and Young's moduli of *ith* and *jth* particles. Both $\mu$ and $\lambda$ are a measure of the ratio of elastic deformation resulting from adhesion to the effective range of surface forces [25]. Johnson and Greenwood presented an adhesion map based on transition parameter $\lambda$. If $\lambda > 5.0$, the JKR model applies and if $\lambda < 0.1$ the DMT model applies. $0.1 < \lambda < 5.0$ corresponds to the transition regime between JKR and DMT models and Maugis model applies [25]. All three theories predict that a finite negative force, often referred to as pull-off force or adhesion force, is required to separate the surfaces in contact.

The JKR theory incorporates adhesion into Hertz contact using the approach of energy balance between elastic energy and surface energy. It assumes that the attractive surface force acts inside the contact area only and the total contact force is the superposition of elastic Hertzian contact force and attractive force induced by the surface energy. The interparticle force and contact radius for JKR theory are given [20]

$$F_{jkr} = \frac{4E^*}{3R_e}a^3 - \sqrt{8\pi w E^*}a^{\frac{3}{2}} \tag{1.6}$$

$$a^4 - 2R_e\delta a^2 - \frac{2\pi w}{E^*}R_e^2 a + R_e^2\delta^2 = 0 \tag{1.7}$$

where $\delta$ is the overlap between two particles and $a$ is the contact radius. Equation 1.5 contains a deformation contribution according to the Hertz model and an adhesion component because of work of adhesion.  In addition, the JKR theory is consistent with the Hertz contact theory when the adhesion of work is equal to zero.

The DMT theory, in contrast to the JKR theory, assumes that the attractive surface force exists outside the contact area and the deformed contact profile remains the same as in the Hertz theory. For the smaller $\lambda$ ($\lambda$ <0.1),  the relationship between deformation and force can be expressed [21]

$$F_{dmt} = \frac{4E^*}{3R_e}a^3 - 2\pi R_e w \tag{1.8}$$

$$\delta = \frac{a^2}{R_e} \tag{1.9}$$

The Maugis theory considers a Dugdale potential (square well) to describe attractive forces and derives an analytical contact model for the entire range of material parameters and points out that JKR and DMT theory  represent the extremes of the whole spectrum. Maugis model can be written as [22]

$$\overline{F} = \overline{a}^3 - \lambda\overline{a}^2(\sqrt{m^2-1} + m^2 tan^{-1}\sqrt{m^2-1}) \qquad (1.10)$$

$$\overline{\delta} = \overline{a}^2 - \frac{4}{3}\overline{a}\lambda\sqrt{m^2-1} \qquad (1.11)$$

$$\frac{\lambda\overline{a}^2}{2}\left[\sqrt{m^2-1} + (m^2-2)tan^{-1}\sqrt{m^2-1}\right] + \frac{4\lambda^2\overline{a}}{3}\left[\sqrt{m^2-1}tan^{-1}\sqrt{m^2-1} - m + 1\right] = 1 \qquad (1.12)$$

where $\overline{F} = \frac{F}{\pi w R_e}$,$\overline{a} = a\left(\frac{4E^*}{3\pi w R_e^2}\right)^{1/3}$, $\overline{c} = c\left(\frac{4E^*}{3\pi w R_e^2}\right)^{1/3}$, $\overline{\delta} = \delta\left(\frac{16E^{*2}}{9\pi^2 w^2 R_e}\right)^{1/3}$,$m = \frac{c}{a}$ and $c$ is the outer radius and $a$ is the radius of contact circle.

In the JKR and DMT models, the overlap between two particles can be first computed based on their relative positions, then to substitute the value of overlap to Equations 1.6 or 1.8, the corresponding contact force can be obtained. As for the Maugis model, it is cumbersome to utilize because there is no single explicit expression between contact radius and applied load. In order to solve Equations 1.10-12 simultaneously, we need to first let $m$ vary approximately between limits, and then the contact radius is determined from Equation 1.11; this procedure has to be iterated until Equation 1.12 is satisfied. Thereafter, the contact force between particles can be computed using Equation 1.10.

## 1.2 Objective

The main objective of this work is to investigate particle behavior such as packing, mixing, particle dynamics, and interaction between dry coated particles, by means of numerical simulations. Of particular interest is to reveal the connections between bulk behavior of particle assembly and particle scale variables, such as particle size, surface energy, and particle shape.

## 1.3 Proposal Outline

This thesis includes seven chapters. Chapter 1 introduces the background of DEM simulation and the objective of this research. Chapter 2 presents the packing properties of cohesive particles, focusing on the effect of surface energy, particle size, and particle shape. Chapter 3 discusses the particle packing under external compressive loading. Chapter 4 presents the DEM modeling of magnetically assisted impaction mixing (MAIM). Chapter 5 focuses on the particle dynamics inside a conical screen mill (comil). Chapter 6 presents the numerical model of adhesion and friction between dry coated particles. Chapter 7 summarizes the results and proposes some future research directions.

# CHAPTER 2

# PARTICLE PACKING UNDER GRAVITATIONAL FORCE

## 2.1 Introduction

The packing of both cohesive and non-cohesive particles has been investigated using DEM simulations [12, 14, 26-31]. The validity of DEM simulations has been tested by means of comparison between experimental and simulated results. For example, DEM simulation obtained packing density is 0.633 [28], which is comparable to experimental data about random close packing (RCP) of 0.6366±0.0005 [32]. For random loose packing (RLP), simulation results also show that the packing density could range from 0 to 0.64, depending on the initial simulation conditions and parameters such as cohesive force, frictional force and so on [33]. The DEM simulation approach can also provide other useful information including the RDF and force distributions and hence has become more and more popular in studying the particle packing problem.

In this section, the particle packing is studied using DEM simulations. Unlike previous work, where the van der Waals force is used to represent the cohesiveness between particles [12-14], in this work, the cohesive force is based on the JKR model [20]. The results including porosity, radial distribution function (RDF), and contact geometry, for various particle sizes, surface energies, and aspect ratios have been presented.

## 2.2 Model and Initial Parameters

In this research, the packing model is created using EDEM (EDEM 2.4, DEM Solutions, Edinburgh, Scotland). The governing equations for individual particles can be written as follows:

$$m_i \frac{d\vec{v}_i}{dt} = \sum_{j \neq i}^{k} \vec{F}_{ij} + m_i \vec{g} \tag{2.1}$$

$$I_i \frac{d\vec{\omega}_i}{dt} = \sum_{j \neq i}^{k} \vec{T}_{ij} \tag{2.2}$$

$$\vec{F}_{ij} = \vec{F}_{ij}^{n} + \vec{F}_{ij}^{t} \tag{2.3}$$

$$\vec{T}_{ij} = \vec{R}_i \times \vec{F}_{ij}^{t} - \vec{\tau}_{ij}^{r} \tag{2.4}$$

where $m_i, \vec{v}_i, \vec{\omega}_i, \vec{R}_i, I_i$ represent the mass, translational velocity, rotational velocity, vector connecting the center of particle *i* and the contact point, and the moment of inertia of particle $i$. $\vec{F}_{ij}$ is the contact force induced by particle $j$ and it can be divided into two parts: normal contact force $\vec{F}_{ij}^{n}$ and tangential contact force $\vec{F}_{ij}^{t}$. $\vec{T}_{ij}$ represents the torque induced by particle $j$ due to tangential contact force and rolling friction force. The total contact force and torque is the summation over *k* particles in contact with particle *i*. The contact model including the cohesive force based on JKR model is used in this work to describe the interaction between particles [20]. Further details about contact model can be found in the references [18, 19]. For incorporating cohesion, two different surface energy values are considered: a low value of 10mJ/m$^2$ is used to see how the behavior changes from no cohesion to low cohesion, and a higher value of 50mJ/m$^2$ is also used that represents a typical pharmaceutical material.

Initially, five thousand particles are randomly generated in the cylindrical container, called cylinder hereafter, without allowing overlap between them. The volume of the cylinder is changed according to the size of the particles so that the initial porosity for all simulations is constant at 94%. Once initialized, the particles fall down under gravitational force and settle down at the bottom of the cylinder. To minimize the effect of the wall of the geometry, periodic boundary conditions are used along the horizontal directions (x and y). Particles with three different aspect ratios of 0.0 (sphere), 1.0, and 3.0 are used in this paper. The spherocylinder particles are formed with multi-sphere approach [34-37], which allows the particles to superimpose to form a composite particle with complex shape. One of the advantages of multi-sphere approach is that it leads to the simplicity of contact detection algorithms, thus decreasing the computation challenge as compared with other methods [38, 39]. Four and twelve ideal spherical particles are used to constitute the spherocylinder particles with aspect ratios of 1.0 and 3.0, respectively. The aspect ratio α, here defined as $\alpha = \frac{L}{d}$, where the L is the overall length of cylinder and d is the diameter of an individual particle, is the same as in other references [40, 41].

The system is regarded to be steady if the porosity does not change during a large number of DEM time steps. After the steady state is achieved, the porosity, RDF, and contacts corresponding to the steady state are obtained according to the simulation results. Figure 2.1 shows the initial configuration of simulation model used in this paper. The magnified pictures in Figures 2.1(b) and (c) show the spherocylinder particles with aspect ratio of 1.0 and 3.0, respectively, which are composed through the multi-sphere assembly.

The values of the initial parameters and material properties used in this simulation are listed in Table 2.1.

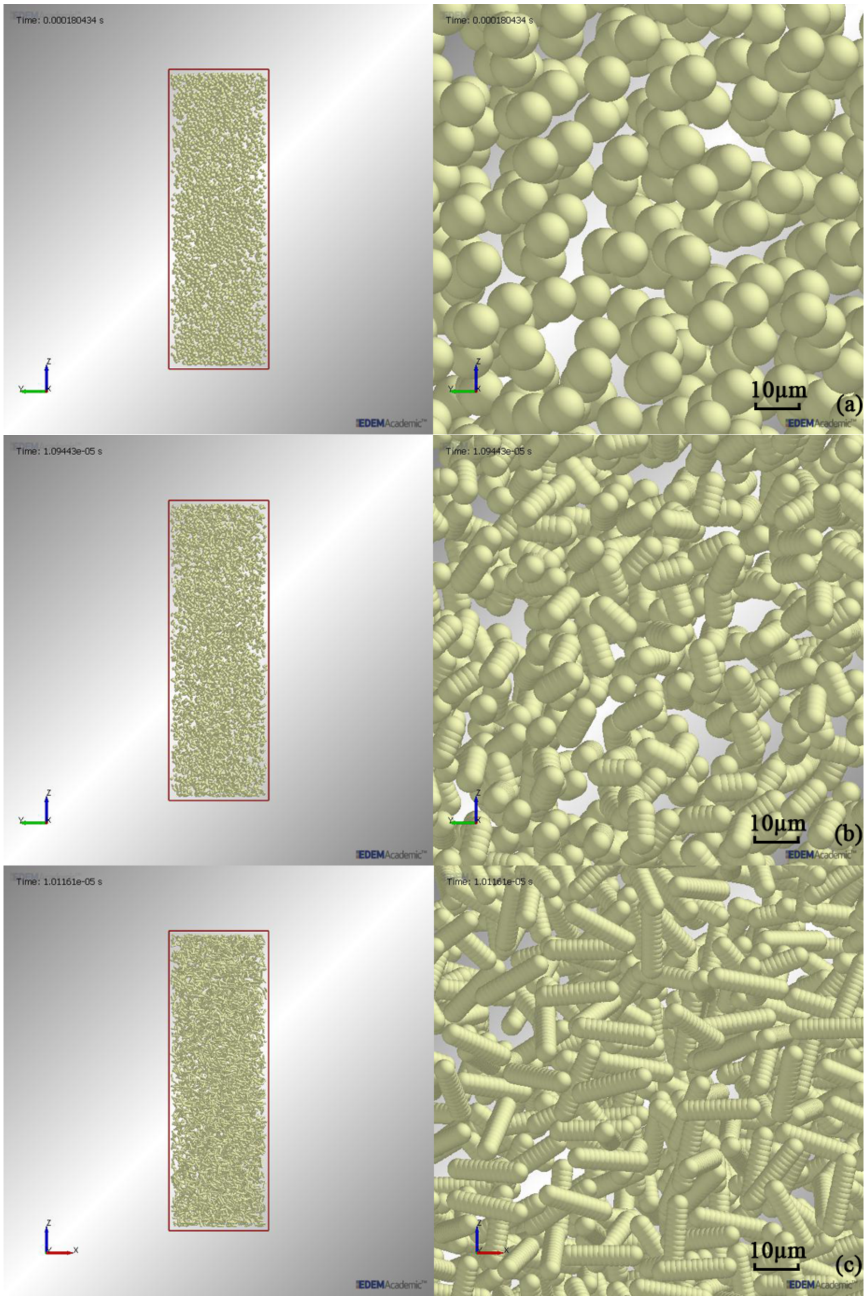

**Figure 2.1** The schematic representation of the simulation model for packing at different aspect ratios.

**Table 2.1** Initial Parameters and Material Properties for Simulation

| Parameter | Value |
|---|---|
| Density of particle | 1500(kg/m$^3$) |
| Diameter of particle | 10~1000(μm) |
| Surface energy of particle | 0,10,50(mJ/m$^2$) |
| Shear modulus of particle | $1.0^8$(Pa) |
| Poisson ratio | 0.3 |
| Friction coefficient | 0.4 |
| Rolling friction coefficient | 0.01 |
| Time step | $5.6\times10^{-6}$~$9.5\times10^{-9}$(s) |
| Initial porosity | 0.94 |

## 2.3 Results and Discussion

### 2.3.1 Packing Porosity

Figure 2.2 shows the porosity as a function of different particle sizes, surface energies, and aspect ratios. For the spherocylinder particles with $\alpha$=1.0 or $\alpha$=3.0, the particle diameter is defined as the diameter of a sphere which has volume equivalent to the corresponding spherocylinders. The porosity decreases with increasing particle size for the case of non-zero surface energy for $\alpha$=0.0, as seen in the Figure 2.2(a). However, when the surface energy is zero, corresponding to non-cohesive particles, the porosity is almost constant, independent of the size of the particles. For the experimental results for coarse particles, where the effect of cohesive force on packing can be ignored compared to gravitational force, it has been reported that there are two reproducible packing states, named RLP (random loose packing) and RCP (random close packing) with porosity of 0.40 and 0.36, respectively [42]. Simulation results shown here for the case of no cohesive force are within this range, as expected. With increasing surface energy, the porosity also increases. However, the effect of surface energy on the porosity becomes weaker with increasing particle size because the gravitational force becomes dominating. For example, there is no significant difference between particles having the surface energy of 10mJ/m$^2$ and 50mJ/m$^2$ for sizes of 500 and 1000 micrometers.

The porosity values from the present simulations are also compared with previously published results from DEM simulations where the van der Waals force model is used instead of the JKR model [12]. As shown in the Figure 2.2(a), the previous results are comparable with ours at the surface energy of 10mJ/m$^2$. The relationship between surface energy, γ, and Hamaker constant, H, is $\gamma = \frac{H}{24\pi z_0^2}$, where the $z_0$ is the cut-off distance when two particles contact each other with the typical value of 0.165nm [24]. Since the Hamaker constant value of $6.5\times10^{-20}$J is used in the reference [12], the corresponding surface energy is 32 mJ/m$^2$. One possible reason why results from the reference [12] match well with the surface energy of 10 mJ/m$^2$ instead is that the cut-off distance used in the reference [12] is 1.0 nm, which is larger than the typical value and leads to a smaller cohesive force between particles. The value of cut-off distance in the cohesive force based on the van der Waals model is somewhat of an arbitrary parameter, representing the intrinsic repulsion between particles. It is pointed out that different values of cut-off distance are used in the previous publications, for example, 1.0nm, 0.165nm, or 0.4nm [12, 43, 44], which makes it difficult to compare them with other simulations or experimental results.

Figures 2.2(b) and (c) show the simulation results of the porosity for $\alpha$=1.0 and $\alpha$=3.0. The relationship between porosity and particle size is generally similar to that of aspect ratio of 0.0 (Figure 2.2(a)). Therefore, for all three aspect ratios, when the surface energy is not zero, porosity increases with decreasing particle size, and increases with increasing surface energy. Otherwise, porosity is almost constant regardless of the size of the particles. In addition, it can be seen from Figures 2.2(b) and (c) that while the porosity becomes significantly higher for finer particles in the presence of cohesive force, i.e., as surface energy goes from 0 to 10mJ/m$^2$, the difference in porosity when the surface energy changes from 10mJ/m$^2$ to 50mJ/m$^2$ for both aspect ratios is not as significant.

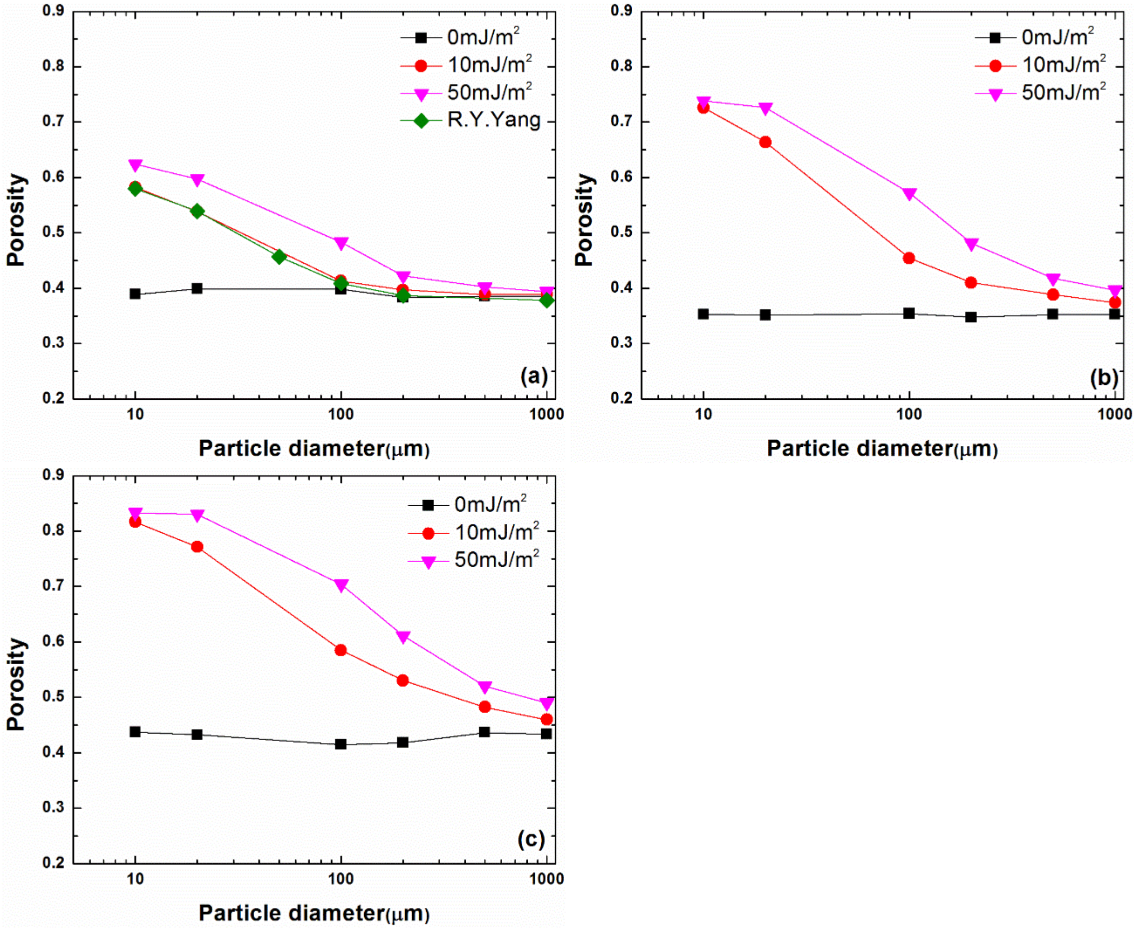

**Figure 2.2** The relationship between porosity and surface energy for different aspect ratios.

It is clear that the results about porosity trends seen in Figure 2.2 have combined effects of both the cohesion, represented via surface energy, and the aspect ratio in addition to the particle size. Also, the surface energy and particle size together determine the influence of cohesion. Thus it is not very easy to assess the main impact of aspect ratio, which can be better highlighted when the results shown in Figure 2.2 are reorganized, shown in Figure 2.3. From Figure 2.3(a), it can be seen that when surface energy is zero, the porosity for the aspect ratio of 1.0 is less than that of the aspect ratio 0.0, and the aspect ratio of 3.0 corresponds to the largest porosity among the three of them.

As mentioned before, different results for packing of particles with varying aspect ratios based on different simulation methods have been published. In the mechanical contraction method, the packing is constructed by means of moving particles to avoid overlap between them as the simulation box is compressed, until it is impossible to separate the overlapping particles if the box is contracted further [45]. The results from that method indicate that porosity first decreases, and then begins to increase after arriving at a minimum value. Qualitatively similar phenomena were obtained using the relaxation algorithm, although the specific value of the aspect ratio corresponding to the minimum porosity was in the range from about 0.35 to 0.50 as reported in different reports [40, 41, 46]. For the simulation of packing using the relaxation algorithm, the packing of particles is performed by means of relaxation of compacted particles with initially unrealistically large overlap between them until the maximum overlap of all the particles in the system is lower than a critical value [40, 41, 46]. The previous results based on mechanical contraction and relaxation algorithm have shown that the porosity for aspect ratio of 0.0 is higher than that of the 1.0, but lower than that of the 3.0 [40, 41, 45], qualitatively agreeing with our current results based on DEM simulation when there is no cohesion. Cohesion has not been accounted for in the relaxation or contraction algorithms.

When the surface energy is 10mJ/m$^2$ as is shown in Figure 2.3(b), the porosity corresponding to the aspect ratio of 1.0 increases faster and eventually becomes larger than the porosity for the aspect ratio of 0.0 for particles sizes less than 200 micrometers. For the larger particles, the porosity for the aspect ratio of 0.0 is still larger than the porosity for the aspect ratio of 1.0, consistent with the results for the surface energy of 0.0mJ/m$^2$. It is reasonable, as previously discussed, that since the gravitational force dominates for the larger particle size, cohesion effects are reduced. When the surface energy increases to 50mJ/m$^2$, the porosity for the aspect ratio of 1.0 is larger than the corresponding result for the aspect ratio of 0.0, except for the larger particle size of 1000 micrometers. Irrespective of the surface energy values, the porosity for aspect ratio of 3.0 is always higher than that of the other two aspect ratios. Thus, higher porosity values in the experimental results for pharmaceutical powders as compared to the prediction of the published model may be explained based on the aspect ratio, since most of those powders have acicular shapes with high aspect ratio. This also indicates that our simulation results, including the effects of aspect ratios, better agree with experimental results of pharmaceutical powders [47], where although higher surface values are may offer one reason for the deviation, the effect of the aspect ratio may be most relevant.

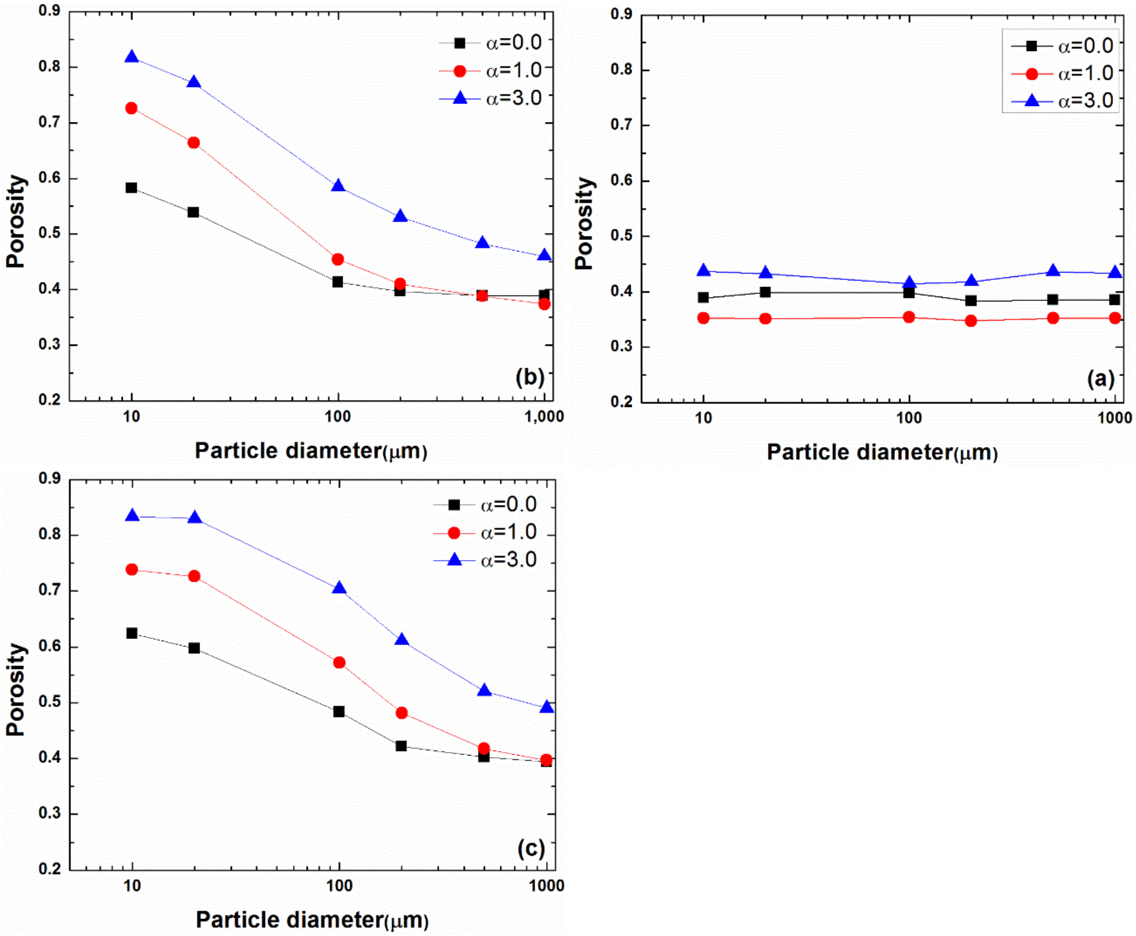

**Figure 2.3** The effect of aspect ratio on porosity for different surface energy values.

### 2.3.2 Radial Distribution Function

In order to better understand how the particle properties impact the packing structure and hence the porosity, the radial distribution function (RDF) values are computed. RDF, expressed as $g(r)$, is the probability associated with finding particles at a certain distance of $r$ of a reference particle. Function $g(r)$ is given by:

$$g(r) = \frac{dN(r)}{4\pi r^2 \rho dr} \tag{2.5}$$

where the *N(r)* is the particle number within a sphere with the radius of *r*, and $\rho$ is the particle number in the unit volume.

Figure 2.4 shows the results of RDF for different particle sizes when α=0.0 and surface energy=50mJ/m$^2$. It reveals that for the largest particle size, i.e., 1000 micrometers, there are two peaks in the RDF at the distance of 1.73d and 2.0d (see inset, note trimmed ranges for x and y axes), agreeing with known two characteristic contacts of spherical particles: edge-sharing in-plane equilateral triangle and the centers of three particles in a line. This represents packing of non-cohesive spherical particles, since the particle size is large enough to negate any influence of cohesion. With decreasing particle size, the first peak at 1.73d disappears, which indicates more uniform packing for fine particles [12]. Therefore, overall, these results of RDF for spherical particles agree with previously published data [12, 48, 49].

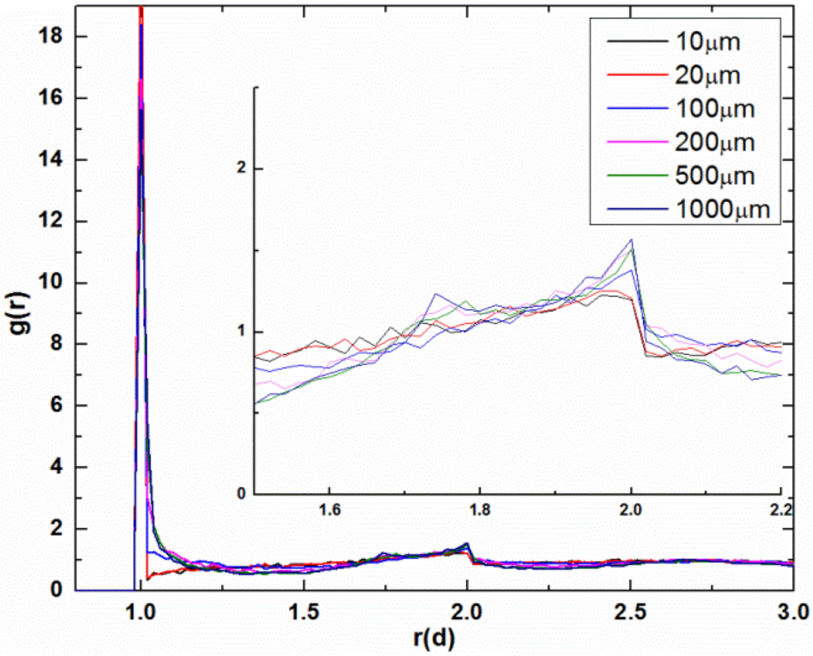

**Figure 2.4** The radial distribution function (RDF) for spherical particles.

The radial distribution function is commonly used with spherical particles, but generalizations of the RDF are also used to analyze the packing of non-spherical particles [45, 50]. The results of RDF for different aspect ratios, particle sizes, and surface energies are presented in Figure 2.5, where the vertical scale is trimmed to show the details of the distributions. For large particles, e.g., 1000 micrometers, Figures 2.5(a), (b), and (c) show that the number of peaks are different corresponding to the different aspect ratios of 0.0, 1.0, and 3.0. For the aspect ratio of 0.0, there are three peaks for all the different surface energy cases. However, for the aspect ratio of 1.0, the first peak at the distance of 1.0d is followed by a depletion region, while there is another peak at the distance of 1.5d. Thus, the characteristic of RDF of spherical particles vanishes with increasing aspect ratio. When the aspect ratio increases to 3.0, only the first peak at the distance of 1.0d still exists, then the RDF decays to a nonstructural value.

Similar to the effect of surface energy on porosity for various particle sizes, where the surface energy has less influence on the porosity for larger particle size because the gravitational force dominates, the effect of surface energy on RDF is not obvious for large particles, e.g., for 1000 micrometers. The results of RDF based on the method of mechanical contraction qualitatively agree with our simulation results using DEM for different aspect ratios [45]. For example, their results indicate there is only one peak and is not followed by a depletion region for the larger aspect ratio in the plot of RDF, which is actually similar to our results for aspect ratio of 3.0. The variation of number of peaks for different aspect ratios has also been verified by the simulation results using the relaxation algorithm [41].

However, quantitatively, current results only show two possible types of local contact structures for the aspect ratios of 1.0 and 3.0: parallel contact and perpendicular contact as indicated in reference [41], corresponding to the two peaks at 1.0d and 1.5d in the RDF plot, respectively. As shown by the inset in the Figure 2.5(a), the parallel contact is two spherocylinders contact with the shortest distance between their centroids and the axes of cylinders are parallel to each other. In contrast, the perpendicular contact is formed by the two spherocylinders with perpendicular axes [41]. For the results based on the relaxation algorithm employing more values of aspect ratios, a peak at 2.0d appears with the change in aspect ratio and it corresponds to another type of local contact structure [41]. However, performing DEM simulations for many different aspect ratios is outside of the scope of the present paper due to higher computational burden, and in the next sub-section, coordination number analysis is employed for further examining the packing structure.

In order to highlight the effect of surface energy, the RDF functions for fine particles (size 10 micrometers) and high surface energy (50mJ/m$^2$) for all three aspect ratios ($\alpha$=0.0,1.0, and 3.0) are shown in Figure 2.5(d). For spherical particles ($\alpha$=0.0), results are similar to previous discussion that the second peak at 1.73d vanishes for fine particles. For aspect ratio of 1.0, the peak at 1.0d shifts slightly towards a higher value. One possible reason is that the parallel contact structure discussed before for Figure 2.5(a) may have changed as the particle-pair may not get well aligned and result in a small angle shown in the inset in Figure 2.5(d). When the aspect ratio is 3.0, there are no obvious peaks in the RDF, indicating more uniform packing structure. Therefore, based on the information obtained from RDF, the surface energy has significant effect on the packing structure. As surface energy changes, the packing structure may also correspondingly change.

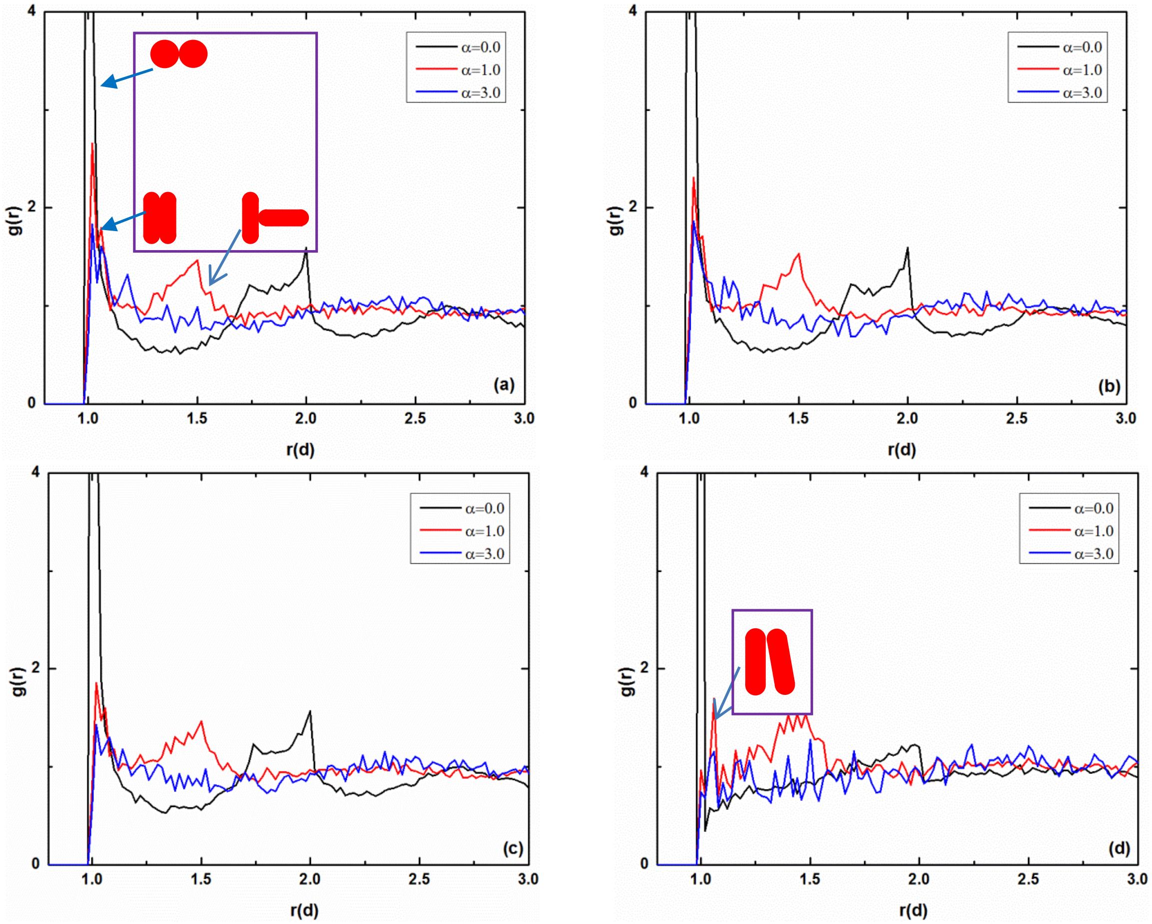

**Figure 2.5** The effect of aspect ratio on radial distribution function (RDF) for different surface energy values.

### 2.3.3 Coordination Number

Coordination number distributions provide quantitative description of the contacts between the particle and its neighbors. In the simulation, the specific value of coordination number depends on the definition of critical distance of separation, below which the two particles are regarded as being in contact. Critical distance values of 1.005d and 1.01d (d is the particle diameter) have been used to calculate the coordination number in previous work [12, 48]. Obviously, the coordination number will increase with increasing critical distance because more neighboring particles that do not directly contact with the specified particle will also be included into the coordination number [12].

Information about the contacts can be computed and saved during the simulation using the EDEM software, although the exact algorithm and cut-off distance employed by EDEM are not specified. These results are shown in Figure 2.6(a). As can be seen, these results show little impact of particle size on coordination number for the aspect ratio of 0.0, and hence do not agree with previously published results [12]. Hence, it is apparent that EDEM software does not employ the cut-off distance of separation of 1.005d and hence these results cannot be directly compared with the previous results. In order to better compare our simulation results with previously published data, the coordination numbers for spherical particles are specifically calculated for the cut-off distance of separation of 1.005d, shown in Figure 2.6(b). Comparing Figure 2.6(a) to (b), it can be seen that the results with 1.005d cut-off distance are higher than those exported data from EDEM in Figure 2.6(a), indicating that cut-off distance used by default in the EDEM to calculate the coordination number is smaller than 1.005d. Although not shown here, comparable results with the EDEM of Figure 2.6(a) were obtained by setting the cut-off distance of separation to 1.0d, which implies only those neighbors having direct contact with the specific particle are counted into coordination number generating by EDEM software; thus confirming that EDEM results are equivalent to direct contact between the particles, equivalent to the cut-off distance of 1.0d.

For the spherocylinder particles, it is not convenient to calculate the coordination numbers at various, specific cut-off distances because the shortest distance between two spherocylinders is dependent on the relative orientation of their axes. Consequently, for the sake of consistency between various aspect ratios, the subsequent results and the discussion of the coordination numbers at non-zero aspect ratios only be concerned with the results directly obtained from the EDEM. According to the Figure 2.6(a), when the surface energy is zero, the coordination number ranges from 4.37 to 4.64, depending on the size of the particles. These results are comparable to some of the previously reported experimental and simulation results. For example, Mason obtained the coordination number of 4.76±0.02 from the experimental results of Scott [51, 52], which is also in good agreement with the simulation result of 4.79±0.02 [53]. The slight difference between our simulation results and the experiment is probably due to the larger particle size (3175 micrometers) with higher density (steel, 7.8kg/m$^3$) used in the experimental investigation, and because the shaking was done after pouring the particles into the cylindrical container in the experiment, causing the particles to rearrange and pack more densely [51].

For zero aspect ratio particles, as per Figure 2.6(a), the coordination number decreases when the surface energy is increased to 10mJ/m$^2$ and 50mJ/m$^2$. The reduction in the coordination number for various surface energy values demonstrates that the surface energy, hence the cohesive force, is an important material property that influences the packing structure, just like what has been observed with the friction coefficient [29].

Within the packing, not every particle has the same coordination number. Therefore, the distributions of coordination numbers, which can provide more detailed information about how the coordination number changes under various conditions, are examined. Figures 2.6(c) and (d) show the results of the distributions of the coordination numbers for particle sizes of 10 micrometers (very fine, hence cohesive, except when surface energy is zero) and 1000 micrometers (large, hence mostly non-cohesive). As depicted in Figure 2.6(c), when the surface energy changes from 0mJ/m$^2$ to 10mJ/m$^2$, the coordination number distribution shifts towards the lower value and the width becomes narrower. When the surface energy increases from 10mJ/m$^2$ to 50mJ/m$^2$, there is no further variation in the width of distribution and the overall distribution shifts towards the lower value, and hence it is the main reason behind the decreasing coordination number. According to the previous results, the effect of surface energy on the coordination number is different than the effect of the friction coefficient, where only overall distribution shift is observed with increasing friction coefficient [29], but no change in the width. In addition, when the surface energy is 50mJ/m$^2$, the minimum value seen in the distribution is one, indicating there are a few particles that only have a single contacting neighbor. Note that although there is very low probability for a particle to have a coordination number of one, it is a finite, non-zero value. This was found to be the case regardless of the cut-off distance of separation, which was changed from 1.0d to 1.01d (results are not shown for the sake of brevity).

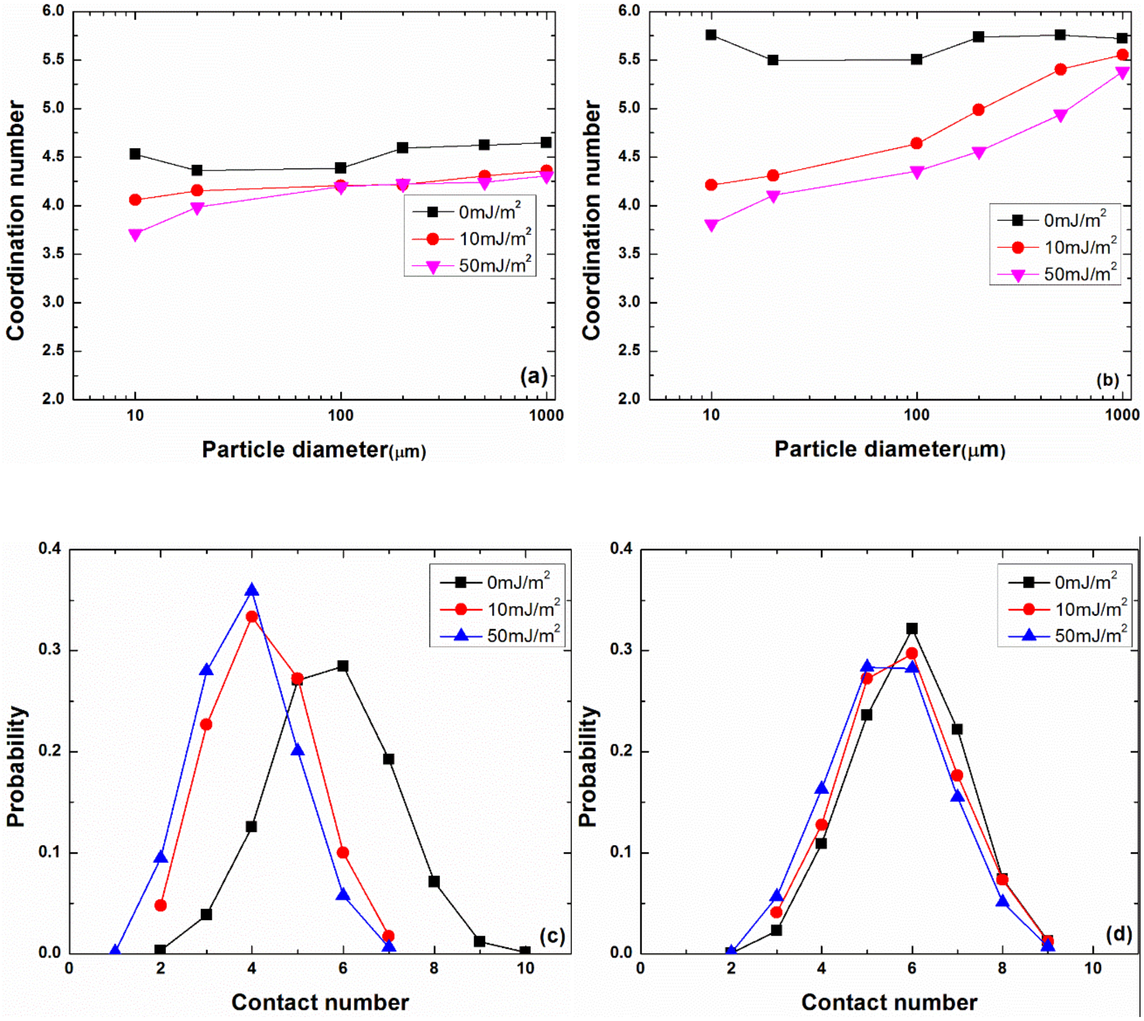

**Figure 2.6** The coordination numbers and its probability distribution.

Having a coordination number of one in a static packed-bed may be a special case of packing and, to our knowledge, such situations have not been discussed before. The lack of previous references on such structure may also be due to the fact that our observations are for the case of packing of fine, cohesive powders, which have not been previously well-discussed. In order to identify the corresponding structure for this situation, the snapshots showing the particle with only one contact and all its neighbors within the distance less than 2.0d are shown in Figure 2.7. In Figures 2.7(a) and (b), two different particles, each having only one contact, are shown, and they were randomly selected from the list of such particles (for reference, their identity numbers during the simulation are 4230 and 619, respectively). In Figures 2.7(a) and (b), the blue color represents the particle with a single contact (central particle) and the red ones represent its neighbors. While it may not be easy to discern from these figures, the blue particle only contacts with one red particle, and an arrow identifies that contacting red particle in each case. One could visualize from these pictures that the neighbors formed a cage-like structure around the central particle, and the central particle is attached to only one of them. This cage structure forms due to the strong cohesive force between the fine particles induced by the higher surface energy, and is an interesting situation previously not identified.

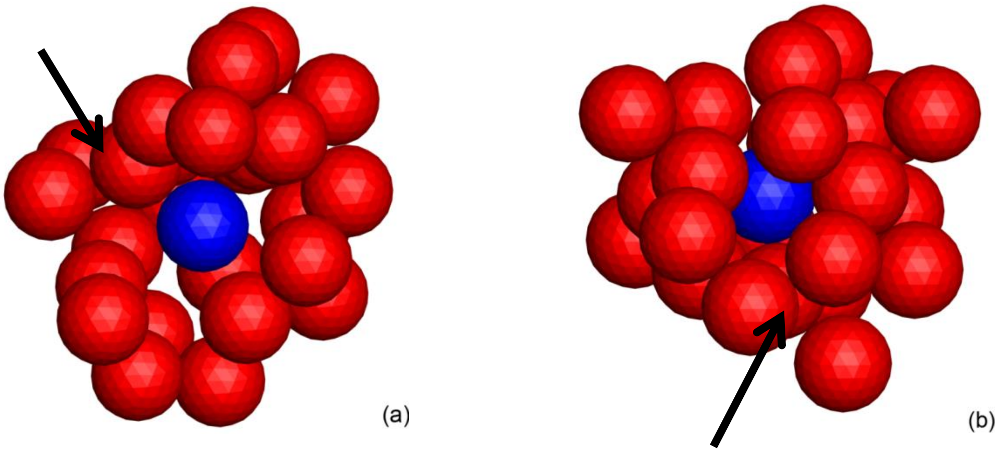

**Figure 2.7** Snapshot of the simulation depicting the cage structure.

It is worth noticing that in the previous simulation results based on the van der Waals model, it is shown that the a single contact appears, although at very low probability, for the particle size of 5 micrometers, but not for the size of 10 micrometers, and the corresponding cage structure has not been identified in that work [12]. The investigation about the effect of friction coefficient uncovered that the coordination number decreases to two with increasing friction coefficient, indicating the appearance of arching structure within the packing [29]. However, our results show a unique influence of surface energy on the coordination number and packing structure, indicating the appearance of particles with as few as one contact if the cohesive force is dominating compared to the gravitational force, because the cage structure can be supported and created within the packing. Compared to the arching structure, the cage structure should correspond to more sparse packing, leading to higher porosity values.

To further examine the influence of cohesion, or lack thereof, distributions for larger particles are considered. Accordingly, Figure 2.6(d) shows the coordination number distribution for particle size of 1000 micrometers. It can be seen that the change in the coordination number distribution due to increased surface energy is mainly in terms of the shift of distribution towards the lower values. However, the width and shape of the distributions stay approximately the same for various surface energy values. In addition, the differences in the distributions for three different values of surface energy are not prominent compared to the particle size of 10 micrometers. Moreover, the minimum attainable value of the coordination number is two for the particle size of 1000 micrometers at surface energy of 50mJ/m$^2$, indicating that there is no cage structure in the packing of 1000 micrometer particles in contrast to 10 micrometer particles which exhibit the effect of cohesion.

Figures 2.8(a) and (b) show the results of coordination numbers for aspect ratios of 1.0 and 3.0, which are directly obtained from EDEM simulation, thus each contact is true contact between the particles. When the surface energy is zero, the coordination numbers only slightly increase with increasing particle size for both cases. Upon examination of Figures 2.8(a) and 2.8(b) along with the zero aspect ratio case of Figure 2.6(a), it is seen that the coordination number increases with increasing aspect ratio for all values of the surface energy. This is an important observation and has implications to porosity as will be discussed next.

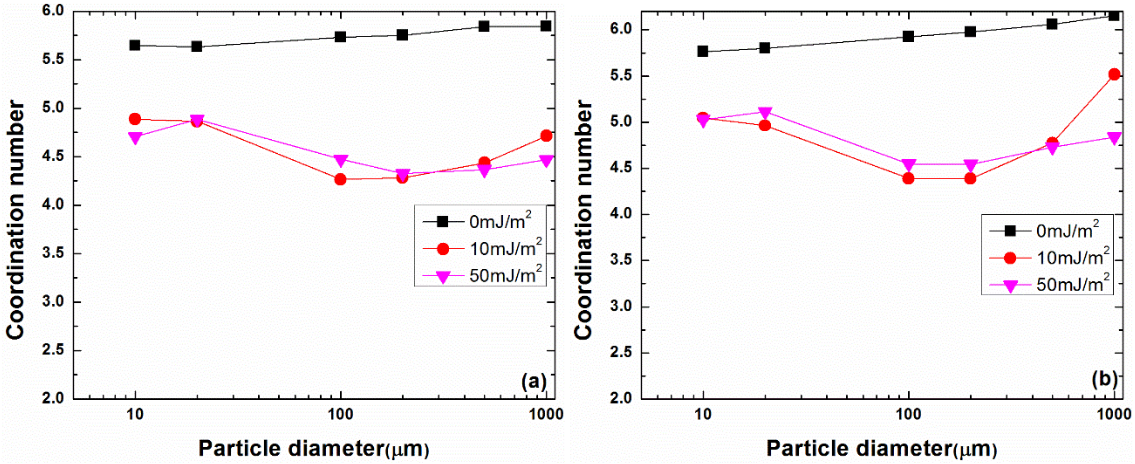

**Figure 2.8** The coordination numbers as a function of particle size for non-zero aspect ratios.

When the results for porosity shown in Figure 2.3 are examined along with the results for coordination number for different non-zero aspect ratios shown in Figures 2.6 and 2.8, it can be seen that there is no monotonously corresponding relationship between porosity and coordination number, which is indeed the case for monodispersed spherical particles (zero aspect ratio case) shown in [12]. In fact, for spherocylinder particles, as indicated by random contact equation [54, 55], the aspect ratio plays a role in the relationship between porosity and coordination number. However, it is not very clear how the aspect ratio impacts the contact geometry. Considering that the coordination number only provides information about how many neighboring particles exist around the specified particle within a certain distance, it lacks information about how those neighbors are arranged in space, hence information on the spatial packing structure. Next, we analyze the distribution of angles of contact vectors, which can represent the orientation of contacts, so that the effect of aspect ratio on porosity can be understood in more detail.

### 2.3.4 Distribution of Contact Vector

Contact vector is defined as the vector connecting the center of the particle and the contact point with its neighbor. Figure 2.9 shows the schematic diagram depicting the contact vector. The angles θ and ϕ define the azimuthal angle and polar angle in the spherical coordinate system, respectively. θ and ϕ can range from [0, 90°] and [0, 180°], respectively. However, the overall characteristic of distribution in each case can be obtained within [0, 90°] due to symmetry. Therefore, the values of θ and ϕ are constrained within [0, 90°] for simplicity. For each contact vector indicated by a green line with arrow in Figure 2.9, the value of θ and ϕ is calculated and the statistical distribution is given in Figure 2.10.

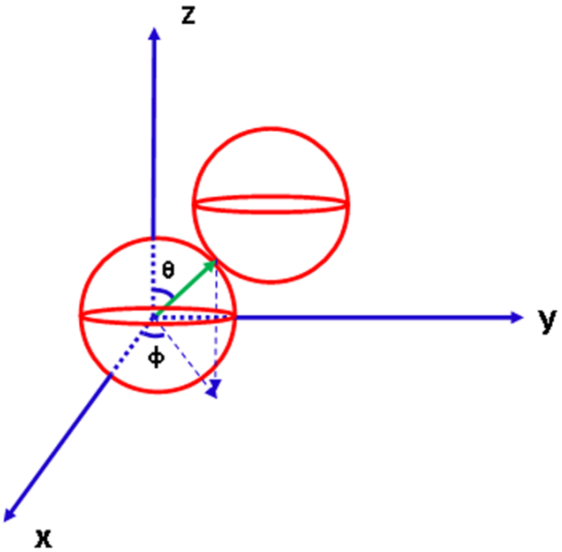

**Figure 2.9** The schematic diagram depicting the angles of the contact vector.

According to Figure 2.10(a), when surface energy is zero, the distribution of θ is increasingly wide (solid lines) as aspect ratio increases from 0.0 to 3.0. This is indicated by the height of two peaks; for case of the aspect ratio of 0.0 at about 48$^o$ and 90$^o$, decreasing as surface energy increases and the distribution becomes flatter. In contrast, the distribution of ϕ, shown in dashed lines, is flat and lacks any obvious peaks for the aspect ratios of 0.0 and 1.0. However, as the aspect ratio increases to 3.0, it develops a small peak at 90$^o$ at the expense of decreasing values at the lower angles. Therefore, with increasing aspect ratio, the θ distribution of contact vector widens and the amplitude of the peak at 90$^o$ decreases, but the ϕ distribution tends to develop a peak at 90$^o$, which differentiates it from the θ distribution.

The presence of peaks in the distribution of contact vector indicates that certain orientations are more preferable than others; in other words, the particles pack in a more orderly fashion compared to the case of the distributions without peaks. However, here, we see that while the θ distribution indicates less order as aspect ratio increases, the ϕ distribution suggests higher order. Therefore, we argue that due to the opposite trends of θ and ϕ distributions with respect to the aspect ratios, they should be two competing mechanisms that influence the porosity of packing. With increasing aspect ratio, the distribution of θ becomes wider, indicating less order in the structure and thus leading to higher porosity. However, the distribution of ϕ begins to develop a peak at 90 $^o$ and it is expected to lead to decreased porosity. Meanwhile, from Figure 2.10, the change of ϕ is not as pronounced as compared to the θ distribution. Therefore, the θ distribution should have a more significant effect on the porosity, which indicates decreasing porosity as surface energy increases, although the coordination numbers also increase at the same time.

The distributions of θ and ϕ for the surface energies of 10mJ/m$^2$ and 50mJ/m$^2$ are also calculated and shown in Figures 2.10(b) and (c) so that the influence of surface energy on the distributions, and hence on packing as well as porosity, can be revealed. According to the results, the general trends of the distribution are similar for all different surface energy values, although there are characteristic differences (for example, the position of the first peak of the θ distribution). With increasing aspect ratio, the height of θ distribution at $90^o$ continues to decrease, and the initial peak at $90^o$ for the aspect ratio of 0.0 continues to diminish as the aspect ratio and surface energy increase and finally forms a valley instead of a peak. On the other hand, the amplitude of the ϕ distribution at $90^o$ keeps increasing and forms a small but obvious peak at all non-zero surface energy values. At the same time, the amplitude of the distribution corresponding to the smaller angles decreases.

The variations seen in the θ and ϕ distributions for different aspect ratios can be used to explain the results about porosity shown in Figures 2.3(a), (b), and (c). For the Figure 2.3(a), the surface energy is zero and the porosity for aspect ratio of 3.0 is higher than that for aspect ratio of 0.0. However, the coordination number is also higher at higher aspect ratio as compared to lower ones. The reason for this is that the θ distribution tends to become flat and the packing becomes more disordered for aspect ratio of 3.0, which results in the higher porosity. For the Figures 2.3(b) and (c), the interpretation is similar to that of Figure 2.3(a). In addition, the results shown for RDF in Figure 2.5 show that for the fine particles with higher surface energy, parallel contact structure can change slightly and become non-parallel. As shown in the inset in the Figure 2.5(d), such configuration is likely to result in the distribution of θ changing accordingly and consequently the peak at $90^o$ would vanish. Therefore, the information from both the RDF plots and the distributions of contact vector match each other and explain the apparent contradiction between increased porosity for increased coordination numbers of fine, cohesive particles with non-zero aspect ratios.

In previous work, the $\theta$ distribution has been used to analyze the contact force in the assembly of spherical particles and the anisotropy of force network is illustrated, indicated by the appearance of the peaks in the probability distribution [14, 30]. According to our results in Figure 2.10, for the particles with aspect ratio of 0.0, the $\phi$ distribution is flatter for various surface energies. Therefore, only the $\theta$ distribution influences the contact geometry in this case and it is reasonable to ignore the effect of the $\phi$ distribution. However, when the aspect ratio is 1.0 or 3.0, the $\phi$ distribution begins to develop a peak at $90^{\circ}$ and this tendency is strengthened by the increased surface energy, which is an obvious deviation compared to the aspect ratio of 0.0. Although the increased porosity trends are mostly explained by the $\theta$ distribution, it would be interesting to examine how the $\phi$ distribution impacts the packing of non-spherical particles with higher cohesive force and aspect ratio, and to what extent it impacts the packing property; and hence would be a topic of future research.

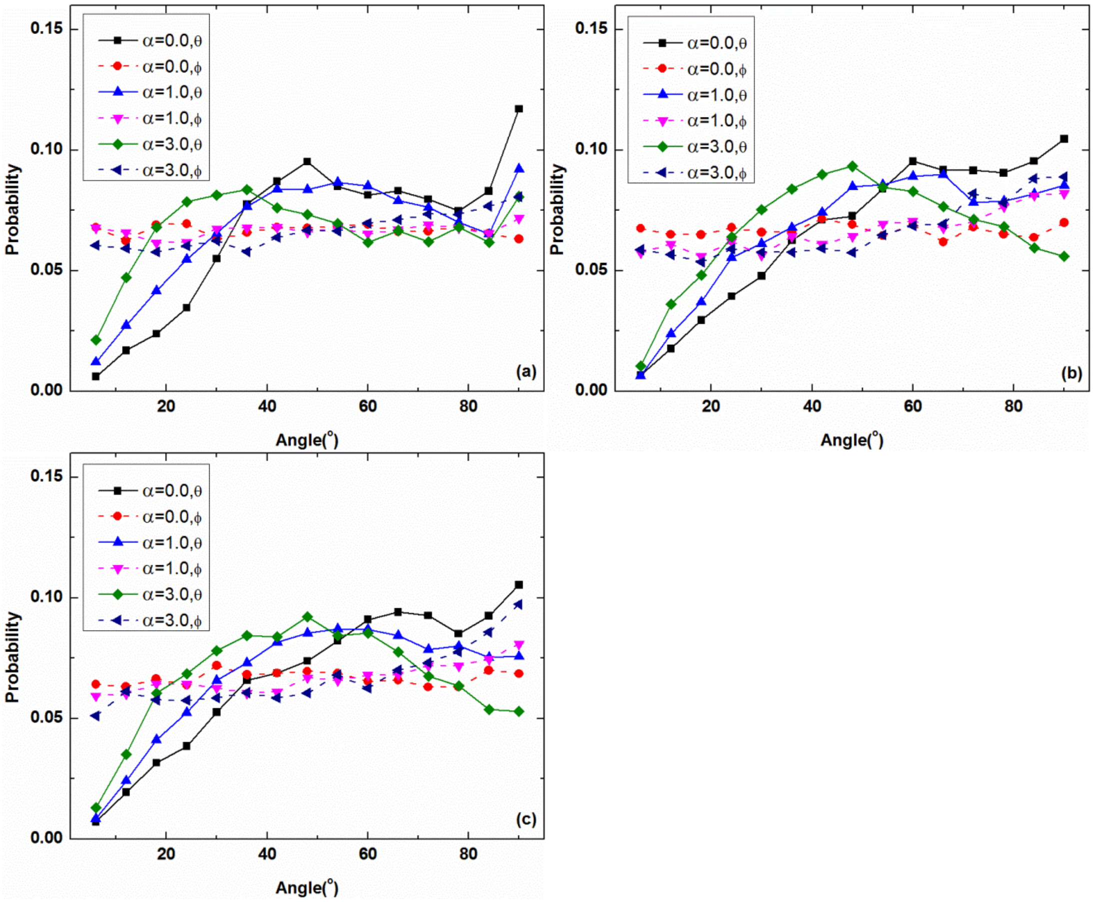

**Figure 2.10** The probability distribution of the contact vector angles.

## 2.4 Conclusions

The discrete element method is used to simulate the dynamic process of particle packing for different particle sizes, their surface energies, and aspect ratios. In contrast to the work reported to date, the JKR model and multi-sphere method are employed so that the effect of the surface energy (thus cohesion) and aspect ratio can be revealed. The simulation results show that particle sizes, surface energy, and aspect ratio all influence the porosity of packing to various degrees. When the surface energy is 0.0mJ/m$^2$, hence the particles are non-cohesive, the porosity stays almost constant for a fixed aspect ratio, regardless of the particle size. For the various aspect ratios, porosity corresponding to aspect ratio 0.0 is higher than that of 1.0, but less than that of 3.0, which is qualitatively in agreement with the results based on the mechanical contraction approach and the relaxation algorithm, validating the presented DEM simulations as a useful method to study the effect of particle shape on packing. In the presence of surface energy, particles are cohesive, and the porosity increases with decreasing particle size and increasing aspect ratio; all of which are generally expected. The radial distribution function (RDF) for all cases are computed and they show that the number of peaks for different aspect ratios change and show trends similar to the simulation results based on the relaxation algorithm. The coordination number analysis of all simulated cases reveals interesting patterns; the most novel outcome is the identification of the existence of single contact for a finite number of particles, attributed to the formation of a cage structure around the particle, when there exist strong cohesive forces as compared to the particle weight, due to higher surface energy and small particle size. Analysis of the coordination number distributions indicates that the surface energy tends to influence both the peak position and the width of the distribution because fewer contacts are required to achieve the mechanical equilibrium for the particles with higher surface energy. The relationship between coordination number and porosity shows another interesting outcome, which is that higher porosity, does not always imply fewer coordination numbers for the case of particles having non-zero aspect ratios and high surface energies. In fact, for higher aspect ratios, both coordination number and porosity increase as surface energy increases; hence, the coordination number analysis by itself is not sufficient to corroborate the porosity because of the lack of information regarding the orientation of contact vector for particles with higher aspect ratios. Consequently, the distribution of the angles of contact vector between the particles is analyzed to reveal useful information about the packing structure. Those results indicate that the distributions of θ, the azimuthal angle, ϕ, and the polar angle, have different trends with various aspect ratios. However, the θ distribution, being more dominant between the two, better explains the results of increased porosity in spite of higher coordination numbers for high aspect ratio particles.

In summary, the DEM simulation results presented here shed light on the packing density and structure for fine particles as well as coarse particles with various aspect ratios and surface energies, revealing interesting features not easily discerned via experiments, and confirm the important role of cohesion and particle aspect ratio in packing.

# CHAPTER 3

# PARTICLE PACKING UNDER COMPRESSIVE LOADING

## 3.1 Introduction

When subjected to the external force, the disordered granular media develop heterogeneous force networks to transmit stress at the boundaries through the interparticle contacts [56-58]. Such force networks are the key to understand the various phenomena associated with granular materials, such as jamming transition, and mechanical properties of static and dynamic dense granular media [59-64]. According to the magnitudes of contact forces, it is known from earlier studies that force networks in jammed granular media can be further decomposed into two categories: strong contact network and weak contact network, corresponding to the contacts carrying the forces larger or smaller than the mean contact force, respectively [65-67]. The nonsliding strong contacts form chainlike structures and carry the majority of the loading and the weak network behaves essentially like an interstitial liquid [65]. The percolation of such strong network in all directions signals a fully shear jammed state [68]. However, to data, there is no general theory about spontaneous emergence of such chainlike structures.

On the other hand, the interparticle contact forces are characterized by the probability distribution function (PDF) $P(f)$, defined as the probability for finding a contact force with a specific magnitude. Experimental results demonstrate that the contact force distribution is a signature of jamming transition [59]. In spite of intensive research focusing on the particle packing under confined stress in recent years, it is one of the long-standing fundamental problems in granular physics to identify the characteristic of tail of contact force distribution. Early experimental measurements using carbon paper technique [69-71] and contact dynamics simulations [72] or discrete element method [14, 30, 31] reported that the PDF decays exponentially for the normal forces larger than the mean normal contact force. However, the faster than exponential decay is also observed in the later experiments using photoelastic particles, emulsions, and liquid droplets [56, 59, 73], supporting by numerical simulations [60, 62, 74, 75]. Along with the experiments, many theoretical attempts have also been conducted to explain the tail behavior of PDF, such as $q$ model [76] and statistic description [77], supporting exponential and Gaussian tail, respectively. Furthermore, there is no consensus with regard to the distribution for the contact forces smaller than the mean either. For example, $q$ model predicts the PDF approaches zero with contact force approaches zero [76], which is inconsistent with experimental data [71]. In addition, using contact dynamics approach, the statistical distribution for normal and tangential contact forces lower or higher than mean values decays with power or exponential laws [72], indicating the statistical model probably applies only to the strong force network [72]. The discrepancy among the model predictions and available experimental data indicates that the more comprehensive researches are required in order to provide further understanding about the behaviors of jammed granular media. A promising and feasible way to test robustness of various theories is to investigate the jamming under various conditions such as different loads, and particle size distributions.

In this section, a set of DEM simulations designed to address the effects of various applied compressive loads and particle size distributions on force networks within jammed granular media. Of specific interests in this study is to unravel the difference between the strong and weak networks by investigating the spatial correlation and distribution of contact angle, chainlike structures in the strong and weak networks, and the response to external loads, which are distinct from previous work that addressed the complementary mechanical properties of strong and weak force networks [65].

## 3.2 Model and Initial Parameters

DEM approach is used to simulate particle packing between two parallel plates composed of particles on the top and bottom of the packing. The initial configurations are obtained by randomly placing particles within simulation domain without any overlap between any two of them. Then the particles settle down at the bottom plate under the gravity and a gradually increasing compressive force in the negative z direction is exerted on the top plate until it reaches a prescribed values. At each simulation step, the total forces exerted by the bulk particles on the top plate are computed and then equally assigned to all the particles belonging to the top plate so that all of them move together. Thereafter, we use pressure, which is the ratio of compressive force to the area of top plate, to quantity the degree of compression.

The interparticle interactions are described via nonlinear elastic Hertz-Mindlin spring-dashpot model where the dissipative damping forces are proportional to the relative normal and tangential velocities [78, 79]. The packing models with monodisperse and bidisperse size distribution have been constructed. The monodisperse simulation systems consist of total 5,000 particles with diameter of 1.0mm. The bidisperse simulation systems consist of 4,000 large particles with diameter of 1.0mm and 4,629 smaller particles with diameter of 0.6mm (mass ratio of smaller particles to the total particles is equal to 0.2). The microscopic parameters defined particle properties are the shear modulus of 29GPa, the Possion ratio of 0.2, the friction coefficient of 0.3, and the density of $2.0\times10^3$ kg/m$^3$. The total 3,200 glued particles with same material properties constituted the top and bottom plates. The periodic boundary conditions are employed in both $x$ and $y$ directions to eliminate the side wall effect.

## 3.3 Results

### 3.3.1 Contact Force Network

According to the magnitude of force carried by a contact, the contact network can be further divided into the weak and strong networks [65, 66]. The contacts involved in the strong network carry the force larger than a cutoff force and vice versus in the weak network. In this paper, the cutoff force is set to be the mean of all contacts [65]. The strong and weak contact networks for monodisperse and bidisperse systems at the pressure of 100MPa have been visualized in Figure 3.1. Contact vectors are shown using a cylinder connecting the centers of two contacting particles and the diameter and color (violet to red) of cylinders indicate the magnitude of corresponding contact forces (low to high). It can be seen that for the both monodisperse and bidisperse systems the contact segments in the strong network spatially prefer to form a chainlike structure along the compressive direction (vertical). Those observations are consistent with experimental results using frictionless droplets [73].

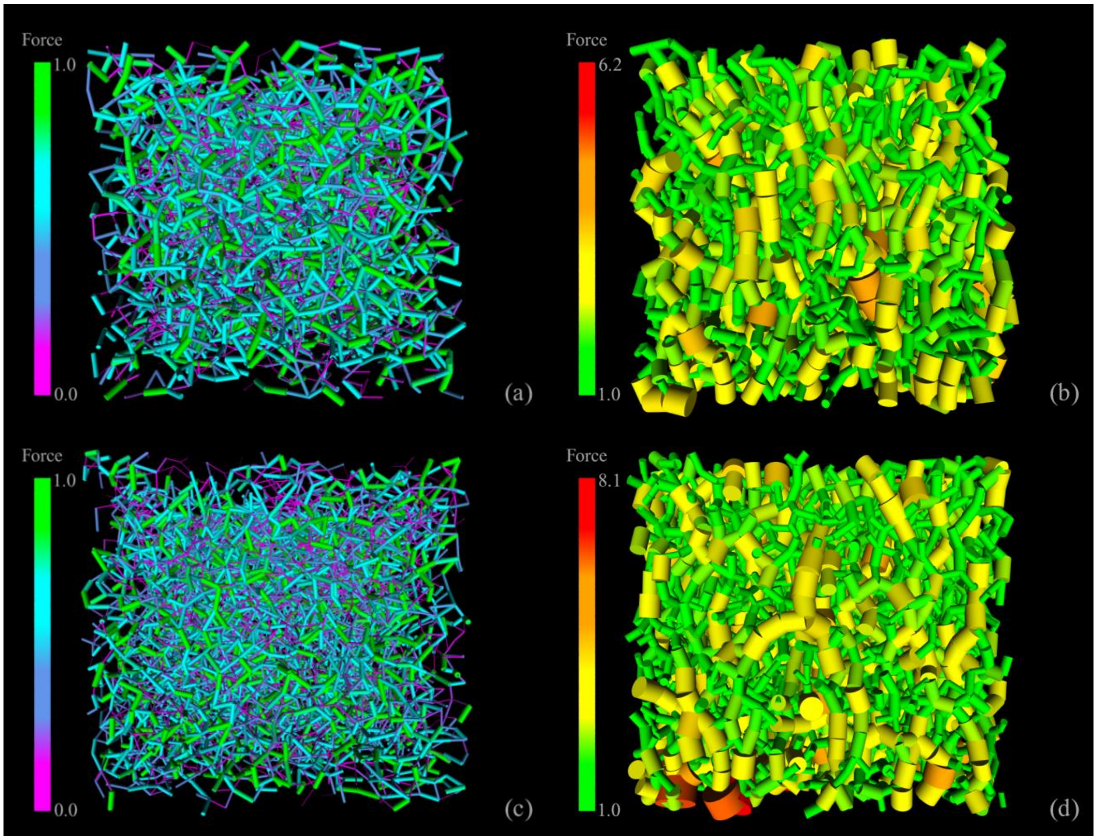

**Figure 3.1** Weak and strong force networks for the monodisperse and bidisperse systems at the pressure of 100MPa.

Various methods have been applied to characterize the chainlike structure of contact network in the literature [80-83]. In this study, in order to quantitatively analyze the chainlike structure in both weak and strong contact networks, two angles $\theta_1$ and $\theta_2$ between three jointing contact force segments have been defined in Figure 3.2. Suppose particle 1 in Figure 3.2 is the one who needs to be determined whether it is in a chainlike structure or not. First, its two neighboring particles are chosen (particles 2 and 3). Next, all the neighboring particles with particle 2 have been determined, which are shown as particle 4 and 5, and so on. Then, the value of angles $\theta_1$ and $\theta_2$ can be computed. The similar processes have been preceded for particle 3, which is another neighboring particle with particle 1. The force chain is allowed to have a reasonable degree of curvature [81], therefore, particle 3, 1, 2, and 4 are regarded as linear chainlike arrangements as long as both $\theta_1$ and $\theta_2$ are less than 45 degree (tolerance angle). Comparing with other methods characterized the force chain [82], the method presented here is able to identify the branching or emerging chainlike structures. The minimum number of particles involved into chainlike structure is four, instead of two or three [81, 83, 84].

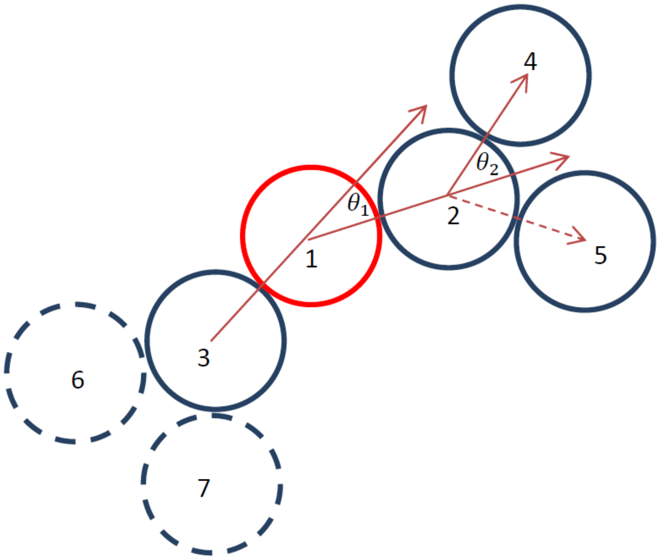

**Figure 3.2** Schematic of chainlike structure analysis.

Figure 3.3 presents the extracted chainlike structures using the method described above in the both weak and strong contact networks. For the chainlike structures in the strong network, they preferentially arrange themselves along the compressive direction for both monodisperse and bidisperse systems. The longest chainlike structure in Figure 3.3(b) is composed of thirteen individual particles. In contrast, there are 12 large particles plus 3 small particles constitute the longest chainlike structure in Figure 3.3 (d). For the chainlike structures in the weak network, there are no preferential arrangements along compressive direction and the longest length of chainlike structure is shorter than that in the strong network.

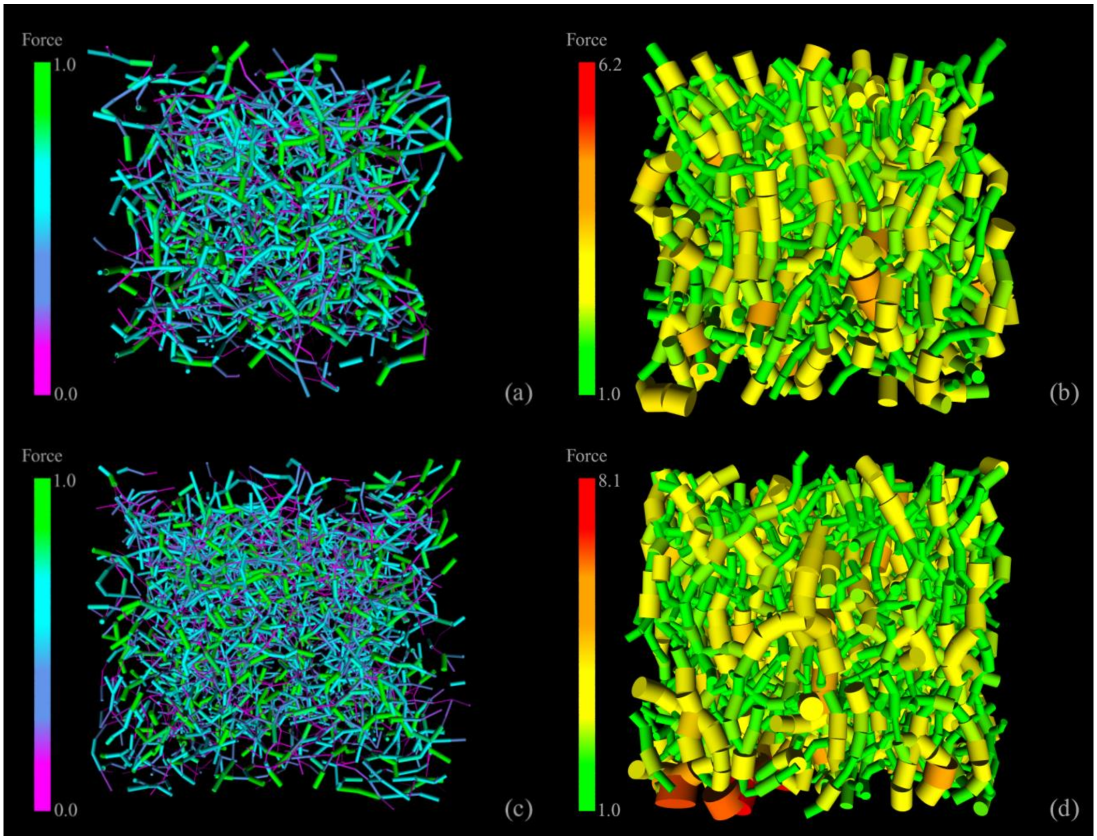

**Figure 3.3** Linear chainlike structures for the monodisperse and bidisperse systems at the pressure of 100MPa.

Figure 3.4(a) displays the fraction of chainlike contacts as a function of pressure in the strong and weak networks for monodisperse and bidisperse systems. It can be observed that there are about 60% of contacts in the strong network are able to form the chainlike structures for both systems, independent of the pressures. In contrast, for both monodisperse and bidisperse systems there are about 32% of contacts in the weak network involve into the chainlike structures at the pressure of 0.001MPa, and the percentage increases to about 45% at the pressure of 100MPa. This dependence of fraction involved in the chainlike structures in the weak network on the pressure indicates that the weak network can reorganize and develop more chainlike structures upon increasing pressure in order to effectively support the stability of strong network at higher pressure. Therefore, these results indicate that not all the contacts in the strong and contact networks are able to constitute the chainlike structures, which qualitatively agrees with the previous 2D DEM simulation results [81]. Moreover, we found this is also true for the weak network, where even less than half of the contacts involved into the chainlike structure. The chainlike structure is more prevalent in the strong network comparing with the weak network. On the other hand, the fraction of contacts involved in the strong network with respect to the total contacts has also been illustrated in Figure 3.4(b). The results show that the strong contacts for bidisperse systems consist of about 37%-40% of total contacts, slightly increasing with the pressures, in agreement with previous 2D contact dynamic simulation results [65]. For the monodisperse system, the fraction of contacts in the strong force network with respect to the total number of contacts is about 39%-42%, comparable with the bidisperse system.

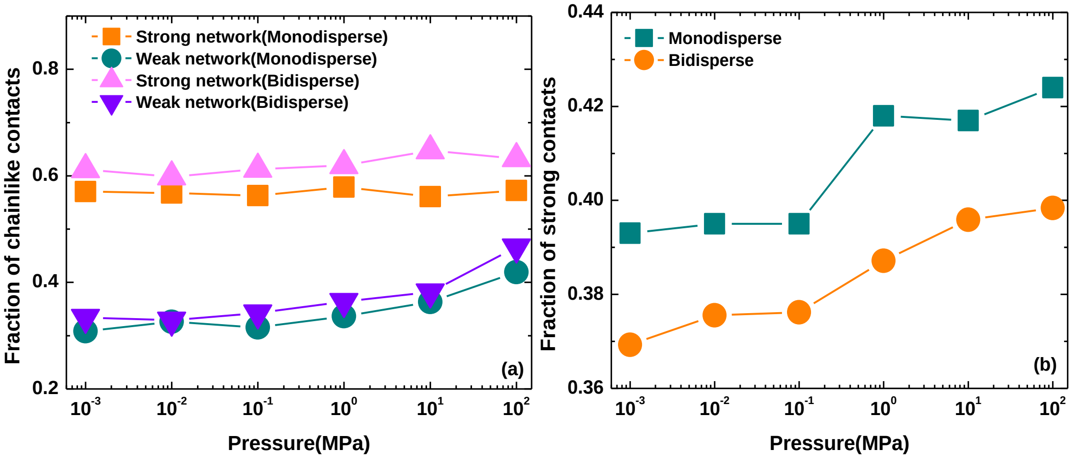

**Figure 3.4** (a) Fraction of chainlike contacts in the strong and weak networks as a function of pressure for monodisperse and bidisperse systems. (b) Fraction of strong contacts with respect to the total contacts as a function of pressure.

### 3.3.2 Various Types of Contacts in Bidisperse System

For bidisperse system, the contact network can be categorized not only depending on the magnitude of contact forces, but also the size of particles in contact, including the contacts constituted by coarse-coarse (CC), coarse-fine (CF), and fine-fine (FF) particles. The corresponding fractions of those specific types of contacts with respect to the total number of contacts have been shown in Figure 3.5(a) as a function of pressure. It can be seen that the fractions of CF contacts are roughly 50% with respect to the total number of contacts and the contacts in bidisperse system are therefore dominated by CF contacts. Similarly, Figure 3.5(b) shows the fractions of specific type of contacts in the strong contact network as a function of pressure. Surprisingly, although about 50% contacts with respect to the total contacts are CF contacts, 60% contacts in the strong contact network are CC contacts. In other words, the CF contacts dominate the total contact network but CC contacts dominate the strong contact network.

Since not all the contacts in the strong network form linear chainlike structure, the fractions of specific contacts in the chainlike structure have also been examined and the results are shown in Figure 3.5(c). It can be seen that CC contacts dominate the chainlike structures as well. Figure 3.5(d) shows the fraction of chainlike contacts in the weak contact network as a function of pressure, indicating that the dominated type of contacts is the CF contacts, which is a strong contrast with the fact that CC contacts dominate the strong contact network.

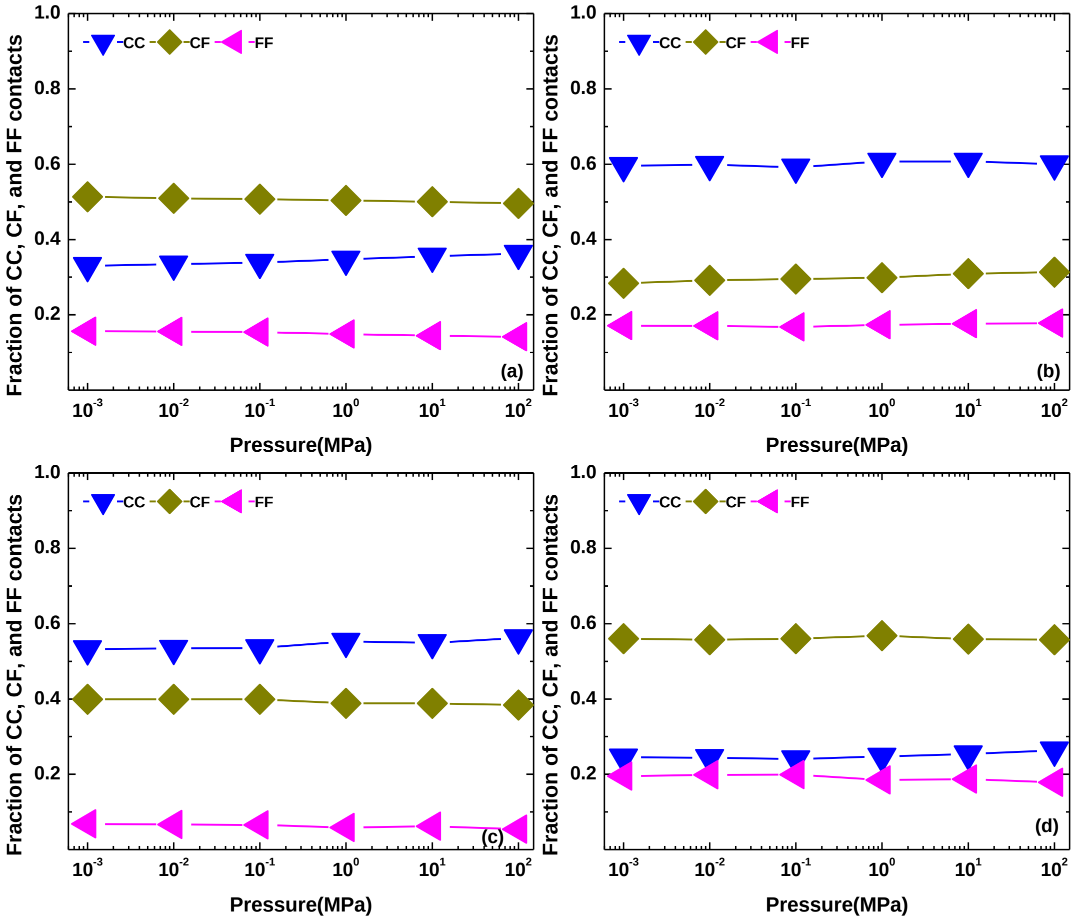

**Figure 3.5** Fraction of coarse-coarse (CC), coarse-fine (CF), and fine-fine (FF) contacts with respect to the total contacts as a function of pressure for bidisperse systems. (b) Fraction of CC, CF, and FF contacts in the strong contact network. (c) Fraction of chainlike structures in the strong network. (d) Fraction of chainlike structures in the weak network.

### 3.3.3 Response of Contact Orientation to Compressive Load

The texture of contact force network is characterized by orientation distribution of contact vectors [15]. The angle $\varphi$ defined in the local spherical coordinate system as the angle between the contact vector and the vertical (parallel to the compressive direction). Therefore, $\varphi=0^{\circ}$ is a vertical contact and $\varphi=90^{\circ}$ is a horizontal contact. Figure 3.6 shows the distribution of angle $\varphi$ as a function of pressure for both monodisperse and bidisperse simulation systems. One of the remarkable outcomes is that the strong and weak contact networks have completely different dynamic response to the external loads. With increasing pressure, the strong contact network develops a peak at around *φ* of 50° for both monodisperse and bidisperse systems. In contrast, the distributions of contact orientation in the weak contact network develop a peak around *φ* of 90° for both simulation systems. Moreover, the probabilities of distribution of contact orientations in the strong network increases for the contact orientation less than 60° and decreases for contact orientation greater than 60°, while the weak network exhibits the opposite trends. When we consider the whole contact ensemble such opposite responses of strong and weak contact networks are swept away by the ensemble average and the total distribution of *φ* for all the contacts is very similar for low and high pressure.

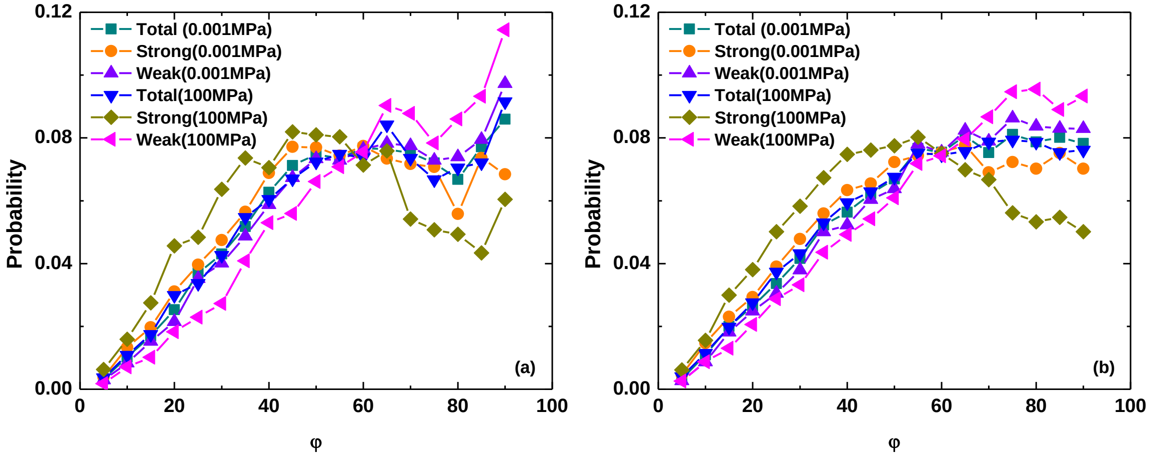

**Figure 3.6** Response of contact orientation in strong and weak networks to external load for both monodisperse and bidisperse systems.

## 3.4 Conclusions

Using DEM simulations, the properties of strong and weak force networks in jammed granular media under compression have been investigated. The particular interests are spatial correlation and distribution of contact angle, chainlike structures in the strong and weak force networks, responses of force networks to the external loads, and statistical analysis of contact forces. The simulation results show that there are about 60% of contacts belonging to the strong network form the chainlike structures. In contrast, there are about 32%-45% of contacts in the weak contact network are able to form the chainlike structures, increasing with increasing pressures. For the bidisperse systems, the total contact network is dominated by the coarse-fine particle contacts; however, coarse-coarse particle contacts dominate the strong contact network, as well as the chainlike structures. In the strong force network the probabilities of contact orientation with respect to the compressive direction increases for the contact orientation less than $60^o$ and decreases for the contact orientation greater than $60^o$, while the weak network exhibits the opposite trends.

# CHAPTER 4

# PARTICLE MIXING BY MAGNETICALLY ASSISTED IMPACTION

## 4.1 Introduction

Recent experimental research shows that magnetically assisted impaction mixing (MAIM) is an effective method to mix sub-micron particles [85] and can be also used to mix nano-particles at the sub-agglomerate particle scale due to the strong shear that can be generated [86]. The effects of different operating parameters, such as magnet size, processing time, and number of magnets have also been examined to shed light on the effectiveness of the MAIM device [86]. Unlike common industrial mixing methods that use harmful and environmentally unfriendly solvents [87, 88], MAIM is a dry mixing process. By avoiding the use of solvents, there is no need for additional processing steps of filtration and drying, which can be costly and can lead to caking or segregation. The previously published experimental study [86] showed that the homogeneity of mixing (HoM), defined as the complement of the Intensity of Segregation from Danckwerts [89], improved with an increase in the number of magnets and processing time. The results suggest that those two variables are important scaling parameters. Thus in order to understand the MAIM process for its use in industrial applications, and validating previous experimental results, the system model of the deagglomeration of cohesive particles via magnetic assistance is considered in this paper. It is expected to have a much broader impact because magnetically assisted methods have also been shown to promote flow [90], fluidization [10], and dry surface coating with nano-particles [91, 92], making it a versatile device, suitable for various fine, adhesive, and cohesive powder processing.

In this section, DEM simulations are employed to study the mixing of cohesive particles under magnetically assisted impaction, which includes the cohesive forces based on the JKR model and includes the formation and subsequent mixing of agglomerates. Different factors such as surface energy, magnet size, mass ratio, and processing time are considered to determine how each would affect the mixture homogeneity. Furthermore, the relationship between HoM and the collision parameters is analyzed to identify the most critical variables, such as collision number and collision energy. Simulation results are also compared with the previously obtained MAIM experimental results and they qualitatively agree with each other, thereby validating the MAIM DEM model [86].

## 4.2 Model and Initial Parameters

### 4.2.1 Initial Parameters of Simulation

In this study, DEM modeling based on the soft sphere model is used to simulate magnetically assisted impaction mixing. In soft sphere model, the particles can experience small deformation, which can be used to calculate the contact force. Initially, magnets and non-magnets are generated randomly, without overlap between any two of them, in a cylinder with the radius of 6.2 millimeter and length of 27.3 millimeter. The volume is scaled in proportion to the amount of the sample used in the jar, when compared to the experimental mass [7]. Therefore, within a unit volume, mass of the magnets and sample is the same in the simulation as with the physical experiment. The initial parameters for the simulations are listed in Table 4.1. The size of the non-magnets, intended to represent a large, non-fragmenting sub-agglomerate of the nano-particles, is kept at 0.2 mm to keep the simulation time reasonable. In addition, since our model is more time-consuming due to the involvement of the magnetic force, softer particles are used as commonly done [93, 94] in order to avoid making time steps too small, and hence artificially smaller elastic constant of particles is employed.

**Table 4.1** Initial Parameters and Material Properties for Simulation

| Name | Value | Unit |
|---|---|---|
| Radius of cylinder | 6.2 | mm |
| Height of cylinder | 27.3 | mm |
| Number of magnets | 2-60 | / |
| Number of non-magnets | 2000 | / |
| Number of agglomerates | 100 | / |
| Magnetization of barium ferrite | 37 | A·m$^2$/kg |
| Maximum magnetic flux density of external magnetic field | 70 | mT |
| Frequency of external magnetic field | 60 | Hertz |
| Density of magnets | 5000 | kg/m$^3$ |
| Density of non-magnets | 5000 | kg/m$^3$ |
| Diameter of magnets | 644-2000 | micrometer |
| Diameter of non-magnets | 200 | micrometer |
| Shear modulus of magnets | 7.0e6 | Pa |
| Shear modulus of non-magnets | 2.5e6 | Pa |
| Shear modulus of geometry | 7.0e6 | Pa |
| Poisson ratio of magnets, non-magnets, and geometry | 0.3 | / |
| Rolling friction coefficient | 0.01 | / |
| Static friction coefficient(magnets and magnets, geometry) | 0.3 | / |
| Static friction coefficient(magnets and non-magnets) | 0.4 | / |
| Static friction coefficient(non-magnets and non-magnets, geometry) | 0.4 | / |
| Restitution coefficient(magnets and magnets, geometry) | 0.8 | / |
| Restitution coefficient(magnets and non-magnets) | 0.7 | / |
| Restitution coefficient(non-magnets and non-magnets, geometry) | 0.7 | / |
| Surface energy between non magnets and non-magnets | 0.1-0.3 | J/m$^2$ |
| Surface energy between non magnets and geometry | 0.1 | J/m$^2$ |
| Time step | $2.0\times10^{-6}$ | s |

### 4.2.2 Contact Model and Governing Equations

Every particle can experience translational and rotational motion in DEM simulations. Rotational motion is very critical for accurately modeling the effect of the magnetic field on the magnetic particles, which are modeled as magnetic dipoles. During their movement, magnetic or non-magnetic particles can collide with each other and exchange energy and momentum. The contact model will define how the particles interact when they make contact with other particles or the geometry. The motion of individual particles can be described by Newton's second law of motion. The equations governing translational and rotational motion of particle is written as follows:

$$m_i \frac{d^2\vec{r}_i}{dt^2} = \vec{F}_i^{con} + \vec{F}_i^{gra} + \vec{F}_i^{mag} \tag{4.1}$$

$$I_i \frac{d\vec{\omega}_i}{dt} = \vec{T}_i^{mec} + \vec{T}_i^{mag} \tag{4.2}$$

where $m_i$ and $\vec{r}_i$ is mass and the position vector of particle *i*, respectively. Variable *t* represents time, and $\vec{F}_i^{con}$, $\vec{F}_i^{gra}$ and $\vec{F}_i^{mag}$ are the contact force, gravitational force, and magnetic force, respectively of particle *i*. $I_i$ is the moment of inertia, $\vec{\omega}_i$ is the angular velocity of particle *i*, and $\vec{T}_i^{mec}$ is torque acting on the particle *i* induced by tangential contact force and rolling friction. $\vec{T}_i^{mag}$ is the torque induced by magnetic force. For the perfect sphere, $I_i$ is $\frac{2}{5} m_i R_i^2$, where $R_i$ is the radius of particle *i*.

Once the force and torque are known, then Equations 4.1 and 4.2 can be solved numerically. As a result, the velocity and position of every individual particle can be calculated. In the DEM simulation, contact force can be further divided into the normal contact force and the tangential contact force [19, 95]. So in Equation 4.1, the contact force $\vec{F}_i^{con}$ can be written:

$$\vec{F}_i^{con} = \sum_{j \neq i}^{N} (\vec{F}_{ij-n}^{con} + \vec{F}_{ij-t}^{con}) \tag{4.3}$$

$\vec{F}_{ij-n}^{con}$ is the normal contact force and $\vec{F}_{ij-t}^{con}$ is tangential contact force. The total contact force is summed over the $N$ particles in contact with particle $i$. The normal contact force is calculated by the sum of two components. The first component, the cohesive force, is based on the JKR model. The second component, the dissipative component, is induced by the dissipation of energy during collision, which is related with impact velocity.

$$\vec{F}_{ij-n}^{con} = \vec{F}_{ij-n}^{jkr} + \vec{F}_{ij-n}^{dam} \tag{4.4}$$

In the DEM simulation, there are different methods to add cohesive forces, such as, liquid bridge force [96-98], constant surface energy [8], or van der Waals force [12, 26]. In this work, the cohesive force is based on JKR theory [20]. JKR model has been widely used in many DEM model considering cohesive force [99-104], and the more accurate way to depict the influence of cohesion and associated forces have been proposed by Savkoor and Thornton group [104-106]. In our paper, a modified JKR model is used for the sake of simplicity, also used in a recent paper [107]. The main simplification is that according to this model, the contact will break once the normal overlap becomes zero. Therefore, the force required to break the contact equals the 8/9 of pull-off force, which is representative of the JKR theory [20, 107]. The cohesive forces between each non-magnetic particle and between non-magnetic particles and the geometry were considered. The amplitude of cohesive force can be easily adjusted by varying the surface energy of the particles. The normal force based on JKR model can be given:

$$\begin{aligned} \vec{F}_{ij-n}^{jkr} &= -(\frac{4E^*}{3R^*}a^3 - 4\sqrt{\pi\gamma E^*}a^{\frac{3}{2}})\vec{n}_{ij} \\ a^4 - 2R^*\delta_n a^2 &- \frac{4\pi\gamma}{E^*}R^{*^2}a + R^{*^2}\delta_n{}^2 = 0 \end{aligned} \tag{4.5}$$

where $E^*$ is equivalent Young's modulus and $R^*$ is equivalent radius. $\delta_n$ is the normal overlap. $\vec{n}_{ij}$ is the unit vector from the center of particle $i$ to the center of particle $j$, $a$ is contact radius and $\gamma$ is surface energy. $E^*$ and $R^*$ are defined as,

$$\frac{1}{E^*} = \frac{1-\upsilon_i^2}{E_i} + \frac{1-\upsilon_j^2}{E_j} \tag{4.6}$$

$$\frac{1}{R^*} = \frac{1}{R_i} + \frac{1}{R_j} \tag{4.7}$$

with $\upsilon_i$, $E_i$, $R_i$ and $\upsilon_j$, $E_j$, $R_j$ being the Poisson ratio, Young's modulus, and radius of every sphere in contact, respectively. The normal overlap, $\delta_n$, is given by:

$$\delta_n = ((R_i + R_j) - |\vec{r}_i - \vec{r}_j|) \tag{4.8}$$

where vector $\vec{r}_i$ and $\vec{r}_j$ represent the position of particle *i* and particle *j*.

The physical mechanism of energy loss during the collision is complicated and depends on the material properties and the types of collision. For examples, in the plastic impact, the energy loss is mainly due to the plastic deformation [108], however, even when the collision between particles is in elastic regime, the energy can be dissipated by elastic waves [108, 109]. There are several approaches to capturing energy dissipation in DEM, most popular one includes use of a dashpot originally proposed by Cundall and Strack [2] and used in many papers. This model provides a simple method of capturing the intrinsic elastic and dissipated characteristics of the particle assembly, and it is a reasonable balance between computation costs and accuracy.

In the presence of cohesion represented by JKR model, accurate representation of the dissipation force becomes even more complicated and, to our knowledge, there is no generally well accepted model. For example, the energy dissipation is associated with the time derivative of contact force in [110]. On the other hand, normal overlap or contact area are involved with estimation of dissipation force in other references [111, 112]. In this paper, the main objective is to examine the use of agglomerates in mixing of nanoparticles, that are cohesive, and hence a simplified model, which has been used in previous publications, was selected due to its computational efficiency and numerical stability [13, 113]. Accordingly, the energy dissipation can be simulated by introducing a velocity-dependent damping force [13, 113, 114]. The damping force $\vec{F}_{ij-n}^{dam}$ is given by [114]:

$$\vec{F}_{ij-n}^{dam} = -2\sqrt{\frac{5}{6}}\beta\sqrt{S_n m^*}\vec{v}_n^{rel} \tag{4.9}$$

$$\beta = \frac{\ln e}{\sqrt{\ln^2 e + \pi^2}} \tag{4.10}$$

$$S_n = 2E^*\sqrt{R^*\delta_n} \tag{4.11}$$

where the reduced mass $m^*$ is defined in terms of the masses of the individual contacting particles, $m_1$ and $m_2$, as $1/m^* = 1/m_1 + 1/m_2$ , $\vec{v}_n^{rel}$ is normal component of relative velocity, and $e$ is the coefficient of restitution. The parameters in the Equation 4.11 $R^*$, and $\delta_n$ have been defined in the Equation 4.7, and Equation 4.8 as the equivalent radius and normal overlap, respectively. $\vec{v}_n^{rel}$ is given by:

$$\begin{aligned} \vec{v}_n^{rel} &= (\vec{v}_{ij} \cdot \vec{n}_{ij})\vec{n}_{ij} \\ \vec{v}_{ij} &= \vec{v}_i - \vec{v}_j \end{aligned} \tag{4.12}$$

where $\vec{v}_i$, $\vec{v}_j$ is the velocity of particle *i* and particle *j*, respectively.

Due to the relative tangential velocity of contacting particles at the contact point, there will be tangential force on the contacting particles, which is calculated by:

$$\begin{aligned} \vec{F}_{ij-t}^{con} &= -S_t \delta_t \vec{t}_{ij} + \vec{F}_{ij-t}^{dam} \\ S_t &= 8G^* \sqrt{R^* \delta_n} \end{aligned} \tag{4.13}$$

where $S_t$ is tangential stiffness, $\delta_t$ is tangential displacement. $\vec{t}_{ij}$ is the unit tangential vector, $G^*$ is equivalent shear modulus, $\vec{F}_t^{dam}$ is tangential damping force which is induced by the dissipation of energy. The tangential displacement is calculated by integrating the relative tangential velocity during the whole time of contact:

$$\vec{\delta}_t = \int \vec{v}_t^{rel} dt \tag{4.14}$$

$$\vec{v}_t^{rel} = \vec{v}_{ij} - (\vec{v}_{ij} \cdot \vec{n}_{ij})\vec{n}_{ij} + (\vec{\omega}_i \times R_i \vec{n}_{ij} + \vec{\omega}_j \times R_j \vec{n}_{ij}) \tag{4.15}$$

Tangential damping force is given by:

$$\vec{F}_{ij-t}^{dam} = -2\sqrt{\frac{5}{6}}\beta\sqrt{S_t m^*}\vec{v}_t^{rel} \tag{4.16}$$

where $\vec{v}_t^{rel}$ is the relative tangential velocity.

The maximum tangential force is limited by Coulomb friction:

$$|\vec{F}_{ij-t}^{con}| \le \mu_s |\vec{F}_{ij-n}^{con}| \tag{4.17}$$

where $\mu_s$ is static friction coefficient. In the presence of cohesive forces, the normal force can no longer be directly used in Equation 4.17 [102]. In this paper, the normal force for non-cohesive contact force is used to determine tangential behavior. It should be pointed out that the Equation 4.17 is approximately used to describe the critical tangential force for the sake of simplicity. The detailed study of effect of cohesion on tangential sliding has been conducted in the references [104-106]. Thornton proposed a modified equation to describe the sliding condition in the presence of cohesion and was given by [105]:

$$|\vec{F}_{ij-t}^{con}| \le \mu_s |\vec{F}_{ij-n}^{con} + 2F_c| \tag{4.18}$$

where $F_c = 3\pi\gamma R^*$ is the pull off force in the JKR model. In Equation 4.18, quantities, $\vec{F}_{ij-t}^{con}$, $\vec{F}_{ij-n}^{con}$, and $\mu_s$ have been defined in Equation 4.3 and Equation 4.17 as the tangential contact force, normal contact force, and the static friction coefficient, respectively.

However, as we will see in the results, the collisions between magnets and non-magnets play dominating role in the process of mixing, and those interactions (between magnets and non-magnets) are described using model without cohesion, which will minimize the possible inaccuracies associated by use of Equation 4.17 on our simulation results for various initial conditions. The gravitational force $\vec{F}_i^{gra}$ is equal to the product of mass and the gravitational acceleration.

The torque is the result of the tangential component of contact force and it will cause the rotational motion of particles. In addition, the torque induced by the rolling friction is considered [115], although its effect is expected to be low and not incorporating it would not substantially change the overall outcome of these simulations since the small rolling friction coefficient (0.01) is used. However, there are several reasons for introducing the rolling friction in our simulation. For example, the relative rotation between contacting particles will cause rolling resistance due to the elastic hysteresis [116]. In addition, the rolling friction can also be produced by the micro-slip and friction on the contact surface arising from the difference of curvature of the contacting surfaces and their different mechanical properties [117]. Rolling friction has been included in many previously published DEM simulations [12, 13, 26, 118], and different models for estimation are available [118, 119]. Assessing and testing which rolling friction model is better than the others, when it comes to cohesive particles, is outside of the scope of this paper. In this work, the torque induced by rolling friction is adopted from [115] , which has been widely used before [12, 26]. The equations to calculate the torques are given by:

$$\begin{aligned} \vec{T}_i^{mec} &= \vec{T}_{i-\tan}^{mec} + \vec{T}_{i-rol}^{mec} \\ \vec{T}_{i-\tan}^{mec} &= \sum_{j\neq i}^{N} (R_i \vec{n}_{ij} \times \vec{F}_{ij-t}^{con}) \\ \vec{T}_{i-rol}^{mec} &= \sum_{j\neq i}^{N} -\mu_r \, |\vec{F}_{ij-n}^{con}| \, R_i \vec{\omega}_i / |\omega_i| \end{aligned} \tag{4.19}$$

where $\mu_r$ is rolling friction coefficient.

### 4.2.3 Force and Torque due to Magnetic Field

The influence of electrostatic fields on the motion of particles has been widely studied [120-122]. However, specifically modeling the magnetic particles in external fields has not been reported, except for the preliminary models [123, 124]. In this paper, the model is further refined and is applied for magnetically assisted impact mixing. In order to simulate the motion of magnets under an external magnetic field, it is necessary to include the magnetic force into the DEM model. For the sake of simplicity, the external magnetic field is assumed to be uniform in the jar, and the magnetic particles are treated as small magnetic dipoles. The force $\vec{F}_i$ and torque $\vec{T}_i^{mag}$ acting on magnetic particle *i* can be given by:

$$\vec{F}_i^{mag} = (\vec{m}_i \cdot \nabla)\vec{B}_{dip} \tag{4.20}$$

$$\vec{T}_i^{mag} = \vec{m}_i \times (\vec{B}_{ext} + \vec{B}_{dip}) \tag{4.21}$$

where $\vec{m}_i$ is the magnetic dipole moment, $\vec{B}_{dip}$ is the magnetic flux density at the position of magnetic particle *i* induced by all the other magnetic particles, and $\vec{B}_{ext}$ is the external magnetic flux density. The direction of the external magnetic field oscillates with time, but the amplitude of the magnetic field is constant. Due to uniform distribution of external magnetic field, it will not contribute to the magnetic force. $\vec{B}_{dip}$ and $\vec{B}_{ext}$ are given by:

$$\vec{B}_{dip} = \sum_{j \neq i}^{N_{mag}} \frac{\mu_0}{4\pi r_{ji}^{\,5}} [3(\vec{m}_j \cdot \vec{r}_{ji})\vec{r}_{ji} - r_{ji}^{\,2}\vec{m}_j)] \tag{4.22}$$

$$\vec{B}_{ext} = B_0 \sin(2\pi ft)\vec{k} \tag{4.23}$$

$$\vec{r}_{ji} = \vec{r}_i - \vec{r}_j \tag{4.24}$$

where $\mu_0$ is the permeability in vacuum and vector $\vec{k}$ represents the direction of the external magnetic field [125]. $B_0$ is constant and represents the amplitude of external magnetic field. *f* is the frequency of the oscillating external magnetic field. Spatial orientation of particles changes with time due to the presence of angular velocity. Consequently, the magnetic dipole moments of magnets need to be updated with time:

$$\vec{m}_i(t_{t1+dt}) = \vec{R}_{t1} \times \vec{m}_i(t_1) \tag{4.25}$$

where $\vec{m}_i(t_{t1+dt})$ , $\vec{m}_i(t_1)$ represent the magnetic dipole moment of magnetic particle *i* at next and current time step of DEM. $\vec{R}_{t1}$ is the rotation matrix and is calculated using singularity-free quaternions [126]. In order to validate the DEM program, the benchmark tests have been done in the absence of external magnetic field and in the presence of static external magnetic field. The results, although not included here for the sake of brevity, show the magnets form the chain-like structures and agglomerates when there is no external magnetic field. In contrast, for a static external magnetic field, the magnets align themselves along the direction of the field. These phenomena qualitatively agree with previous results [16], validating the code.

### 4.2.4 The Formation of Stable Agglomerates

In this study, the first step of the mixing process is to form stable agglomerates. Nano-particles, forming hierarchical, fractal, agglomerates, consist of a multitude of sub-agglomerates, each containing of millions of primary particles. Thus detailed modeling of even a single realistic agglomerate is not possible at current computational capabilities [86, 127-130]. However, as a first approximation, individual sub-agglomerates may be modeled as primary particles (non-magnets in this paper) that subsequently form the agglomerates. This scheme also allows for directly modeling the mixing of micron-sized particles that also form agglomerates due to cohesive forces. The process of forming agglomerates is similar to previously published work [131-133]. First, some of the non-magnet particles within the simulation are chosen randomly as the cores of agglomerates. Then a centripetal force is introduced in order to drive the other non-magnet particles move towards those cores to form roughly spherical assemblies, which consequently constitute the agglomerates. The amplitude of the centripetal force is equal to the force of gravity on the non-magnet particles. After a while, the cohesive force is added gradually from zero to the desired value, while the centripetal force will be removed gradually from the set value to zero. After relaxation, the gravitational force is added gradually. When all the particles settle down on the bottom of the jar, the magnetic force is applied, which will act on all magnetic particles. The contact number, defined as average number of contacts per particle, and the average kinetic energy are used to quantity if the agglomerates are stable or not. Simulation results show that the contact number and kinetic energy have reached a stable value prior to the addition of the magnetic force. There are totally one-hundred agglomerates consisting of 20 primary particles. These agglomerates are also coded so that half belong to one constituent in the mixture, and the other half to the other constituent in the mixture. The average contact number is 4.899, for a surface energy of 0.3J/m$^2$ and it will decrease with increasing surface energy because the higher cohesive force between particles induced by higher surface energy will prevent the particles from flowing/moving freely, hence they cannot pack well, signifying higher porosity within the agglomerate. Snapshots at different times, corresponding to the formation of agglomerates, are shown in Figure 4.1. Figure 4.1(a) shows the initial configuration of non-magnets and magnets. Initially, magnets and non-magnets are located at the top and the bottom of the jar, respectively. Figure 4.1(b) shows that the non-magnet particles begin to move towards their own cores of agglomerates under the centripetal force. Figure 4.1(c) shows that the steady-state agglomerations with two different kinds of colors have been formed. Figure 4.1(d) shows the steady-state agglomerations settle down at the bottom of simulation jar and the external magnetic force has been exerted.

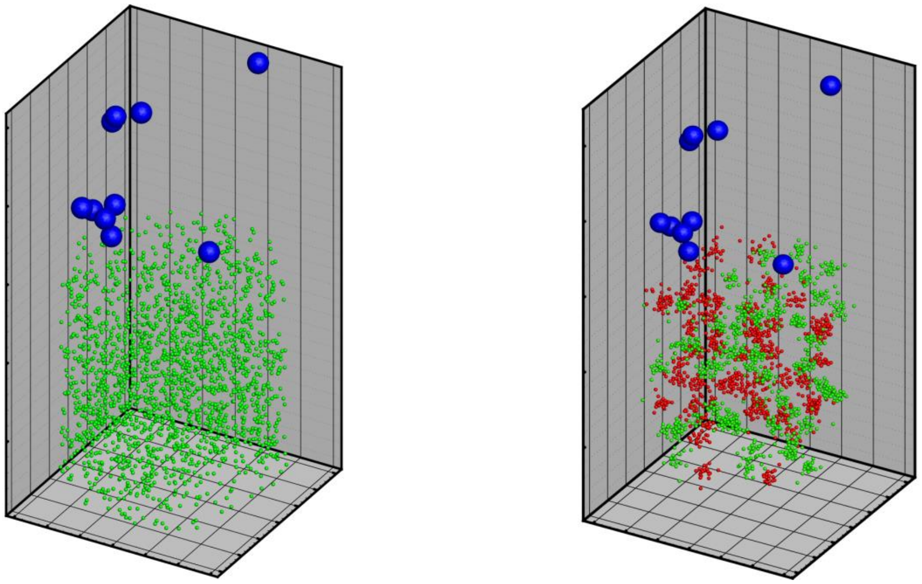

(a) 0 second (b) 1 second

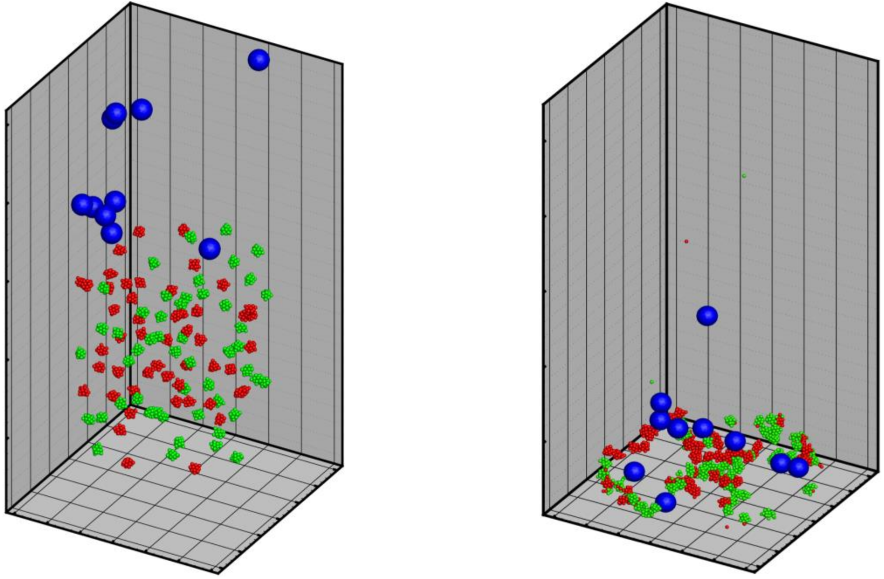

(c) 4.0 second (d) 6.04 second

**Figure 4.1** The schematic of simulation model under different. Blue represents magnets, red and green represent non-magnets. (a) 0 second, (b) 1 second, (c) 4.0 second, (d) 6.04 second.

### 4.2.5 The Index of Mixing

There are different parameters available to quantify the degree of mixing in literature [134].

In this work, relative standard deviation (RSD) is used to quantify the homogeneity of mixing (HoM), which has been widely used before [135-137]. RSD can be calculated as follow:

$$RSD = \frac{\sigma}{\bar{x}} \times 100\% \qquad \sigma = \sqrt{\frac{\sum_{i=1}^{M} (\bar{x} - x_i)^2}{M - 1}} \tag{4.26}$$

where $M$ is the total number of samples, $\bar{x}$ is the average concentration of all the samples, and $x_i$ is the concentration of each individual sample.

As previously mentioned, during the simulation, the color of half of the agglomerates was designated as red and the other half of agglomerates was designated as blue. At each time step, samples consisting of one random particle and its neighboring particles were selected. Then the concentration of color can be calculated. The number of neighbors of non-magnets will define the scale of scrutiny. It should be noted that mixing problems can be masked due to an unsuitable scale of scrutiny [138]. In this paper, the mixing scale is slightly smaller than the scale of the agglomerates. Accordingly, six neighbors are used to calculate the RSD, and hence proper mixing information may be obtained because the initial agglomerate contains 20 primary particles. In every time step, 500 samples are chosen randomly to calculate the relative standard deviation.

The theoretical asymptotic value of RSD corresponding to a completely random binary mixture is defined as

$$RSD_r = \frac{\sigma_r}{\bar{x}} \times 100\% \tag{4.27}$$

$$\sigma_r = \sqrt{\frac{p(1-p)}{n}} \tag{4.28}$$

where $p$ represents the concentration of one specific particle type, either red or blue particles [139]. In our simulation, the total number of particles for each constituent are equal, so $p$ = 50%. Here, $n$ denotes the number of particles in each sample. Further, HoM is defined as

$$HoM = 1 - RSD \tag{4.29}$$

in order to quantify the homogeneity of mixing. $HoM_r$, corresponding to the $RSD_r$, will be about 59.2% for a perfectly random mixture. It is noted that in the literature, quantification of homogeneity index, or its complement the segregation index, is done using several different parameters, even though many of those are based on the concept of the standard deviation. Therefore, depending on a specific definition employed for quantification of the homogeneity, the theoretical asymptotic values for perfect random mixture (or completely segregated mixture) will be different for different definitions. For example, in a previously published paper, the value for homogeneity of mixing for perfectly random mixture is 1 (and 0 for completely segregated mixture) [86]. In contrast, according to another definition, the asymptotic values could be 0 and 0.5 corresponding to the perfect random mixture and completely segregated mixtures [140]. The range of mixture homogeneity employed in this paper is between 0.592 and 0, corresponding to the perfect random mixture and completely segregated mixtures. While the values differ based on the definitions employed, the issue of importance in the present study is to compare the relative trends observed between the different cases, and also between the simulations and physical experiments. Therefore, in spite of the differing definitions in different studies, the outcome and conclusions are not expected to be affected.

## 4.3 Results and Discussion

### 4.3.1 The Effect of Magnet Size on the Homogeneity of Mixing

The experimental results obtained by MAIM show that the smaller magnets will lead to the higher homogeneity of mixing value given a fixed mass ratio [86]. In order to study the effect of magnet size on the homogeneity of mixing, the magnet size is changed for fixed magnet-to-sample mass ratio. Four magnet sizes are chosen in the simulation; three were based on the averaged size used in the previous experiment (811µm, 1169µm, and 2000µm) [7], and one additional magnet size of 644µm. The mass ratio is fixed at 1:1 and the surface energy of the non-magnetic particles was $0.1 J/m^2$, $0.2 J/m^2$, and $0.3 J/m^2$, in Figures 4.2(a), (b), and (c), respectively. The figures are plotted as HoM versus processing time while the results for each magnet size has been represented as the total number of magnets present in the simulation. The higher number of magnets corresponds to the smallest magnet size and the total number increases for each decreasing magnet size. As expected, for all three values of surface energy, HoM increases with the increasing processing time and eventually achieves the theoretical asymptotic value $HoM_r$, which indicates the perfect random mixing has been achieved at the selected scale of scrutiny. In order to quantify the speed of mixing, the slopes of each HoM curve were calculated, shown in Figure 4.2(d). The slope can be obtained analytically by means of fitting the HoM data, for a specific HoM value. According to Figure 4.2(d), at HoM of 40%, the speed of mixing increases with increasing number of magnets, for surface energies of 0.1J/m$^2$ and 0.2J/m$^2$. With increasing surface energy to 0.3J/m$^2$, the difference between 10, 30 and 60 magnets is not significant. Moreover, the speed of mixing corresponding to 60 magnets (644μm) is slightly lower than the 30 magnets (811μm). This result indicates that the smaller magnets are no longer as efficient as the larger magnet sizes in mixing non-magnetic particles with high surface energy.

Understandably, the slope will change with varying HoM values. As mentioned before, Figure 4.2(d) only shows the slope corresponding to a HoM value of 40%. Several different HoM values were also checked, although not presented here for the sake of brevity, and the results show that the qualitative phenomena are similar throughout and they support the conclusions above.

When comparing the time required in the physical experiment to homogenize the materials, the homogeneity of mixing can be achieved much faster in the simulation than in actual experiments. For example, in one experiment, a time of approximately 300 seconds was required to achieve a desired homogeneity of mixing for 1:1 mass ratio with the medium sized magnets [86]. However, in the simulation, less than ten seconds is required for the 1169μm magnets, with a surface energy of 0.2J/m$^2$, to reach a desired equivalence. A similar phenomenon is also observed in another DEM simulation [141]. In the present case, this is most likely because the simulations are actually only simulating the mixing of sub-agglomerates while the physical experiment involved mixing of nano-particles. Another related reason is that, in the simulation, the number of non-magnetic particles in the agglomerates is much smaller when compared with the experiment. This is because the size of the non-magnets is limited to how small they can be in a simulation. In order to test the effect of the size of non-magnets on the homogeneity, the radius of non-magnets was changed from approximately 100μm to 79μm (volume decrease of 50%). In this simulation, the numbers of non-magnets are doubled to keep the mass ratio constant. In this new system, there are a total of 4000 non-magnets that form 100 individual agglomerates. All of the other simulation conditions are kept exactly the same. The simulation results obtained at ten second of mixing, for a magnet size of 811μm and the surface energy of 0.3J/m$^2$, results in HoM values of 46.1% and 56.1%, for 4000 and 2000 non-magnetic particles, respectively. This indicates that by increasing the number of non-magnets, for a fixed mass, the speed of mixing will be slower even for the same magnet-to-sample mass ratios, and hence it explains the differences in the actual mixing time of physical experiments versus simulations. Notwithstanding, the trends observed in the simulations qualitatively match those of the physical experiments.

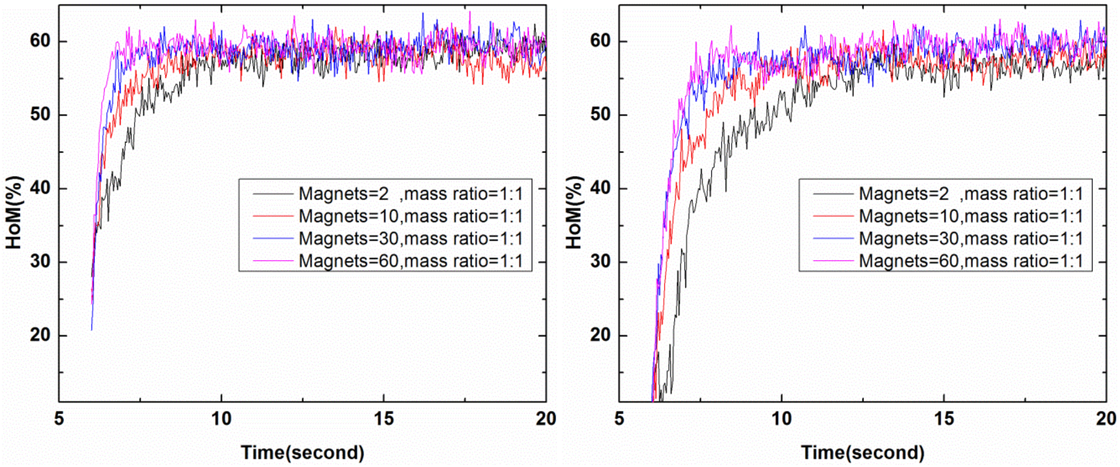

(a)Surface energy=0.1J/m$^2$ (b) Surface energy=0.2J/m$^2$

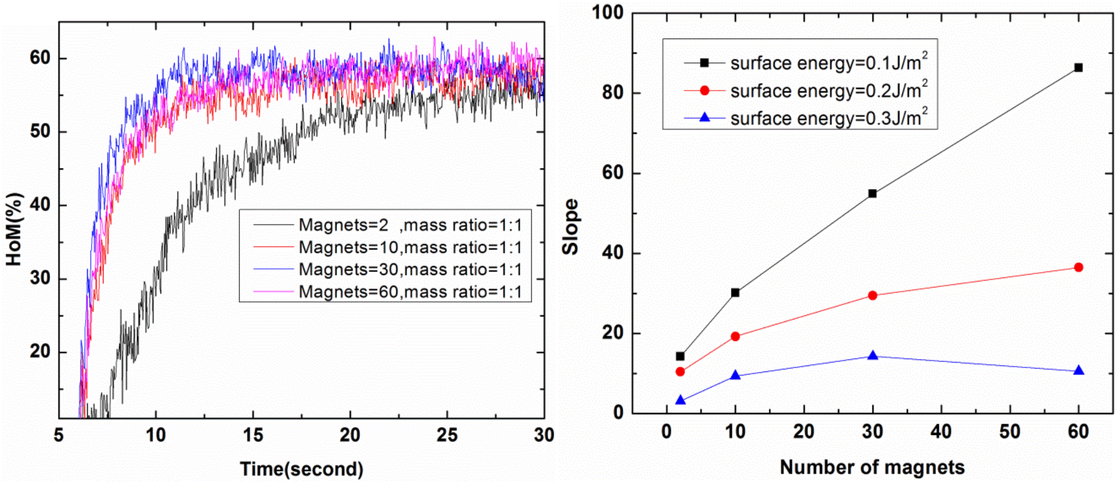

(c) Surface energy=0.3J/m$^2$ (d)

**Figure 4.2** The effect of magnets number on HoM under different surface energies.

### 4.3.2 The Effect of Surface Energy on Homogeneity of Mixing

Figures 4.3(a)-(d) show the effect of surface energy on the HoM for different magnet sizes. According to the results, as may be expected, for all four different magnet sizes, the agglomerates with a higher surface energy requires a longer time to achieve the HoM$_r$ value. For example, when the magnet size is 1169μm, the particles with surface energies of 0.1J/m$^2$, 0.2J/m$^2$, and 0.3J/m$^2$ achieve HoM$_r$ at about ten, thirteen, and eighteen seconds, respectively. For the magnet sizes of 2000μm, 811μm, and 644μm, the results follow similar trends as the results for the 1169μm magnet size. A phenomenological explanation is that strong cohesive force induced by high surface energy makes it hard to detach the particles from agglomerates. Therefore, higher collision numbers and collision energy would be required from the magnets to drive the mixing.

It is worth mentioning that other DEM simulation results show that the cohesive force will not always make the mixing worse and the mixing can be enhanced at intermediate levels of cohesion [8, 142]. While those results are valid for their chosen configurations or purpose, our numerical experiments are intended to better understand highly cohesive particles. As a comparison with previous studies, the granular Bond numbers for the non-magnetic particles in the present study are about 918, 1838, and 2759, for the surface energy values of 0.1J/m$^2$, 0.2J/m$^2$, and 0.3J/m$^2$, respectively. It is noted that the Bond numbers presented here are based on the ratio of attractive force divided by particle weight. The attractive force here is not the total force in the JKR interactions, which also includes the repulsive component that reduces the total adhesion. For reference, if one used total JKR force, the maximum value of Bond number for case of 0.3J/m$^2$ will be about 688 instead of 2759; even then it is higher than those used in the previous studies. Therefore, in our simulations, when surface energy, i.e., cohesive force, is increased, obtaining a homogeneous mixture will require longer mixing times. Previous studies also did not incorporate the effect of agglomerates on mixing homogeneity, which could also be another possible reason for the difference. Although it would be interesting to examine a wider range of surface energy values in the present simulations, it is more instructive to examine various parameters and the process of agglomerate fragmentation in more detail.

We note that simulating the wider range of values, particularly higher values of surface energy, also requires much longer simulation times to achieve the perfect random mixing.

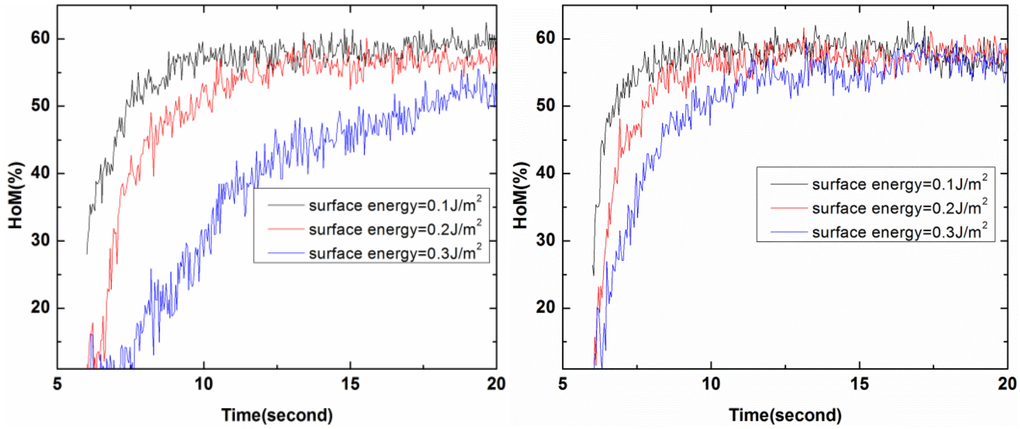

(a) 2 magnets(2000µm) (b) 10 magnets(1169µm)

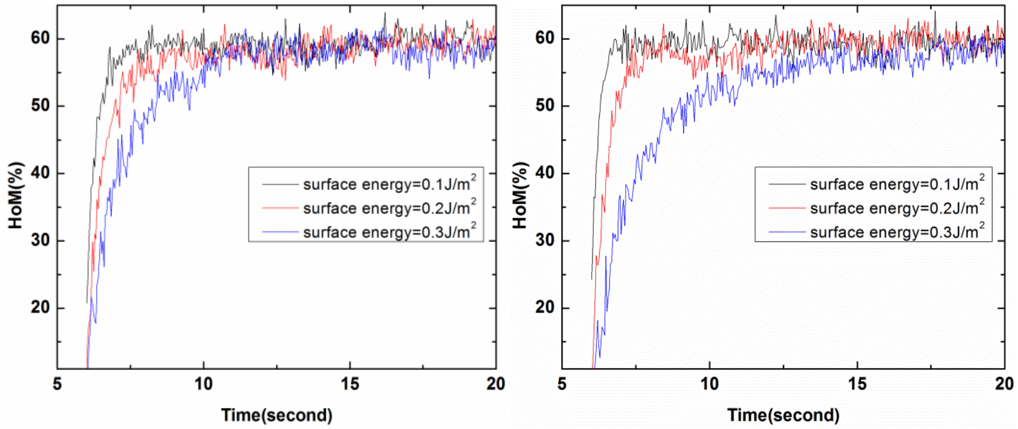

(c) 30 magnets (811µm) (d) 60 magnets (644µm)

**Figure 4.3** The effect of surface energy on HoM under different magnets size.

### 4.3.3 The Effect of Mass Ratio on Homogeneity of Mixing

The effect of magnet-to-sample mass ratio on the homogeneity of mixing is examined next. Experimental results indicated that by increasing the mass ratio, the homogeneity of mixing will also increase under similar processing conditions [86]. In current simulation, three different magnet-to-sample mass ratios (1:1, 2:1, 4:1) are used to simulate the effect of the mass ratio on the mixing process. In Figures 4.4(a)-(d), the results show that for the different magnet sizes studied, increasing the mass ratio will increase the speed of mixing and the larger mass ratio requires less processing time to achieve a steady state for mixture homogeneity. For example, when the 1169μm magnets size are used, $HoM_r$ can be achieved at about eight, eleven, and thirteen seconds, corresponding to mass ratio 4:1, 2:1, and 1:1, respectively. Thus qualitatively, the effect of the mass ratio on the mixture homogeneity agrees with the previously published experimental results [86].

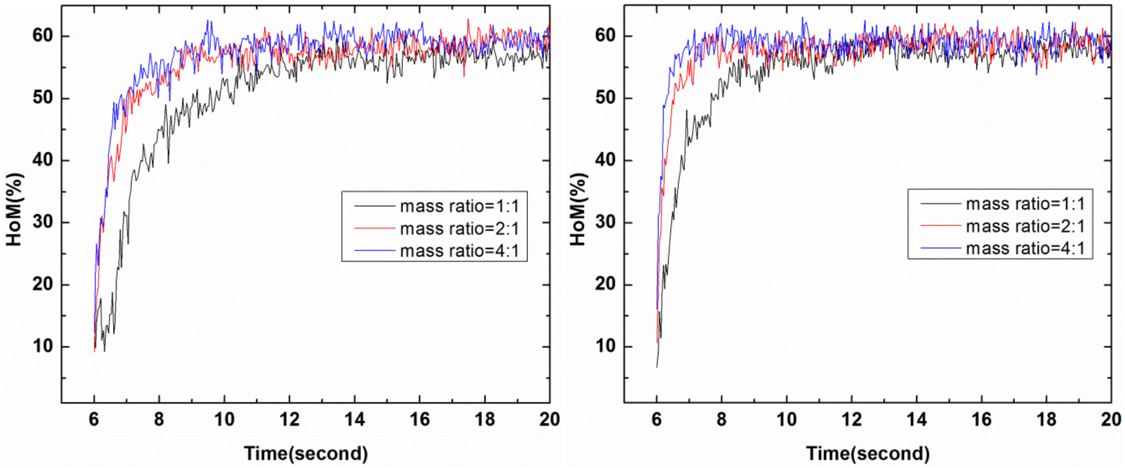

(a) magnets size=2000μm (b) magnets size=1169μm

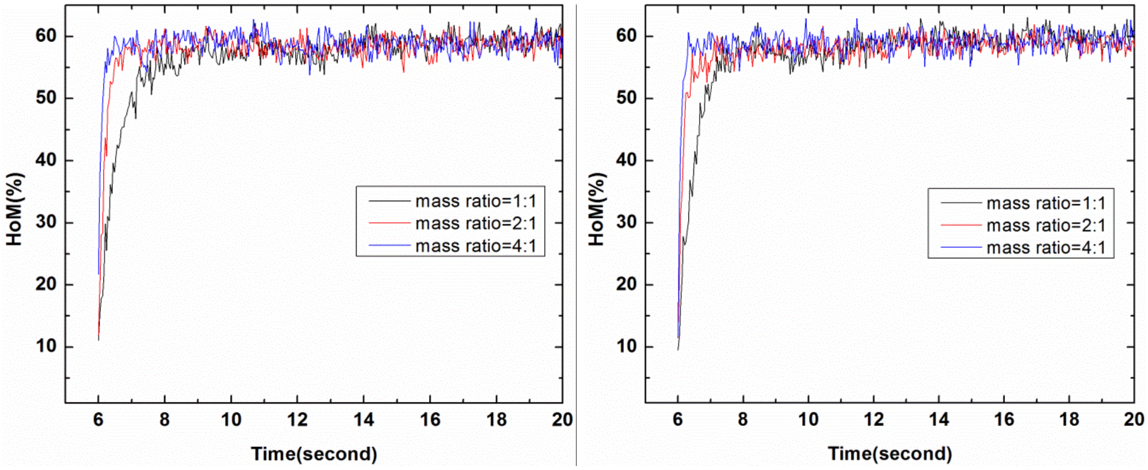

(c) magnets size=811μm (d) magnets size=644μm

**Figure 4.4** The effect of mass ratio on HoM under various magnets size.

### 4.3.4 The Collision Parameters and Homogeneity of Mixing

During MAIM, the energy is transferred from magnets to non-magnets by means of collisions between the two types of particles. The motion of non-magnets, driven by the momentum transfer by the magnets, will promote the mixing of non-magnets. In the DEM simulations, each collision is tracked and the velocity of the particles is recorded, which can be used to calculate collision number (total collisions for all the particles during a certain amount of time) and collision energy. The two types of collisions that influence the homogeneity of mixing are examined in this paper. The first is the number of collisions between magnets and non-magnets, CNmn, and the second is the number of collisions between non-magnets and non-magnets, CNnn. The total collision energy between magnets and non-magnets is defined as CEt. For total collision energy, only CEt is discussed here because when the collision energy between magnets and non-magnets is compared to the collision energy between non-magnets and non-magnets, that latter is trivial. Figures 4.5(a), (b), and (c) show the relationship between CEt, CNmn, and CNnn versus time for surface energy of 0.2J/m$^2$ of the non-magnetic particles. According to Figures 4.5(a), (b) and (c), it is found that CEt, CNmn and CNnn, all increase almost linearly with time. At the same time, they also increase with the increasing number of magnets under fixed surface energy. While not shown, similar trends were observed for the other two surface energy cases. For the convenience of comparison between different simulation cases, collision frequency (CFmn, CFnn) can be defined as the respective collision number (CNmn, CNnn) per unit time. Therefore, collision number CNmn and CNnn represent the product of collision frequency CFmn and CFnn and processing time, respectively. For individual collisions, CEmn represents the collision energy for each collision between magnets and non-magnets.

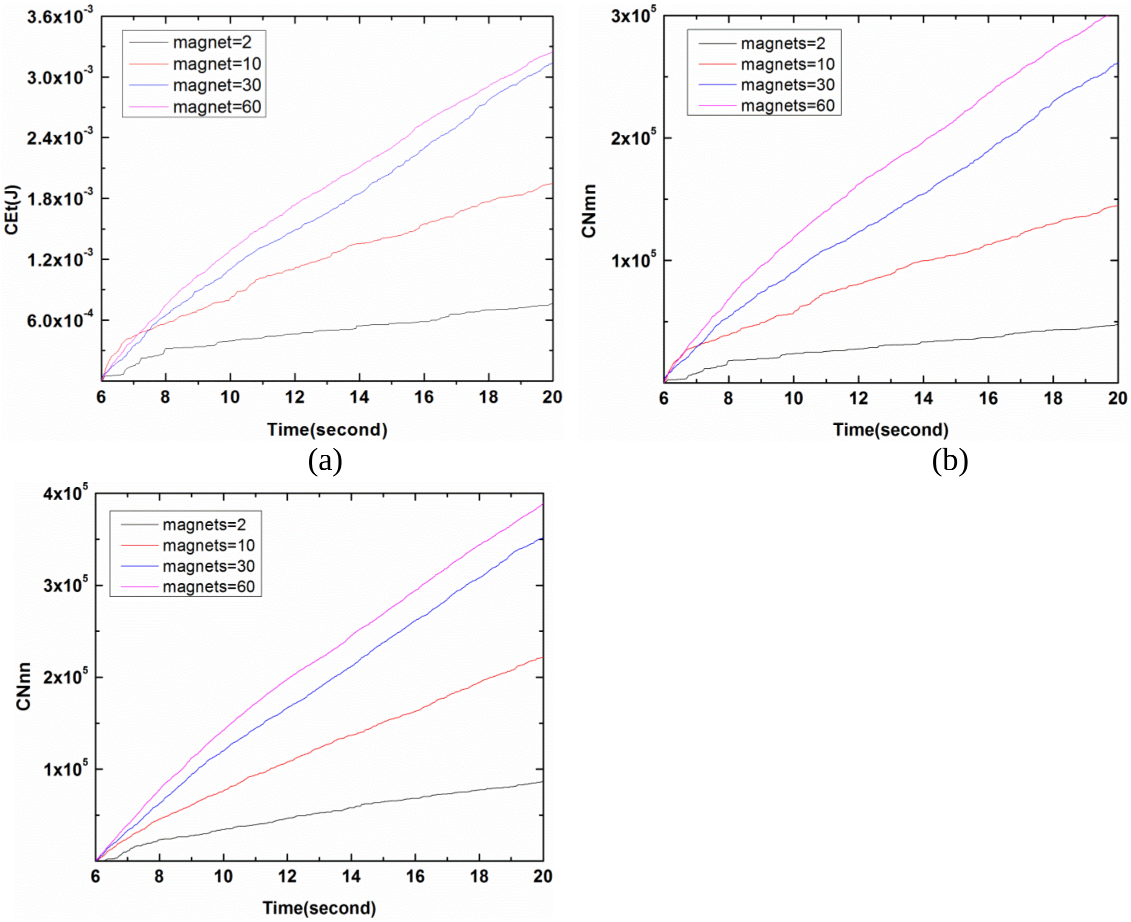

(a) (b)

(c)

**Figure 4.5** The relationship between collision numbers, collision energy and time.

Figure 4.6 shows the results of CFmn, CFnn, and the product of CEmn and CFmn, as a function of the number of magnets and different surface energies. According to Figure 4 6(a), the CFmn increases with increasing number of magnets for all three different surface energies. For a fixed number of magnets, the CFmn also increases with increasing surface energy. For example, when the magnet size is 2000µm, CFmn is about 1400 times per second for a surface energy of 0.1J/m$^2$ and 15000 times per second for a surface energy of 0.3J/m$^2$. When compared with the information in Figure 4.3, which shows that the speed of mixing is faster for lower surface energy, this trend of the CFmn appears to be inconsistent with the speed of (or time taken for) mixing for various surface energies. On the other hand, as seen in Figure 4.6(b), CFnn increases with increasing number of magnets, and at the same time, CFnn also increases with decreasing surface energy, which is consistent with the trend observed for the speed of mixing. When the collision energy between magnets and non-magnets is factored in, as shown in Figure 4.6(c), the trend is similar to Figure 4.6(a), hence at low magnet mass ratio, CFmn and its product with CEmn have inconsistent trend with the speed of mixing. It is noted that the collision energy decreases slightly when the size of magnets decreases from 811μm to 644μm, for the surface energy of 0.3J/m$^2$. This latter exception seems reasonable when we account for the results from Figure 4.2(c), showing that the speed of mixing decreases for 644μm magnets as compared to 811μm magnets, with a surface energy of 0.3J/m$^2$. From Figures 4.6(a) through (c), we can conclude that the collisions between the non-magnets and non-magnets, represented by CFnn in Figure 4.6(b), seem to follow a trend consistent with the mixing time results from the simulations as well as the experiments; however, the number of collisions between magnets and non-magnets and the respective collision energies (Figures 4.6(a) and 6(c)) do not follow the same trend.

While these results show that neither collision frequency (for collisions between magnets and non-magnets) nor collision energy can directly explain the trend of HoM versus surface energy, the results do reveal the significant role the surface energy has on the homogeneity of mixing. This conclusion could not have been derived without the generation of agglomerates, which were utilized to represent the effect of cohesion. The fact that CFnn is lower with increasing surface energy indicates that there is a stronger cohesive force between non-magnets making it difficult to deagglomerate those particles, and thereby they remain as agglomerates and hence reducing the number of collisions amongst them. Similarly, the increased number of collisions (and associated total collision energy) between magnets and non-magnets with increased surface energy also suggests that agglomerates are mostly in-tact and that the collisions are between the magnets and the non-magnets that are still part of the agglomerates, without the associated dissipation due to fragmentation. Thus overall, by just examining the collision numbers and collision energy, without examining the state of deagglomeration, the expected trend with respect to increased surface energy cannot be explained. Likewise, although the collision frequency and collision energy are both higher for a surface energy of $0.3 J/m^2$, the process of mixing is still slower when compared to the surface energy of $0.1 J/m^2$ and $0.2 J/m^2$. This may also be attributed to lack of deagglomeration for the higher surface energy, as will be examined through agglomerate fragmentation analysis in the next sub-section.

Figures 4.6(d), (e) and (f) show the relationship of CFmn, CFnn, and CFmn*CEmn and the size of the magnets, for different magnet-to-sample mass ratios at fixed surface energy, and these results are as expected. By increasing the mass ratio, thus increasing the number of magnets, higher collision frequencies and collision energies are achieved and should accelerate the mixing process.

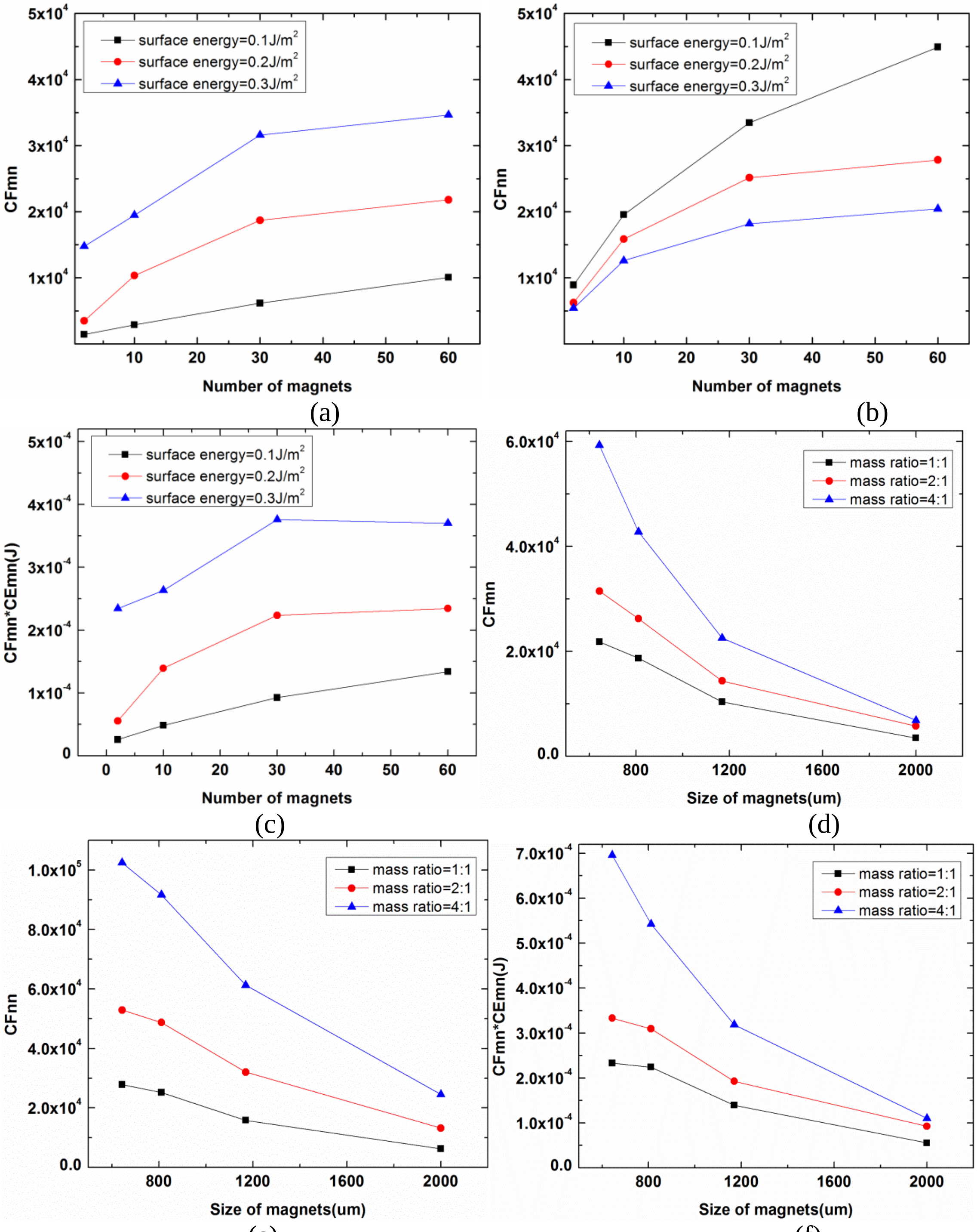

**Figure 4.6** Results about collision frequency and collision energy.

### 4.3.5 The Agglomerate Fragmentation Analysis

Based on the results shown in Figure 4.6, neither CFmn nor CFmn*CEmn can be used to explain the trend of HoM with respect to increasing surface energies, although the trend observed for CFnn is consistent with the HoM results. Thus there is a need for the examination of the fragmentation of the agglomerates caused by collisions between magnets and non-magnets. In this work, since the agglomerates are rather small and have small coordination numbers, it was more instructive to analyze the number of particles that detach from the agglomerate as a function of the surface energy and other processing conditions. This essentially represents the process of agglomerate fragmentation as a function of the processing conditions and time. Figure 4.7 shows the number of detached particles, defined as non-magnetic particles, which do not contact with any other non-magnetic particles, at a specific time. The number of detached particles is obtained at different times (every 20000 time steps after the magnetic force is introduced) and the averaged value is used for comparison with the different simulation cases. As seen in Figure 4.7(a), for a fixed number of magnets, the number of detached particles increases with decreasing surface energy. Furthermore, for a fixed surface energy, the number of detached particles increases with increasing number of magnets. When the surface energy is low, the number of detached particles continues to increase, as the number of magnets increase. When the particles have a high surface energy, the curves reach a plateau and level off. This is in line with the results from Figure 4.2(d), where the speed or time of mixing shows a similar trend, particularly at the highest surface energy. Thus results of Figure 4.7(a) demonstrate the relevance of the agglomerate fragmentation analysis done through counting of detached particles, hence deagglomeration, on the process of mixing of cohesive particles.

Next, the number of detached particles is analyzed as a function of increasing magnet mass ratio. As shown in Figure 4.7(b), the number of fragmented or detached particles increases with increasing magnet mass ratio. These results from Figure 4.7 are comparable to the trends of HoM in Figure 4.3 and Figure 4.4, revealing that the analysis of fragmentation and hence trends of detached particles better predict the nature of the mixing process as influenced by surface energy and magnet mass ratio. Thus, the mixing conditions that lead to a higher degree of deagglomeration/detachment will lead to improved mixing. As one may expect, higher surface energy tends to decrease the number of detached particles due to the stronger interparticle force as seen here, and thus the information on collision frequency between the non-magnets and magnets is not sufficient to define the mixing process of cohesive powders. Thus, deagglomeration is expected to be a function of collisions between magnets and non-magnets combined with the surface energy of the non-magnetic particles. Further insight into fragmentation and subsequent mixing may be obtained by analyzing the cohesive energy between non-magnets and non-magnets, calculated as follows [101]:

$$E_{coh} = 2N_c \pi a^2 \gamma \tag{4.30}$$

The averaged contact number, $N_c$, and contact radius, $a$, can be obtained by means of simulation results, thus the cohesive energy can be calculated using Equation 4.30, which represents the averaged energy required to detach one non-magnetic particle from an agglomerate.

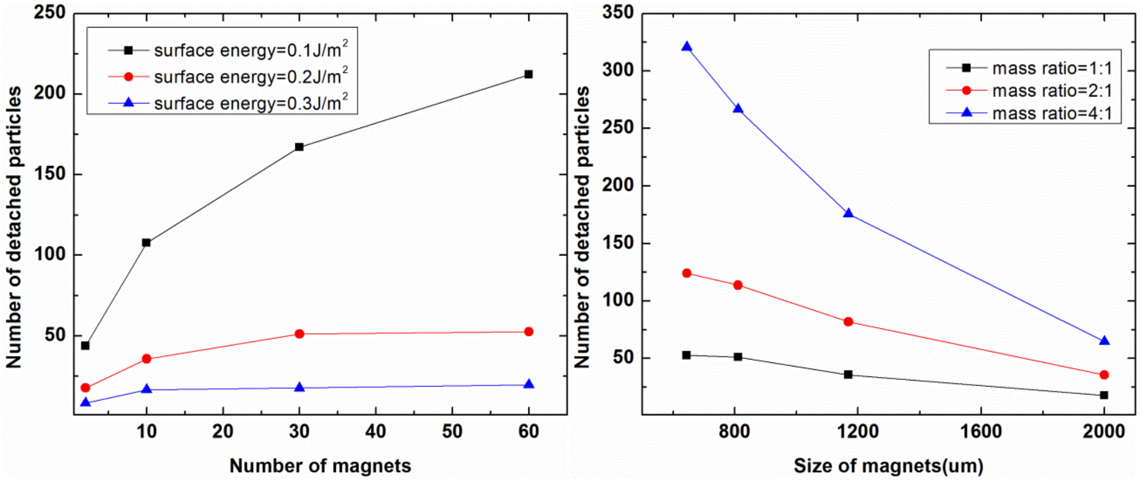

(a) (b)

**Figure 4.7** The evolution of number of detached particles under different surface energies and mass ratios.

During the MAIM process, non-magnets gain the energy from the frequent collisions with magnets, which are agitated by an external oscillating magnetic field. Additionally, we have also learned that the surface energy has significant effect on the deagglomeration and hence mixing process. In order to shed further light on the relationship between collision energy, surface energy, and the number of detached particles, simulations with larger surface energies were carried out. In Figure 4.8(a), the results are shown for the effect of surface energy on the HoM as a function of time for the 811μm magnets size and 1:1 mass ratio. It can be seen that the speed of mixing decreases gradually with increasing surface energy, and the time required to reach a perfect random mixing is delayed. When surface energy is larger than 0.5J/m$^2$, HoM has not yet achieved an asymptotic value at the end of the simulation. When the surface energy is set to even higher value of 1.2J/m$^2$, the results show that very poor mixing occurs. Figure 4.8(b) shows the cohesive energy calculated from Equation 4.30, the normal collision energy (CEnmn), and the tangential collision energy (CEtmn) as a function of surface energy. The normal and tangential energy were calculated using the relative normal and tangential velocities, respectively. As seen in Figure 4.8(b), the tangential collision energy is much larger than the normal collision energy due to the high rotational velocity of the magnets. Both normal collision energy and tangential collision energy are almost constant because of the fixed magnet size and the strength of the external magnetic field and do not depend strongly on surface energy. For the surface energy of 0.7J/m$^2$, the values of cohesive energy and collision energy are very similar. However, as the surface energy is increased to 1.0J/m$^2$ and 1.2J/m$^2$, the cohesive energy becomes larger than the collision energy. Figure 4.8(c) shows the corresponding number of detached particles as a function of surface energy, indicating that the number of detached particles decreases quickly with increasing surface energy.

Therefore, based on the results in Figure 4.8, the relative collision and cohesive energies provide useful indication of the possibility of mixing at sub-agglomerate level. Consequently, good mixing can occur only when the collision energy is higher than the cohesive energy. Otherwise, the mixing will be much slower or it may not occur at all due to lack of deagglomeration.

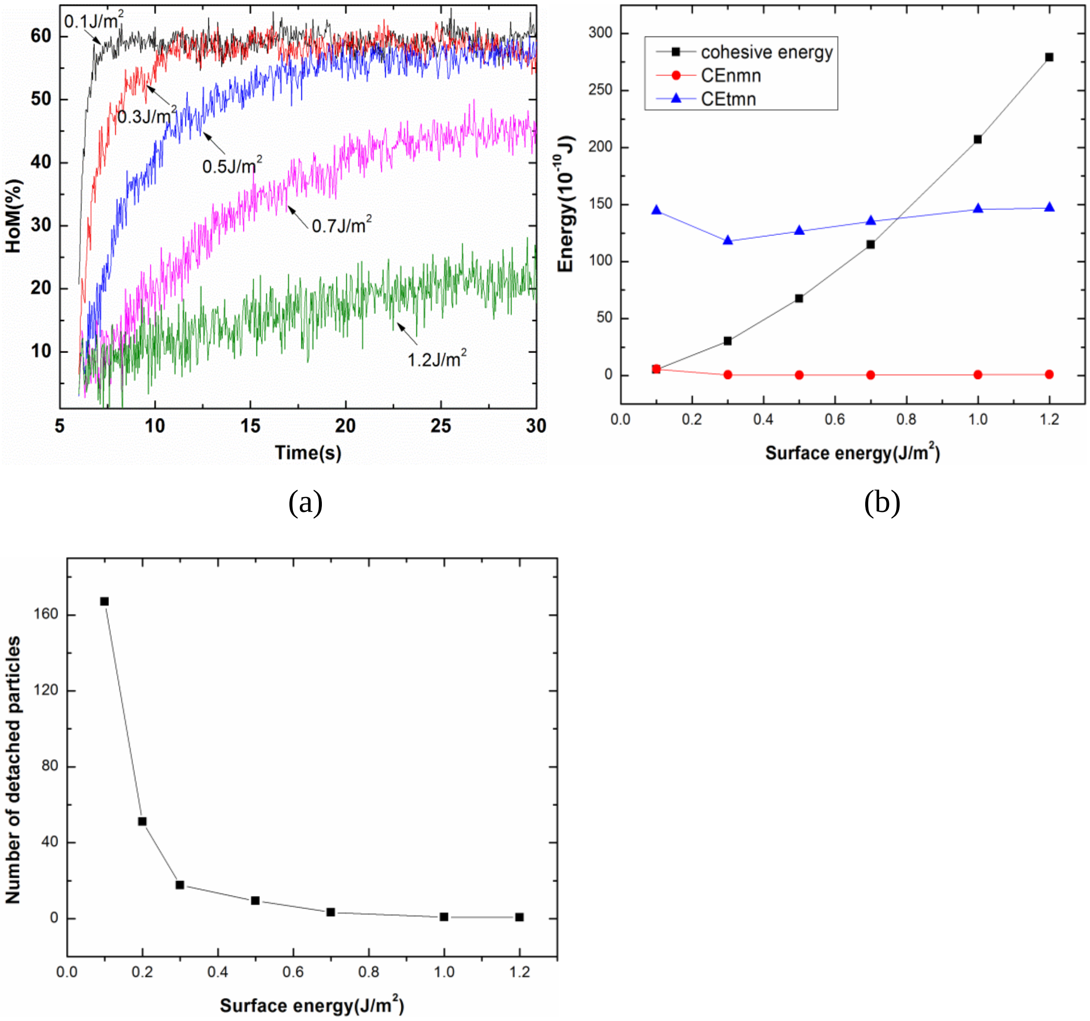

(a) (b)

(c)

**Figure 4.8** (a) Relationship between HoM and surface energy, (b) the relationship between cohesive energy, normal collision energy (CEnmn) and tangential collision energy (CEtmn), (c) the relationship between the number of detached particles and surface energy.

## 4.4 Conclusions

A DEM based particle system model that incorporates agglomerates of cohesive particles in mixing was developed to determine the effect of interparticle forces on the magnetically assisted impaction mixing process. The simulation results show that the mixing will be faster for an increase in the number of magnets and magnet-to-sample mass ratio, agreeing well with the previous experimental results. Trends observed in the homogeneity of mixing (HoM) as a function of surface energy, mixing conditions and processing time in simulations are qualitatively consistent with previously observed experimental results. The results suggest that the system model used for the analysis of mixing based on the evaluation of deagglomeration of the agglomerates is a reasonable representation of the mixing behavior of very cohesive particles as in MAIM.

The relationship between HoM and the collision parameters, CFmn, CFnn, CEt, are analyzed to obtain better insight into the mixing of cohesive particles. The analysis shows that, for a fixed surface energy, the mixture will reach a more homogeneous state faster with higher collision frequency and collision energy between magnets and non-magnets, whereas collisions between non-magnets and non-magnets do not reveal useful information without analyzing the fragmentation process. Results also show that with increasing surface energy, the mixing process requires longer time to reach a more homogeneous state with all else being equal. Analysis of the deagglomeration was carried out by examining the number of detached particles as a function of other conditions, and revealed the real impact of surface energy, hence cohesive forces between non-magnetic particles. Such analysis also showed that when the collision energy is significantly higher than the cohesive energy, mixing of primary particles occurs more readily, and sheds light on the relative roles played by surface energy, magnet mass ratios and magnet size. In cases when the cohesive energy is larger than the collision energy, the mixing may not occur on a sub-agglomerate scale because it will be very difficult for magnets to detach non-magnets from the agglomerates. Clearly, mixing can occur at the larger scale of scrutiny even when the surface energy is high and the cohesive energy is higher than the collision energy, but the mixture homogeneity would be low if examined at a finer scale of scrutiny. Employing the agglomerates in the modeling of the mixing of cohesive particles allowed for revealing such nuances of the mixing process, which otherwise would not have been observed.

It is hoped that the cohesive particle system modeling approach presented and the results obtained here are not only pertinent for mixing, but can also be used to understand particle (or sub-agglomerate) scale mechanisms in other processes involving nano or micro sized highly cohesive particles, such as in dry coating and processing of nanocomposite materials.

# CHAPTER 5

# PARTICLE DYNAMICS INSIDE THE CONICAL SCREEN MILL (COMIL)

## 5.1 Introduction

The conical screen mill, comil, is a popular continuously operating device in pharmaceutical industry for its use in granule milling or cohesive powder delumping. Despite its ubiquitous presence in the industrial applications, it has not been well studied until recently [143, 144] where it has been shown to be a highly promising device for dry coating. This is because unlike conventionally available dry coating devices [91] that operate in a batch mode and pose challenges for scale up, comil can operate continuously, hence is potentially easier to scale up, and could be easily incorporated into continuous pharmaceutical tableting operations. Recent interesting work has shown that its use for dry coating of poorly flowing pharmaceutical powders such as fine grades of acetaminophen, ibuprofen and ascorbic acid leads to significant improvement in their flow and packing density [145]. Significant improvements in these two properties could help eliminate more extensive granulation based operations, and may subsequently aid high speed continuous manufacturing [146], and warrants further investigation.

In this chapter, a DEM model of comil is developed and the residence time is studied by means of simulating a process comparable with the experiments through pulse tracer input method. The effect of impeller speed, feed rate, open area and the size of holes in the comil screen on RTD and MRT is examined. As will be shown, the simulation results indicate that MRT increases with increasing impeller speeds, an outcome that appears to be counter-intuitive. A limited experimental investigation is conducted to corroborate those results, indicating that the effect of impeller speeds on RTD and MRT are qualitatively consistent with the simulation results. In addition to computing the RTD and MRT, the relationship between average collision number (ACN), number of particles inside the transition zone (region above the cone), and MRT is examined, suggesting that the MRT alone cannot explain the expected coating quality. The detailed analysis of the nature and spatial distribution of collisions is done so that better understanding of the impact of the operating parameters may be gained. As will be shown, such detailed analysis provides better explanations of the coating quality improvements seen as a function of impeller speed at low powder feed rates shown in the prequel [145].

The governing equations for individual particles can be written as follows:

$$m_i \frac{d\vec{v}_i}{dt} = \sum_{j \neq i}^{k} \vec{F}_{ij} + m_i \vec{g} \tag{5.1}$$

$$I_i \frac{d\vec{\omega}_i}{dt} = \sum_{j \neq i}^{k} \vec{T}_{ij} \tag{5.2}$$

$$\vec{F}_{ij} = \vec{F}_{ij}^{n} + \vec{F}_{ij}^{t} \tag{5.3}$$

$$\vec{T}_{ij} = \vec{R}_i \times \vec{F}_{ij}^{t} - \vec{\tau}_{ij}^{r} \tag{5.4}$$

where $m_i$, $\vec{v}_i$, $\vec{\omega}_i$, $\vec{R}_i$, $I_i$ represent the mass, translational velocity, rotational velocity, vector connecting the center of particle *i* and the contact point, and the moment of inertia of particle $i$. $\vec{F}_{ij}$ is the contact force induced by particle $j$ and it can be divided into two parts: normal contact force $\vec{F}_{ij}^{n}$ and tangential contact force $\vec{F}_{ij}^{t}$. $\vec{T}_{ij}$ represents the torque induced by particle $j$ due to tangential contact force and rolling friction force. The total contact force and torque is the summation over $k$ particles in contact with particle $i$.

## 5.2 Model and Initial Parameters

### 5.2.1 Geometry and Initial Parameters

An underdriven (model U3, Quadro Engineering, Waterloo, Ontario, Canada) comil was used in simulation and the schematics are shown in Figures 5.1(a) and (b). There are five different sections in the model, including a feed chute, a transition zone, screen, impeller, and the base of the impeller. Two identical impellers that are diametrically opposed are fixed onto the base of the impeller that rotates at speed of the base attached to the motor (not important in the DEM model). The gap between impellers and screen is four times the particle diameter. This is similar to what is in the physical device and the gap is large enough to reduce the damage to the screen and avoid contamination from metal abrasion. In the experiment, the rotating impeller exerts significant collision force on the particles causing deagglomeration, delumping or breakage of the fine powders. The actual dimensions of each zone of the comil were measured prior to establishing the DEM model. Since the particles used in experiments are normally too small to be simulated directly because of very small time steps and large number of particles that would be required, all of the dimensions of the device have been scaled up by 10 times. It is noted that the particle size is also scaled up by the same ratio so that the particle size relative to the comil dimension is comparable with the actual physical experiments.

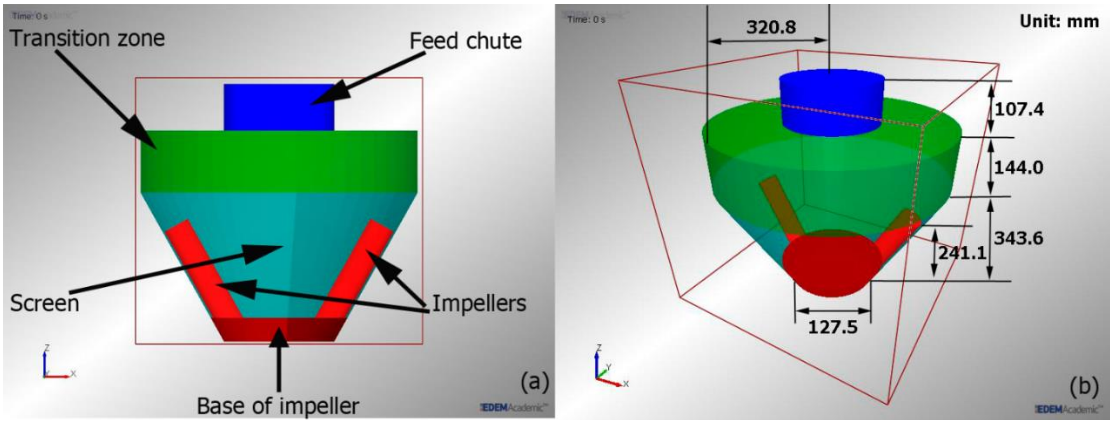

**Figure 5.1** The schematic of the comil model. (a) view along y axis, (b) perspective view.

Exact modeling of the comil device used for dry coating process involves a large number of parameters. Some of the critical and independent operating parameters are: the powder feed rate, the impeller speed, size of the screen holes, total open area, the impeller shape, the gap between the impeller and screen, and, thickness and other geometrical features of the screen. In addition, there are material related parameters, such as the particle size and their other properties. There are also several parameters that may not be independent, for example, the material hold up or the fill level of the comil; which unlike in a batch process like ball mill, cannot be independently set or controlled and would be, for example, a function of the feed rate and the mean residence time (MRT). The latter depends on several other conditions and is part of the outcome or response of the experiment. In order to limit the scope of this investigation, only those parameters that seem relevant based on previous experimental studies are considered. To be specific, the prequel examined the powder feed rate, the impeller speed, and the size of the screen holes, and showed that those have an impact on dry coating quality[145] . Therefore, these parameters which are expected to have primary impact on the comil performance are examined, whereas parameters, for example, the thickness of the screen are not considered because they would have secondary impact and have also not been a subject of experimental investigations for dry coating [143-146]

The simulation starts with randomly generated particles, which do not overlap initially, appearing in the feed chute. The particles will then fall down into the screen region, under gravitational force, and impact with rotating impellers and the other vessel boundaries. When the particles collide with the screen, they have the chance to flow out through the holes in the screen or the particles can rebound from the screen and continue to collide with the other boundaries and particles inside the comil. The movement of particles continues until the particles flow out through the screen. The particles are generated dynamically according to the specific feed rate in the simulation, and individual particles may eventually leave the simulation domain upon exiting the screen.

Although the screen thickness is not considered explicitly in our simulations, as per [147], it may be a factor influencing the comil performance; however, they did not investigate it in their paper. The thickness of the screen could play a role because thicker screens have an effect of essentially reducing the total open area available for the particles to pass through. However, in order to keep the computation burden limited in the present work, the screen holes are considered to be two-dimensional and incorporated within the contact model in which the relative position between particles and screen holes is examined in each simulation step to determine whether or not the particles pass through the holes. While this is not as authentic as using computer-aided-design software to make fully three-dimensional holes in the screen, it is expected that the results capture the primary impact of the dimensions of the holes, while the effect of the screen thickness may be partially captured by simulating smaller hole sizes. The DEM modeling also does not consider particle breakage. That is because the present investigation is limited to the use of comil in dry coating where the experiments indicated little or no particle breakage, which is unlike in milling, where there is particle breakage.

In terms of the key parameters related to particle and the vessel properties, typical properties of pharmaceutical powders and steel are used and kept at fixed values. While some parametric variation of these properties may provide information on their impact on the collision dynamics, the emphasis of this paper is on examining the major trends in the outcomes as a function of operating parameters such as the impeller speed, feed rate, etc. Accordingly, the sizes of the particles are set to 1.0 millimeter, Poisson's ratio is 0.3, shear modulus is 10MPa and the particle density is 1500kg/m$^3$. For the vessel geometries/boundaries, the Poisson's ratio is 0.3, shear modulus is 77GPa, and the density is 7900kg/m$^3$, which represent the properties of steel [148]. The coefficient of static friction is 0.3 and the coefficient of rolling friction is 0.01, chosen based on prevalent practice [149].

### 5.2.2 Residence Time Theory

Residence time distribution (RTD) has been widely investigated by experimental methods [135, 150-154]. In experiments, the pulse tracer input method is commonly used to determine the RTD. For this method, a tracer pulse is injected at the inlet of the flow stream, and then the concentration of tracer particles is measured at the outlet of the flow stream at different time intervals. Supposing c(t) is the concentration of tracer at the outlet of flow stream as a function of time. RTD is then defined as:

$$E(t) = \frac{c(t)}{\int_0^\infty c(t)dt} \approx \frac{c(t_i)}{\sum_0^\infty c(t_i)\Delta t_i} \qquad (5.5)$$

The quantity, E(t), is the residence time distribution function, and it describes qualitatively how the time spent inside the system will differ for different flow elements [155].

It is common to compare the RTD by using its moments. Roughly speaking, the first moment of RTD describes its size and the higher moment describes its shape [156]. The first moment of E(t) is called mean residence time (MRT), which represents the average time the particles remain in the comil.

$$MRT = \int_0^\infty tE(t)dt = \frac{\sum_0^\infty tc(t_i)\Delta t_i}{\sum_0^\infty c(t_i)\Delta t_i} \qquad (5.6)$$

The second moment is the variance, indicating the degree of dispersion around the mean residence time. The greater value of this moment represents the larger spread of distribution.

$$Var^2 = \int_0^\infty (t - MRT)^2 E(t)dt \qquad (5.7)$$

In the simulation, the basic procedures are set to mimic the experiments. First the particles are generated continuously at a specific feed rate and then the tracer particles are added into the main flow stream at a designated time. The concentration of tracer particles in the outlet flow stream can be monitored at different time intervals so that the c(t) curve can be calculated. Finally, according to Equations 5.5, 5.6 and 5.7, the MRT and variance can be obtained.

One of the assumptions required to measure RTD, using the tracer method, is that the main flow stream is at a steady state [157]. Therefore, the decision of when to add the tracer particles is one of important simulation problems. In order to choose a suitable time to introduce the tracer particles, the total number of particles inside the screen is calculated as a function of time. If a steady flow stream has been formed in the comil, then the number of particles inside the screen should be almost constant. This means that the number of particles entering into the screen section is equal to that of the particles leaving the screen. Figures 5.2(a) shows the result for how the amount of particles inside the comil, which includes the transition section plus the screen section, changes with time (not including the tracer particles). As seen in Figures 5.2(a), the number of particles inside the screen first increases and then a steady state value is achieved. In this simulation, the steady state value occurred at about ten seconds after the beginning of simulation. Therefore, the tracer particles are introduced at the tenth second in all the simulations. Moving forward in this paper, if not stated otherwise, the “zero time” refers to the tenth second of the simulation, corresponding to when the tracer is introduced. The particles inside the comil are also visualized in Figure 5.2(b). It should be noted that the particles can be barely seen if only one simulation step data are visualized because the particle size is very small compared with the dimensions of comil. Therefore, all the particle trajectories from 20.05 to 20.07 seconds and amplitudes of particle velocity are displayed in Figure 5.2(c) for the same simulation conditions with Figure 5.2(a). The different colors are used to characterize the amplitudes of particle velocity. It can be seen that there are more particles with lower velocities in the transition zone and lesser amount of particles with higher velocities in the screen section. Such particle scale information will be later discussed in detail.

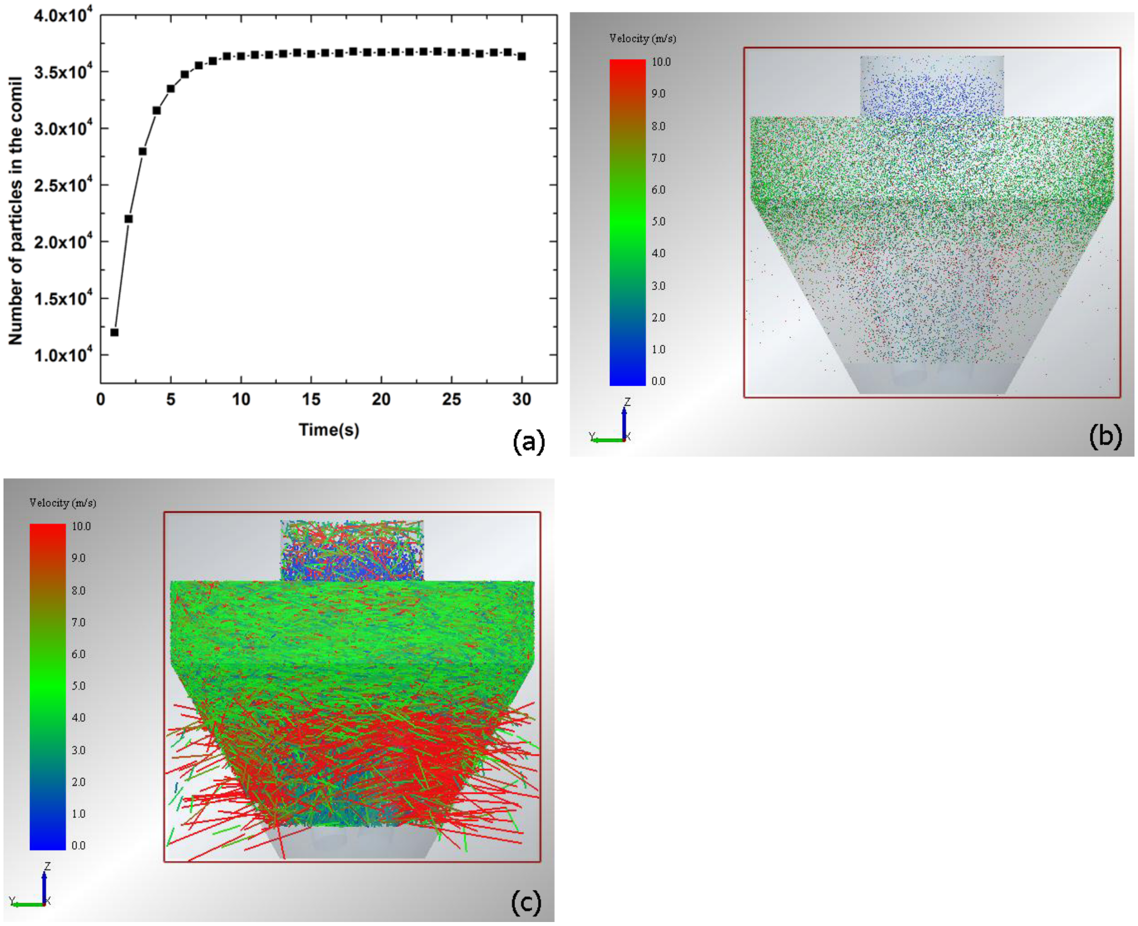

**Figure 5.2** (a) The relationship between the number of particles inside the with time. (b) Particle distribution inside the comil, (c) Particle trajectories inside the comil, different colors represents different amplitudes of particle velocity.

## 5.3 Results and Discussions

### 5.3.1 The Effect of Impeller Speed and Feed Rate on RTD and MRT

Figure 5.3 demonstrates the effect of impeller speed on RTD under different feed rates. According to this figure, the magnitude of E(t) is generally smaller for the higher impeller speed during the first several seconds for all the three different feed rates. After about four seconds, however, E(t) increases with increasing impeller speed for all feed rates. It is important to note that the range of the MRT values is not very large, suggesting that MRT may not necessarily dictate the outcome of the final process, e.g., quality of dry coating [146]. Nonetheless, this observation indicates that at higher impeller speeds, fewer particles flow out through the screen within first several seconds, and the particles have longer residence time.

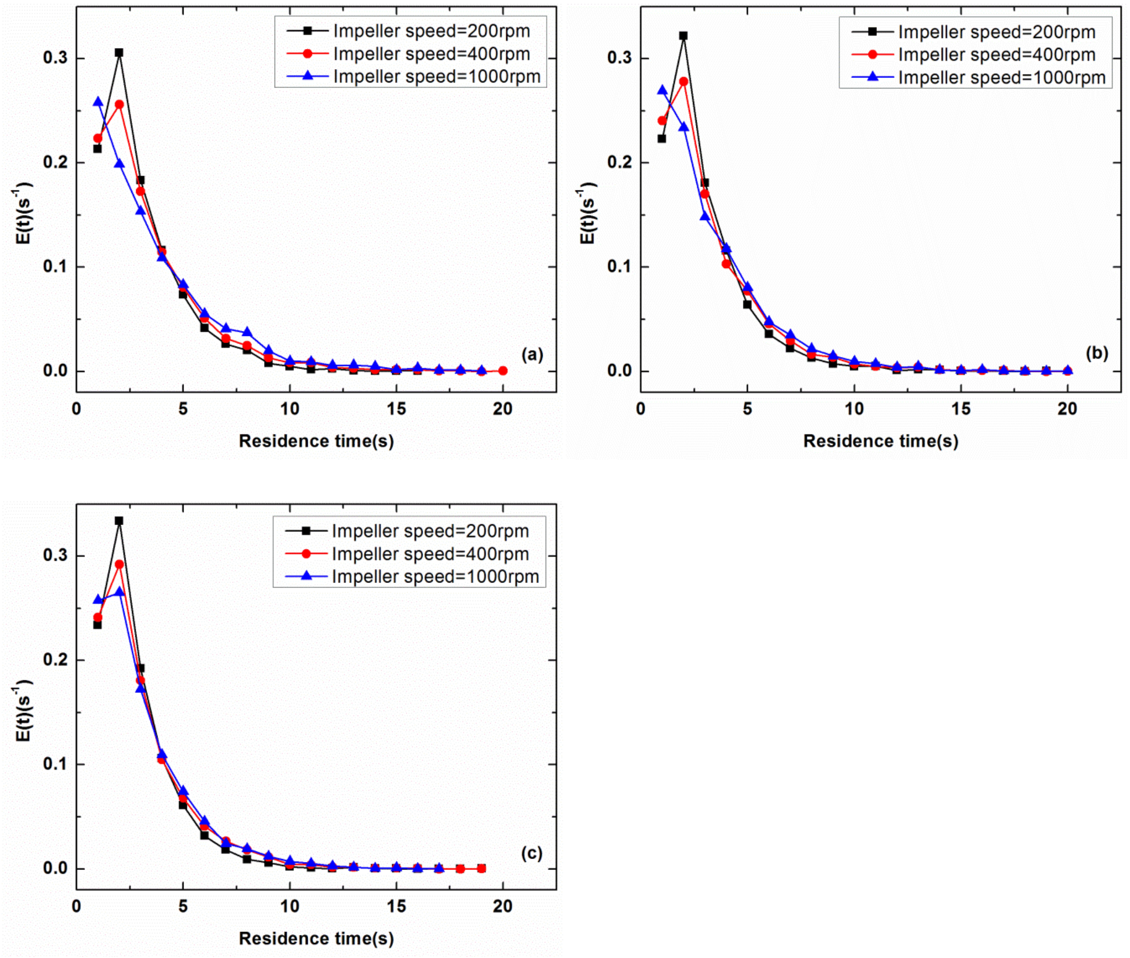

**Figure 5.3** The effect of impeller speed on the E(t), Impeller speed of 200rpm, 400rpm, and 1000rpm, respectively. (a), (b), (c) correspond to the feed rate of 5000, 10000, and 20000 particles per second, respectively.

The results for the effect of feed rates on the RTD for different impeller speeds. For all the impeller speeds, the trend is similar: E(t) increases within the first several seconds, and then decreases as time goes on, thus the RTD becomes narrower with increasing feed rate, indicating that as the feed rate increases, the particles have shorter residence time. Although this result may appear somewhat counter-intuitive, it is likely that higher feed rate leads to increasing collisions between particles, which could result in pushing the particles flow out faster through the holes in the screen.

Based on the residence time distribution, the MRT is calculated according to Equation 5.6. Figure 5.4 shows the results for MRT. It can be seen that the MRT increases with increasing impeller speed at any given feed rate. The MRT also increases with decreasing feed rate at any given impeller speed. Furthermore, the difference between the MRT at different feed rates increases with increasing impeller speed. For example, for impeller speed of 200rpm, the MRT increases about 9% when feed rate is decreased from 20000 to 5000 particles per second. In contrast, the MRT increases about 16% when impeller speed equals 1000rpm for the same change in feed rate. On the other hand, the difference in MRT, for different impeller speeds, decreases with increasing feed rate. For example, when the feed rate is 5000 particles per second, MRT increases about 17% when the impeller speed increases from 200rpm to 1000rpm. However, the MRT only increases about 10% when the feed rate is increased further to 20000 particles per second for same change in impeller speed. Thus the results indicate that the effect of impeller speed can be more dominant for lower feed rates. This result is consistent with the dry coating performance reported in [145], where at the lowest feed rate, the bulk density and FFC both showed a significant increase when increasing the impeller speed. Similarly, the effect of feed rate can be more dominant on the process for higher impeller speed. This is also in part consistent with the results reported in [145], where at the high impeller speed, the bulk density and FFC both showed a significant increase as the feed rate increased from low to medium, although the highest feed rate did not exhibit significant improvements. This suggests that while the MRT is a useful indicator of the process dynamics, it alone may not fully explain the dry coating performance. Similar to the MRT, the change in its variance for different impeller speeds and feed rates is observed. The variance increases with increasing impeller speed for a fixed feed rate; however, it decreases with increasing feed rate for a fixed impeller speed.

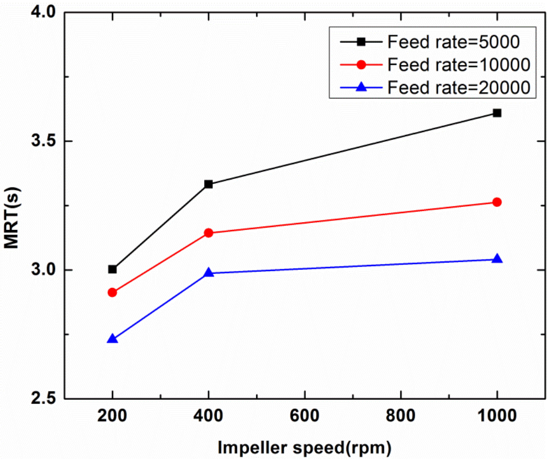

**Figure 5.4** MRT corresponding to the different feed rates and impeller speeds. Open area is 0.3, size of hole is four times the diameter of the particle size.

### 5.3.2 The Effect of Open Area on RTD and MRT

For the comil device, there are various screens available with different open areas, and may be used to manipulate its operation. It is generally believed that smaller amount of open area, which is similar to blocking some of the hole, may increase the powder hold up time, and may impact the process outcome. Although these conditions have not been investigated in previous experimental investigations [143-146], here the simulations are conducted to examine the effect of open area on the MRT. The diameter of each hole is four times the diameter of the particle size. Figure 5.5 shows the results for MRT, calculated from the data of RTD. It can be seen that MRT increases with decreasing open area at the impeller speeds of 200rpm and 400rpm. More specifically, at the impeller speed of 200rpm, as the open area is increased from 0.30 to 0.45, the MRT decreases about 24%, 25% and 22%, corresponding to flow rates of 5000, 10000, and 20000 particles per second. When at impeller speed of 400rpm, as the open area is increased from 0.30 to 0.45, the MRT decreases about 26%, 26%, and 25%, corresponding to flow rates of 5000, 10000, and 20000 particles per second.

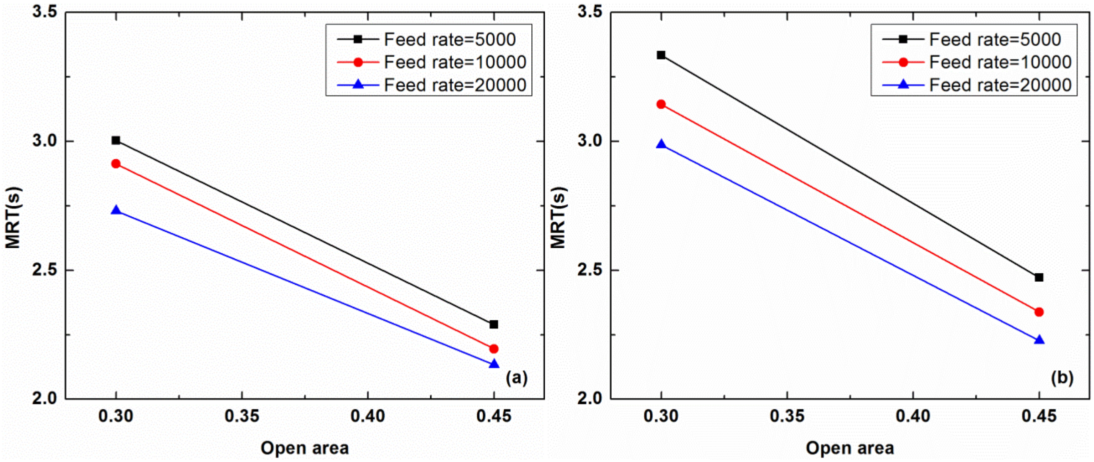

**Figure 5.5** MRT corresponding to open area of 0.3 and 0.45. Feed rate is 5000, 10000, and 20000 particles per second. Impeller speed is also changed. (a) MRT corresponding to 200rpm, (b) MRT corresponding to 400rpm.

### 5.3.3 The Effect of the Size of Holes on the RTD and MRT

Figure 5.6 shows the MRT for varying screen hole sizes and feed rates. For all feed rates, the MRT decreases quite rapidly with increasing screen hole sizes. This outcome is consistent with the results reported in [145], where the coating quality using a larger screen size was inferior to the smaller one. These results show that the screen hole sizes affect the MRT of particles even though the open area remains unchanged.

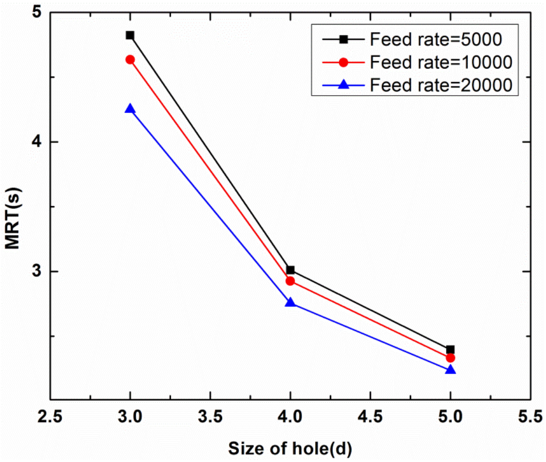

**Figure 5.6** Mean residence time corresponding to the different screen hole sizes. Impeller speed is 200rpm and open area is 0.3.

The simulations described till now, examining the impact of four key operating parameters on the MRT and RTD, have proven useful since they provide partial explanation of the experimental trends observed in [145]. However, one could also obtain detailed information from collisions that cannot be easily obtained from experiments and hence may provide further insight in to the dry coating performance. In the following section, such detailed analysis is carried out.

## 5.4 Collision Rate and Particle Number Analysis in the Comil

### 5.4.1 Collision Rate in the Comil

In the comil, after the particles fall down from the feed chute into the screen, they collide with vessel geometries and other particles. Due to the collisions, the direction and magnitude of the particles' velocity changes accordingly. After experiencing varying residence times, the particles flow out from the screen holes. Therefore, the collisions play a major role on the MRT. Moreover, in dry coating, the collisions between host and guest as well host and host particles promote attachment and dispersion of fine guest particles on the surface of host particles. Therefore, collision dynamics within the comil is investigated in details as it is required for analyzing both MRT and coating quality. The collisions have been divided into five different categories, including collision between particles and particles, particles and the screen, particles and the impellers, particles and transition zone, and the particles and the base of the impellers. Collision rate, defined as the total number of collisions for all the particles in a period of one second, is calculated and plotted as a function of time for all five zones in Figures 5.7 and 5.8.

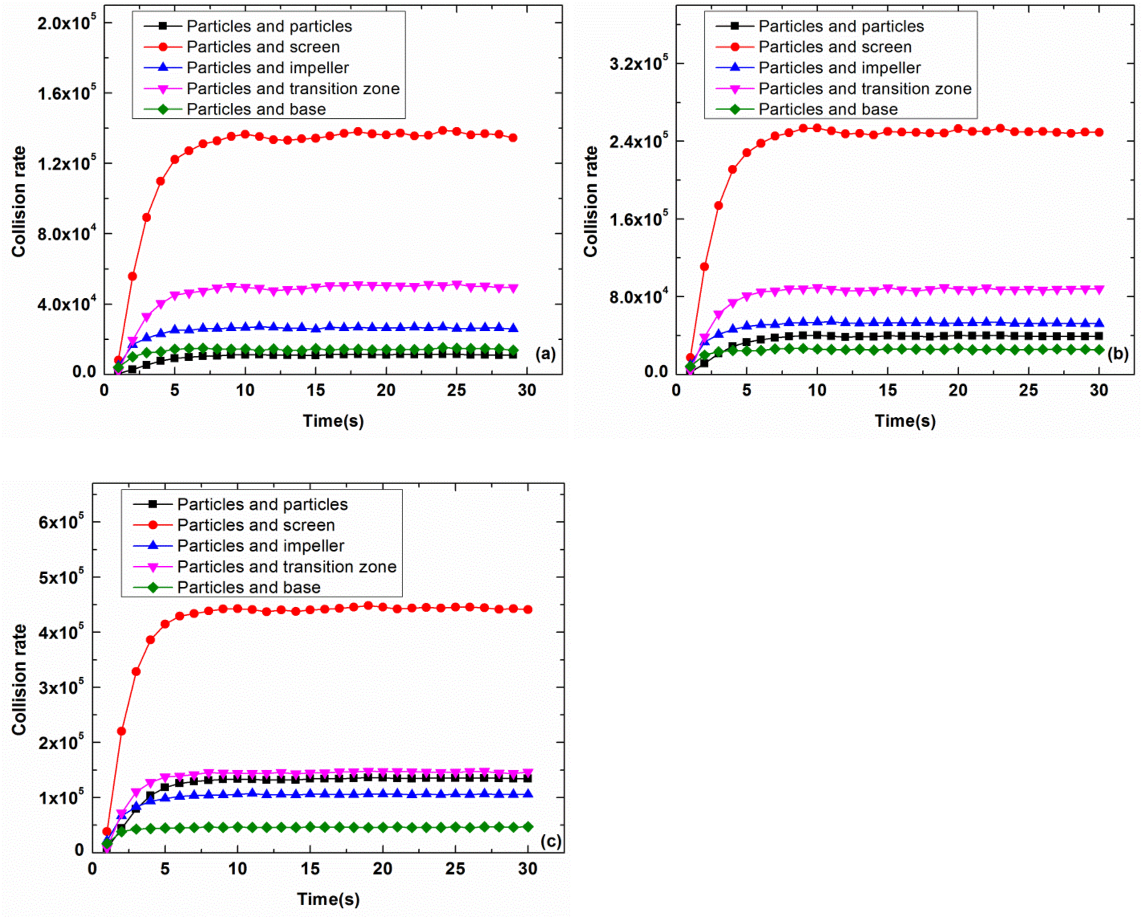

**Figure 5.7** The collision rate as a function of time. (a), (b), (c) correspond to the feed rate of 5000, 10000, 20000 particles per second, respectively. Impeller speed 200rpm.

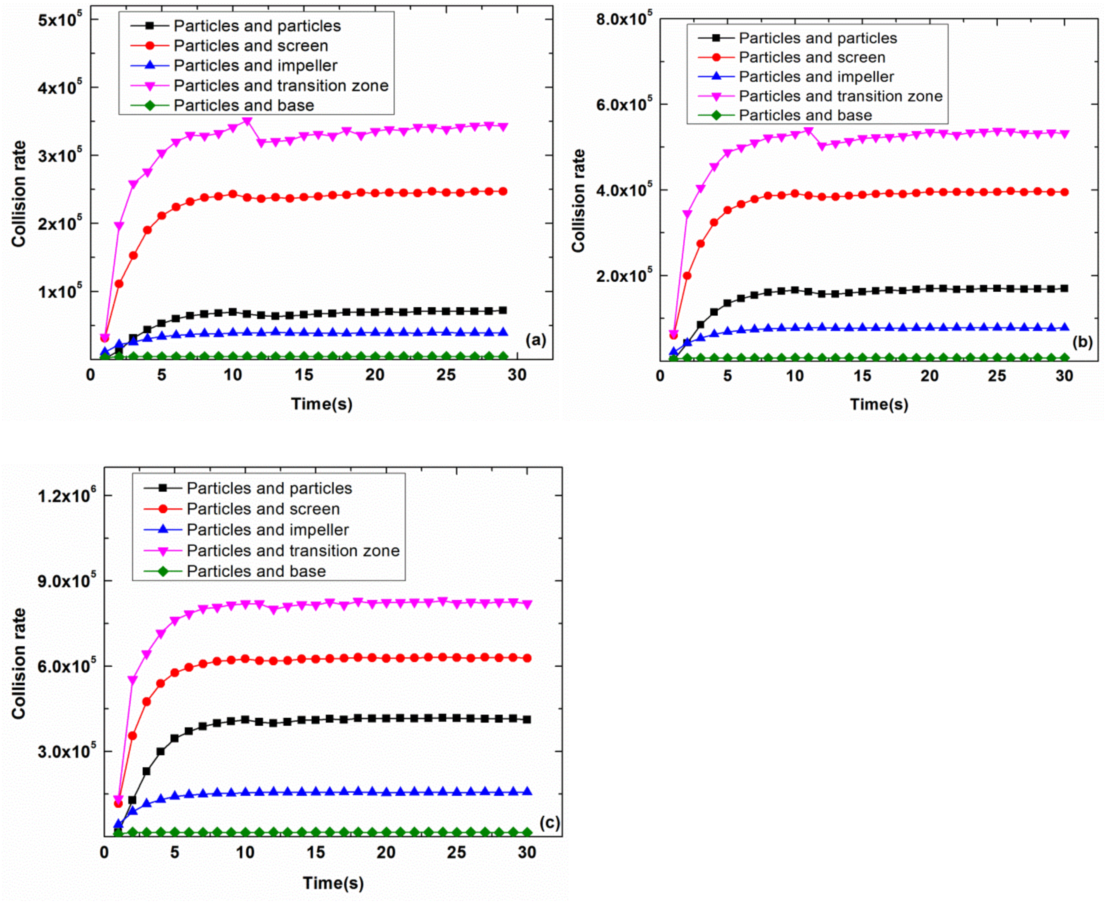

**Figure 5.8** The collision rate as a function of time. (a), (b), (c) correspond to the feed rate of 5000, 10000, 20000 particles per second, respectively. Impeller speed 1000rpm.

It should be noted that the times shown in Figures 5.7 and 5.8 are the real simulation times so that the entire evolution of collision rate with the time can be observed. Figure 5.7 shows the results for the collision rate corresponding to different feed rates, for a 200rpm impeller speed and open area of 0.3. In Figures 5.7(a)-(c), the feed rate is 5000, 10000, and 20000 particles per second, respectively, and all the other simulation conditions are the same. As shown in Figure 5.7, all of the different types of collisions achieve a steady value after about ten seconds. As mentioned previously, the number of particles inside the screen achieves a steady value at that time as well. Therefore, the results for collision rate also support that the addition of tracer particles at the tenth second is during steady state. Second, with an increasing feed rate, all of the types of collision rate increase. This is because there are more particles involved in the simulation with increasing feed rate, and therefore, the collisions between particles and particles, and particles and geometries increase. Third, the most dominant collision type is the collisions between the particles and the screen for all the feed rates. The collisions between particles and the walls in the transition zone yield the second highest collision number. Fourth, the relative magnitude of collision rate between particles and the impellers and between the particles and particles changes with various feed rates. When feed rate is low, the collision rate between particles and the impeller is larger than that between particles and particles. But with increasing feed rates, the collision rate between particles and particles increases faster than that between particles and the impellers.

The results of impeller speed of 400rpm have also been analyzed. The results are similar to those at 200rpm, shown in Figure 5.7. The collision between the particles and the screen is still dominant. The collisions between particles and particles increase faster, so that with and increasing feed rate the collision rate becomes larger than that between particles and impellers. In addition, compared to Figure 5.7, the collision rate between particles and transition zone is closer to that between particles and screen, which indicates that the collision rate between particles and transition zone increases faster than that of particles and screen with increasing impeller speed.

In Figure 5.8, the impeller speed is 1000rpm. Compared to the results from Figures 5.7, even at the low feed rate, the collision rate between particles and particles is still larger than that between particles and the impeller. Moreover, the most obvious difference is that the collision rate between particles and the transition zone becomes dominant over that between the particles and the screen. Transition zone is an important section in comil device since the particles cannot flow out from this section, thus can stay there longer. The number of particles in the transition zone is calculated and plotted in Figure 5.9. The results show the particle number in the transition zone increases with increasing impeller speed, which explains why the dominant type of collisions changed to collision between particles and transition zone with increasing impeller speed.

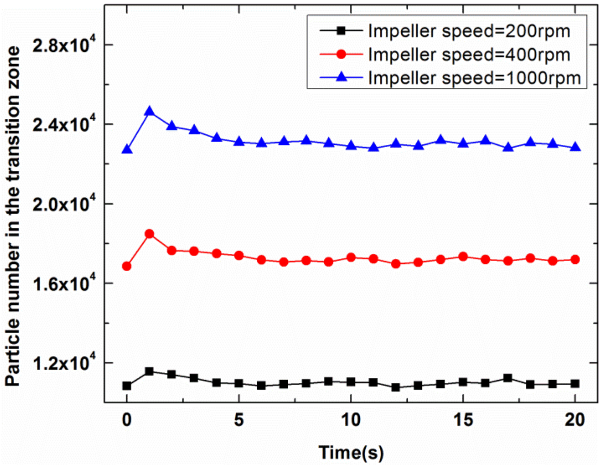

**Figure 5.9** The number of particles in the transition zone as a function of time for different impeller speeds. Feed rate of 20000 particles per second, size of the holes is four times the diameter of the particle, and open areas of 0.3.

### 5.4.2 Average Collision Numbers and Particle Number in the Comil

In order to conveniently compare the collision results for the different simulation conditions, the average collision number (ACN) is calculated by summing up all the specific types of collision numbers and dividing the sum by the total number of particles. The ACN represents how many collisions that one particle experiences before it flows out from the screen, where only the collisions occurring after ten seconds, i.e., once a steady value is achieved, are counted. The results for the ACN, corresponding to the different simulation conditions, are presented in Tables 5.1 to 5.7. The ACN between particles and the base of impeller, which is usually small compared to the other types of collisions, are not shown in these tables for the sake of brevity.

**Table 5.1** The Relationship between ACNs, P1, P2, and MRT for Different Feed Rates, and the Impeller Speed, Open Area, and Hole Size Are Fixed at 200rpm, 0.3 and 4d, Respectively.

| Collision types / Feed rate | Particles and particles | Particles and screen | Particles and impellers | Particles and transition zone | P1 | P2 | MRT |
|---|---|---|---|---|---|---|---|
| 5000 | 2.17 | 24.92 | 4.86 | 9.14 | 1.00 | 1.00 | 3.01 |
| 10000 | 3.71 | 22.97 | 4.88 | 8.06 | 1.00 | 0.94 | 2.92 |
| 20000 | 6.29 | 20.47 | 4.89 | 6.74 | 1.03 | 0.87 | 2.75 |

**Table 5.2** The Relationship between ACNs, P1, P2, and MRT for Different Feed Rates, and the Impeller Speed, Open Area, and Hole Size are Fixed at 400rpm, 0.3 and 4d, Respectively.

| Collision types / Feed rate | Particles and particles | Particles and screen | Particles and impellers | Particles and transition zone | P1 | P2 | MRT |
|---|---|---|---|---|---|---|---|
| 5000 | 5.91 | 37.59 | 5.93 | 25.37 | 1.40 | 1.15 | 3.35 |
| 10000 | 7.95 | 31.63 | 6.04 | 20.71 | 1.43 | 1.04 | 3.15 |
| 20000 | 10.70 | 25.58 | 6.02 | 16.26 | 1.48 | 0.95 | 3.00 |

**Table 5.3** The Relationship between ACNs, P1, P2, and MRT for Different Feed Rates, and the Impeller Speed, Open Area, and Hole Size are Fixed at 1000rpm, 0.3 and 4d, Respectively.

| Collision types / Feed rate | Particles and particles | Particles and screen | Particles and impellers | Particles and transition zone | P1 | P2 | MRT |
|---|---|---|---|---|---|---|---|
| 5000 | 13.04 | 43.92 | 7.07 | 60.69 | 1.93 | 1.18 | 3.62 |
| 10000 | 15.52 | 35.80 | 7.12 | 48.17 | 1.95 | 1.04 | 3.27 |
| 20000 | 19.36 | 29.13 | 7.23 | 38.15 | 2.00 | 0.94 | 3.04 |

**Table 5.4** The Relationship between ACNs, P1, P2, and MRT for Different Feed Rates, and the Impeller Speed, Open Area, and Hole Size Are Fixed at 200rpm, 0.45 and 4d, Respectively.

| **Collision types** / **Feed rate** | **Particles and particles** | **Particles and screen** | **Particles and impellers** | **Particles and transition zone** | **P1** | **P2** | **MRT** |
|---|---|---|---|---|---|---|---|
| 5000 | 0.89 | 13.19 | 3.56 | 5.67 | 1.02 | 0.65 | 2.29 |
| 10000 | 1.61 | 12.72 | 3.49 | 5.38 | 1.05 | 0.62 | 2.20 |
| 20000 | 2.89 | 11.86 | 3.43 | 4.82 | 1.09 | 0.58 | 2.14 |

**Table 5.5** The Relationship between ACNs, P1, P2, and MRT for Different Feed rates, and the Impeller Speed, Open area, and Hole size are fixed at 400rpm, 0.45 and 4d, Respectively.

| **Collision types** / **Feed rate** | **Particles and particles** | **Particles and screen** | **Particles and impellers** | **Particles and transition zone** | **P1** | **P2** | **MRT** |
|---|---|---|---|---|---|---|---|
| 5000 | 2.33 | 22.41 | 4.25 | 17.05 | 1.44 | 0.71 | 2.48 |
| 10000 | 3.27 | 19.30 | 4.25 | 14.50 | 1.47 | 0.65 | 2.34 |
| 20000 | 4.56 | 16.25 | 4.23 | 11.66 | 1.50 | 0.60 | 2.24 |

**Table 5.6** The Relationship between ACNs, P1, P2, and MRT for Different Feed Rates, and the Impeller Speed, Open Area, and Hole Size Are Fixed at 200rpm, 0.30, and 3d, Respectively.

| **Collision types** / **Feed rate** | **Particles and particles** | **Particles and screen** | **Particles and impellers** | **Particles and transition zone** | **P1** | **P2** | **MRT** |
|---|---|---|---|---|---|---|---|
| 5000 | 8.38 | 57.09 | 8.58 | 15.18 | 0.91 | 1.91 | 4.82 |
| 10000 | 13.48 | 51.02 | 8.92 | 12.12 | 0.88 | 1.76 | 4.63 |
| 20000 | 21.47 | 43.00 | 8.80 | 8.56 | 0.85 | 1.63 | 4.25 |

**Table 5.7** The Relationship between ACNs, P1, P2, and MRT for Different Feed Rates, and the Impeller Speed, Open Area, and Hole Size Are Fixed at 200rpm, 0.30, and 5d, Respectively.

| **Collision types** / **Feed rate** | **Particles and particles** | **Particles and screen** | **Particles and impellers** | **Particles and transition zone** | **P1** | **P2** | **MRT** |
|---|---|---|---|---|---|---|---|
| 5000 | 1.16 | 17.25 | 4.01 | 6.33 | 0.98 | 0.72 | 2.40 |
| 10000 | 2.07 | 16.23 | 3.89 | 5.60 | 0.99 | 0.69 | 2.33 |
| 20000 | 3.71 | 15.41 | 3.91 | 4.84 | 1.01 | 0.65 | 2.24 |

The collisions between particles, as well as particles and geometries are related to the number of particles. Therefore, in addition to the collision information, the other key factor impacting the dynamic process is the total number of particles, hereafter termed, particle number, inside the comil. Here two parameters associated with particle number, represented by P1 and P2, are defined in order to discuss the relationship between particle number, ACN, and MRT. P1 is defined as the ratio of particle number in the transition section to the particle number inside the comil (including the transition zone as well as the conical screen section), whereas P2 is the ratio of particle number corresponding to the steady state inside the comil to the total particle number generated during the whole simulation process. According to the definitions of P1 and P2, the absolute values of P1 will be larger than P2 since the total particle number generated during the whole simulation is huge. However, the most valuable information is how they change relatively for different simulation conditions. Thus, the normalized P1 and P2 by the values corresponding to the impeller speed of 200rpm, feed rate of 5000 particles per second, open area of 0.30, and size of holes of 4d are presented in Tables 5.1 to 5.7.  The corresponding MRT is also shown along with the ACN and P1, P2 in these tables so that the relationship between them can be conveniently identified.

The initial simulation conditions in Tables 5.1-5.3 are for the impeller speeds of 200rpm, 400rpm and 1000rpm, respectively. At the same time, for each impeller speed, three different feed rates are simulated: 5000, 10000, 20000 particles per second. The open area and the size of holes are fixed at 0.3 and four times the diameter of a particle, respectively. In Tables 5.4 and 5.5, when compared to Tables 5.1-5.3, the open area is fixed at 0.45 instead of 0.3. Similarly, in Tables 6 and 7, the size of the holes is changed to 3 and

5 times the diameter of a particle, from four times the diameter. Consequently, through examination of different combinations of simulation data, the effect of different parameters, such as impeller speeds, feed rates, open areas and the sizes of holes in the screen, on ACN, P1, P2, and MRT can be revealed. For example, according to Table 5.1 (Table 5.2, Table 5.3), the effect of feed rates for impeller speed of 200rpm (400rpm, 1000rpm) on ACN, P1, P2, and MRT can be obtained. Also, if just the first (second, third) row in Tables1-3 is considered, then the effect of impeller speeds for feed rates of 5000 (10000, 20000) particles per second on ACN, P1, P2, and MRT can be examined.

According to the data presented in Tables 5.1-5.5, the effect on ACN and MRT of impeller speed for different feed rates and open areas of the screen can be obtained. First, it can be seen that all the different types of ACN increase with increasing impeller speed. Second, it can be observed that when the impeller speed is lower, the dominant collision type in the comil is the collisions between the particles and the screen, since the particles can move more freely to the screen without interacting as much with the impeller blade. With increasing impeller speed, the collisions between particles and the transition zone increase quickly and that becomes dominant.

The corresponding results about P1 and P2 show that P1 increases greatly with increasing impeller speed, in contrast, P2 is not sensitive to the change of impeller speed. For example, for the feed rate of 20000 particles per second, the relative change of P1 is 94% when the impeller speed increases from 200rpm to 1000rpm, however, P2 only changes by 8% for the same range of impeller speed. Nevertheless, P2 also shows a slight increase with increasing impeller speed, indicating more particles stay inside the comil, which helps explain the increasing ACNs and MRT with increasing impeller speed. In addition, P2 almost keeps constant when the impeller speed increases from 400rpm to 1000rpm, compared with its change from 200rpm to 400rpm.

According to the analysis above, with increasing impeller speed, more particles enter into the transition zone, as they are driven into the transition zone by the impeller with higher speeds. Therefore, the ACN between particles and the transition zone increases and becomes dominant with increasing impeller speed. The transition zone is an important section in comil where the particles cannot interact with the screen and its holes and cannot leave the system unless they return back to the screen section. This indicates increasing particle number in the transition zone leads to the increase in the MRT as well as the ACN between particles and particles and geometries.

According to Tables 5.1 through 5.7, first, an obvious characteristic is that the ACN between particles and impellers is insensitive to the feed rate at fixed impeller speed. The biggest relative change is only 3.8% in Table 5.6. Second, the ACN between particles increases with increasing feed rate. Third, the other types of ACNs decrease with increasing feed rate. Moreover, all the simulation results indicate that the MRT decreases with increasing feed rate.

In addition, the results about P1 and P2 indicate that the particle fraction in the transition zone is not sensitive to the change of feed rate for fixed impeller speed. For example, the relative change of P1 as seen in Tables 5.1 to 5.7 ranged from about 3.0% to 6.6%. In contrast, the relative change of P2 ranged from 10.8% to 20.3%. Moreover, P2 decreases with increasing feed rate.

The analysis above reveals that the equilibrium particle number fraction inside the comil decreases with increasing feed rate, and this is the main reason why the ACN between the particles and the transition zone, and the particles and the screen decrease with increasing feed rate. Another interesting phenomenon is that the ACN between particles, which increases with increasing feed rate, has the opposite trend as compared to other types of ACN. This observation indicates that the collisions between particles become more frequent with increasing feed rate because there are more particles involved in the system. At the same time, most of particles experience collisions with other particles, rather than with the impellers or screens before they flow out from the comil. Furthermore, the ACN between particles and impellers is almost independent of the feed rate. The collision between particles and impellers is important during the comil process since kinetic energy of particles arises from their collisions with rotating impellers. From the view of collision energy, this type of collision is strong enough to deagglomerate the agglomerates of fine powders so that the finer particles can disperse onto the surface of other larger particles, thus improve the flowability or packing properties of particles. Nonetheless, how different types of collisions occuring in the comil process impact the dry coating or milling quality is an interesting topic to study in the future and is beyond the scope of this paper.

Another interesting observation is that the relative change of ACNs with impeller speeds varies with the feed rate. As previously discussed, MRT exhibits more pronounced effect at lower feed rate when the impeller speed increases from 200 rpm to 1000 rpm. Here, the ACNs show a similar trend, and hence help us better understand the experimental results for coarse acetaminophen (cAPAP) [145], which show in Table 5.2 of the prequel that the coating quality, represented by bulk density and flow function coefficient (FFC), clearly improves when impeller speed increases from 1300rpm to 2600rpm at the low feed rate of 3g/min. In contrast, the FFC only slightly increases at the high feed rate of 20g/min corresponding to the same change of impeller speeds, which is also in line with the simulation results.

Comparing the results in Table 4 with Table 1, and the results in Table 5 with Table 5.2, it can be seen that all the types of ACN decrease with increasing open area. At the same time, the MRT also decreases with increasing open area. This is because there is more area for particles to pass through the screen with increased open area.

The results also show that the P1 values only change slightly when the open area increases from 0.30 to 0.45 for a fixed impeller speed. On the other hand, P2 shows the expected decrease with increased open area. This result is reasonable because there are more opportunities for particles to flow out with increased area of the holes. Consequently, the equilibrium particle number tends to decrease with increasing open area, thus results in the decreasing MRT as well.

Comparing the Table 5.6, Table 5.1 and Table 5.7, corresponding to the hole sizes 3, 4 and 5 times the diameter of a particle while all the other parameters kept fixed, the effect of size of screen hole on the ACN, P1, P2 and the MRT can be obtained. As the data shows, all types of collisions decrease with increasing sizes of the screen holes. At the same time, the MRT also decreases with increasing sizes of the screen holes.

Similar to the effect of open area, P1 does not change as may be expected with increasing sizes of the screen holes. In contrast, P2 increases as expected with decreasing sizes of the holes, indicating that there are more particles staying inside the comil with decreasing hole size. Therefore, the ACN between particles and particles, particles and geometries, and the MRT increase with decreasing hole size. In experiments, two types of screens are used to examine the effect of their hole sizes on the coating quality, represented by FFC [145]. The results indicated that the higher FFC value was achieved at the smaller screen hole size of 457 µm, compared to 610 µm at the impeller speed of 2200rpm. The simulation results show that the P2, ACNs, and MRT increase with decreasing hole size, which is the main reason why smaller screen hole size can better improve the flowability after dry coating.

Based on the data presented in Tables 5.1 to 5.7, the qualitative relationship between ACN, P1, P2 and MRT can be obtained, and is summarized in Table 5.8 in terms of how those parameters vary according to various simulation conditions. In the table, symbols ↑, ↓, and ↕* indicate that the corresponding parameters increase, decrease or do not change appreciably, respectively. As seen, the total four process variables; impeller speed, feed rate, open area, and the size of screen holes can be divided into two categories, according to their relationship with P1, P2, and MRT. The first category includes the impeller speed and its characteristic is to impact the P1, thus MRT. The second category includes all the other variables and its main characteristic is to impact the P2, thus MRT.

**Table 5.8** The Relationship between ACNs, P1, P2, and MRT for Various Impeller Speeds, Feed Rates, Open Areas, and Hole Sizes. ↑ , ↓ , and ↕* Indicate the Corresponding Parameters Increase, Decrease, or Change Slightly, Respectively.

| **Impeller speed** | **Feed rate** | **Open area** | **Hole size** | **Particles and particles** | **Particles and screen** | **Particles and impellers** | **Particles and transition zone** | **P1** | **P2** | **MRT** |
|---|---|---|---|---|---|---|---|---|---|---|
| ↑ | **fixed** | **fixed** | **fixed** | ↑ | ↑ | ↑ | ↑ | ↑ | ↕* | ↑ |
| **fixed** | ↑ | **fixed** | **fixed** | ↑ | ↓ | ↕* | ↓ | ↕* | ↓ | ↓ |
| **fixed** | **fixed** | ↑ | **fixed** | ↓ | ↓ | ↓ | ↓ | ↕* | ↓ | ↓ |
| **fixed** | **fixed** | **fixed** | ↑ | ↓ | ↓ | ↓ | ↓ | ↕* | ↓ | ↓ |

## 5.5 Conclusions

Comil, a promising continuous dry coating device, was simulated to gain an understanding of how its operating parameters influence the mean residence time and residence time distribution; both are generally thought to be important to the performance of flow through devices. The impact of the comil impeller speed, particle feed rate, screen hole size, and screen open area on the MRT was examined via simulations. This was done in order to better understand the corresponding experimental results; more specifically the first three operating parameters. Experiments showed that at lower feed rates, impeller speed has more significant impact on the flowability enhancement [145]. The simulations also show that at lower feed rates, MRT increase is significant as impeller speed increased. However, as the feed rate increased to highest value, the bulk density and FFC both from dry coating experiments did not show any significant increase as the impeller speeds increased. The corresponding simulations also show that the increase in MRT at the highest feed rate is not as significant as was the case at the lowest feed rate. In addition, the simulations showed that MRT increases with the impeller speed at all feed rates simulated. This outcome is generally consistent with the limited experimental results [145]; however, it is counter-intuitive. Limited physical experiments were conducted that corroborated the trend of increased MRT with increased impeller speed. The simulation results for the effect of screen hole size on the MRT were also generally consistent with the outcome from dry coating experiments. Thus overall, the simulation results for MRT as a function of several key parameters indicate that in most cases, increased MRT leads to improved dry coating quality. However, some of the previous experimental results showed that not being the case; for example, at the highest feed rate, further flow improvements were not observed when the impeller speed was increased. As another example, at a fixed impeller speed, low powder feed rate yields lesser dry coating quality although the simulation results indicate higher MRT at lower feed rates. Thus it is evident that MRT alone is not sufficient to explain dry coating experimental results, which is expected to be influenced by both MRT and host particle collisions [158]. These results suggested that the analysis of the process dynamics should be conducted. Therefore, in addition to computing the RTD and MRT, the relationship between average collision number (ACN), number of particles inside the transition zone (region above the cone), and MRT was examined indicating that more particles are driven into the transition zone at higher impeller speed, resulting in longer MRT and larger ACNs. In contrast, the equilibrium number of particles inside the comil decreases with increasing feed rate, open area, and screen hole size, therefore, leading to a decrease in both MRT and ACNs. Those results, provided in the tables, show that the system is in a state of inertial flow and the mass hold-up increases due to increased collisions as the impeller speed is increased. This leads to increased MRT although may not necessarily lead to better performance. This insight and explanation of a seemingly counter-intuitive trend could not be obtained without the results that are provided in this manuscript, and constitute an important outcome of this paper.

In addition, different types of collisions were examined through simulations, such as the collisions between particles, particles and the screen, particles and impeller, and particles and transition zone. The results show that the average collision number for all of the particle collisions increases with the increasing impeller speed. However, when the feed rate increases, the ACN between particles increases and ACN between particles and impellers stays almost constant, whereas the other types of collisions decrease. Thus the collision dynamics changes more drastically in comparison to the trend of the total ACN. Overall, the dominating collision type is that between the particles and screen at lower impeller speeds; however, at higher impeller speeds, it is the collisions between the particles and the transition zone as more particles are driven into the transition zone at higher impeller speeds. The latter type of collisions would not meaningfully contribute towards improved dry coating quality. As may be anticipated, the increase in the open area and the screen hole size leads to poorer collision dynamics and hence poorer coating quality due to the decrease of all of the ACNs since the particles can more easily flow out from the screen.

Overall, through such analysis of collisions types and the spatial distribution of particles in addition to mere computation of MRT, one can gain better process understanding from simulations than in physical experiments where the amount of information that can be gathered is limited. The approach developed here is considered to be general, and is expected to be useful and important for more detailed future studies of comil and similar devices.

# CHAPTER 6

# ADHESION AND FRICTION BETWEEN DRY COATED PARTICLES

## 6.1 Introduction

Surface roughness is one of the major factors that affect adhesion and friction between contacting bodies. Modifying the surface morphology by incorporating nanoparticles has led to the capability to tailor surface properties such as adhesion and friction [159-164]. By introducing nanoscale surface roughness by depositing nanoparticles can reduce the real contact area and greatly alter the adhesive and tribological behavior of micro/nanoscale contacting bodies. The dry coating method, capable of randomly depositing nanoparticles (guest particles) on the surface of micro-sized cohesive particles (host particles) by applying mechanical forces, has proved to be an efficient physical method to manipulate surface properties [91, 165].

However, our understanding of the effects of dry coating on bulk properties of materials is still incomplete since it is difficult to obtain experimental information about particle scale. Vital information such as contacts or deformation limits theoretical progress, with the result that accurate models describing interactions between dry coated particles are not readily available. Previous experimental investigations have shown that surface area coverage (SAC), defined as the area ratio of surface covered by the guest particles to the total surface of the host particle, is crucial to control interparticle adhesion force [165-167]. Therefore, attempts have been made to establish a model of adhesion based on the SAC[165, 167] According to two critical values of SAC, contacts between coated particles can be divided into three categories: host-host (HH), host-guest (HG), and guest-guest (GG) contacts [165]. There is a crossover in the nature of contacts from HH to HG, and from HG to GG as the SAC is increased. Figure 6.1 shows the schematics of these three different types of contacts. The large and small particles represent the host and guest particles, respectively. Although the previous theoretical model assumed that only one specific type of contact could appear for a specific SAC [165], Figure 6.1 shows that three different types of contacts can exist for a given SAC, depending upon how two dry coated particles are brought into contact. Consequently, all the three contacts can simultaneously contribute to the adhesion and friction for the assembly of dry coated particles. Determining the probabilities of various types of contacts as a function of experimental conditions is key to establish a more accurate theoretical model to help us better understand the bulk behaviors of dry coated particles. So far, such a model is neither available nor the friction between dry coated particles as a function of SAC been systematically explored in previous research which is essential for dissipation of particle assembly as well as particle dynamics [168].

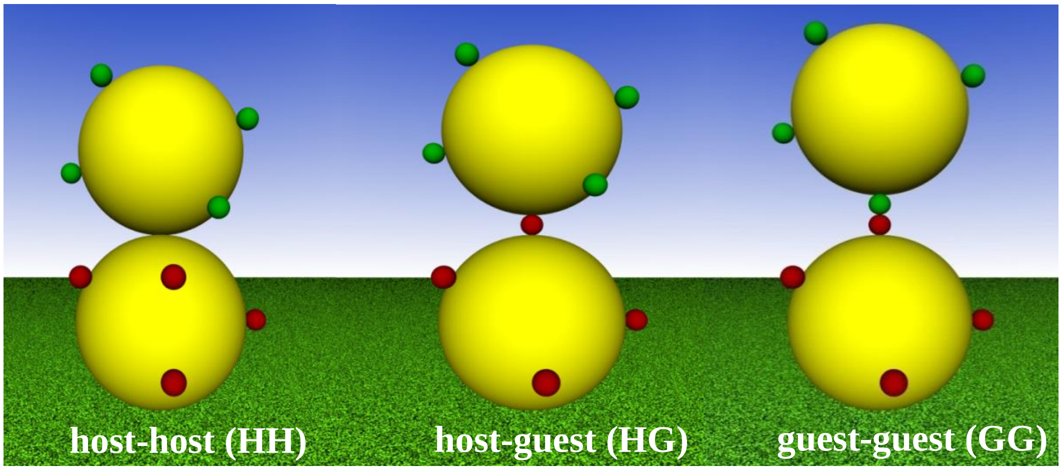

**Figure 6.1** Schematics of host-host (HH), host-guest (HG), and guest-guest (GG) contacts between dry coated particles at a given surface area coverage (SAC). Large (yellow) and small particles (red and green) represent the host and guest particles, respectively.

The aim of this study is to first investigate the adhesion and friction between dry contacts formed by two micro-sized particles with nanoscale surface roughness using numerical modeling. Next, to develop a probabilistic model that can predicate the probabilities of HH, HG, and GG contacts as a function of the SAC. The predictions from the theoretical model are in good agreement with simulation results. Moreover, the research can be of great relevance to other systems that are characterized by contacts between surfaces with nanoscale roughness.

## 6.2 Numerical Method

Nanoparticles with Gauss size distribution are randomly and successively generated and coated on the surfaces of two initially separate large host particles. The variance of nanoparticles size distribution is fixed at 10% of the mean particle size. This study does not allow for an overlap between any two nanoparticles. Due to the large difference between the host and guest particle size, there is a huge amount of nanoparticles on the surface of host particles. For example, assuming host and guest particles sizes are 40 micrometers and 20 nanometers respectively, there are more than one million guest particles on the surface of host particles at the SAC of 100%. A three-dimensional simulation of such a huge amount of particles would require significant computational intensity. However, there is no need to retain all guest particles during the simulations since not every individual particle on the surface of the host particle has the opportunity to contact with other particles. Consequently, they do not contribute anything to the adhesion and friction forces and we can discard some particles without influencing the simulation results. Those particles which contribute to the adhesion and friction forces are reserved in the simulations.

Next, one of the host particles and all the attached guest particles on this host particle remain in fixed positions and the other host particle and all the attached guest particles on its surface are displaced toward the previously fixed host particle in an increment of $2.0\times10^{-6}$ nm per simulation step. The increment is sufficiently small so that we can detect the changes due to the contact force. After each step, the distances between the particles are computed. Two particles are regarded to be in contact if the following equation is satisfied:

$$\delta = |\vec{r}_i - \vec{r}_j| - (r_i + r_j) < 0 \tag{6.1}$$

where $\delta$ is normal overlap between two particles. $\vec{r}_i$, and $\vec{r}_j$ are vectors of positions of *ith* and *jth* particles, $r_i$ and $r_j$ are their individual particle radii, respectively.

Once two particles come into contact, they are inevitably deformed due to their finite elasticity. In an attempt to characterize the relationship between contact force and deformation for adhesive contact between solids and solids, Johnson-Kendall-Roberts (JKR) [20], Derjaguin-Muller-Toporov (DMT)[21], and Maugis models [22] have been developed so far. It is well known that the JKR, DMT, and Maugis models are complementary and apply to different situations characterized by a non-dimensional transition parameter $\mu$ or $\lambda$ [23]:

$$\mu = \left(\frac{R_e w^2}{E^{*2} z_0^3}\right)^{1/3} = \frac{\lambda}{1.16} \tag{6.2}$$

where $\frac{1}{R_e} = \frac{1}{r_i} + \frac{1}{r_j}$, $w$, $E^* = \left(\frac{1-v_i^2}{E_i} + \frac{1-v_j^2}{E_j}\right)^{-1}$ are equivalent radius, work of adhesion and combined elastic modulus. $z_0$ is equilibrium separation distance of the surfaces in contact ($z_0 \approx 0.4$nm) [24]. $v_i$, $v_j$, $E_i$, $E_j$ represent the Poisson's ratios, and Young's moduli of *ith* and *jth* particles. Both $\mu$ and $\lambda$ are a measure of the ratio of elastic deformation resulting from adhesion to the effective range of surface forces [25]. Johnson and Greenwood presented an adhesion map based on transition parameter $\lambda$. If $\lambda > 5.0$, the JKR model applies and if $\lambda < 0.1$ the DMT model applies. $0.1 < \lambda < 5.0$ corresponds to the transition regime between JKR and DMT models and Maugis model applies [25]. All three theories predict that a finite negative force, often referred to as pull-off force or adhesion force, is required to separate the surfaces in contact. Unlike JKR and DMT model, where there is an explicit expression for adhesion force, this is not the case with the Maugis transition regime. Carpick et al. propose a convenient approximation by curve-fitting to calculate adhesion for three different types of contact models [169].

$$F_{Adh} = \left(\frac{1}{4}\left(\frac{4.04\lambda^{1.4}-1}{4.04\lambda^{1.4}+1}\right) - \frac{7}{4}\right)\pi w R_e \tag{6.3}$$

According to Equation 6.3, when $\lambda$ increases from 0 to infinite, $F_{Adh}$ smoothly transits from $-2\pi w R_e$ to $-1.5\pi w R_e$ , corresponding to the adhesion force of DMT and JKR models.

The friction force can generally be assumed to be directly proportional to the contact area. When two coated particles are brought into contact, it is possible that multiple contacts exist between particles. In this case, the total contact force is the summation of the frictions induced by all the individual contacts.

$$F_f = \tau \sum \pi b_i^2 \tag{6.4}$$

where $F_f$ is the friction force, $b_i$ is the effective contact radius within which the friction acts, and $\tau$ is the interfacial shear strength. For JKR and DMT models, $b_i$ can be assumed to be the same with JKR or DMT contact radius [160, 170]. However, the Maugis model assumes that the adhesive force acts in an annular region immediately outside of the contact radius. Therefore, $b_i$ is expected to lie between the radius of the contact circle and the outer radius [170, 171].

Since nanoparticles can locate anywhere on the surface of the host particles, various configurations are possible for a specific SAC. In this study, the mean values of 200 configurations are presented and analyzed for a fixed SAC. Also, test the results for host particle size of 20 micrometers and guest particle size of 20 nanometers for the range of SAC from 0.0001 to 0.1 using 2000 configurations and similar results were found.

## 6.3 Simulation Results

Figure 6.2 depicts adhesion and friction forces as a function of compressive load for various SACs. As predicted, both forces increased with increasing compressive force. This is due to the number of particles that come into contact increases with increasing load, as well as larger deformation for the higher load. These simulation results are in qualitative agreement with previous experimental and molecular dynamic simulation results [160, 165, 170, 172].

A surprising outcome (Figure 6.2(a)) indicates that the adhesion force does not monotonously decrease with increasing SAC. The adhesion force initially decreases with increasing SAC, and then reaches a minimum value at SAC of about 0.05; thereafter it increases with increasing SAC. This behavior is different from the predication of the previous model, indicating that the adhesion force is a monotonous decreasing function of SAC. The friction force shows similar behavior as it reaches a minimum value at SAC of 0.05 as well (Figure 6.2(b)).

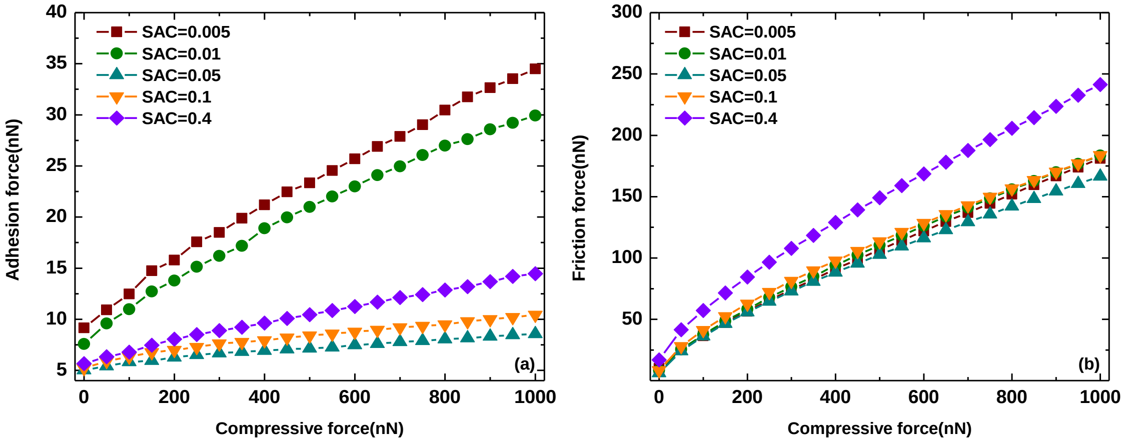

**Figure 6.2** Adhesion and friction forces as a function of compressive load. (a) adhesion forces (b) friction forces. Host particle size and guest particle sizes are 20 micrometers and 20 nanometers, respectively.

Having access to full particle scale information allows us to explore the effects of contacts between particles on the adhesion and friction properties. Figure 6.3 illustrates the relationship between adhesion, friction, and the number of different types of contacts, and SAC for various size ratios of host to guest particles and compressive forces. The adhesion and friction forces are normalized by their values corresponding to the SAC of $10^{-4}$ in order to show them together with contact number. It can be observed that the adhesion and friction forces initially decrease greatly with increasing SAC, and then achieve a plateau value with some fluctuations. With further increase of SAC, both the forces increase nominally. On the other hand, HH contacts rapidly decrease to zero, which is similar to the initial trend of adhesion and friction forces. In contrast, HG contacts increase with increasing SAC and then rapidly decrease to zero and GG contacts always increase with increasing SAC. The dash lines in Figure 6.3 indicate the different regions dominated by various types of contacts. Combining the trends of adhesion, friction, and the various types of contacts with SAC, it can be concluded that with increasing SAC, HH, HG, and GG contacts sequentially dominate the behavior of adhesion and friction between particles. Another important outcome from Figure 6.3 is that the transition of dominated contacts from HG to GG types results in the minimum adhesion and forces.

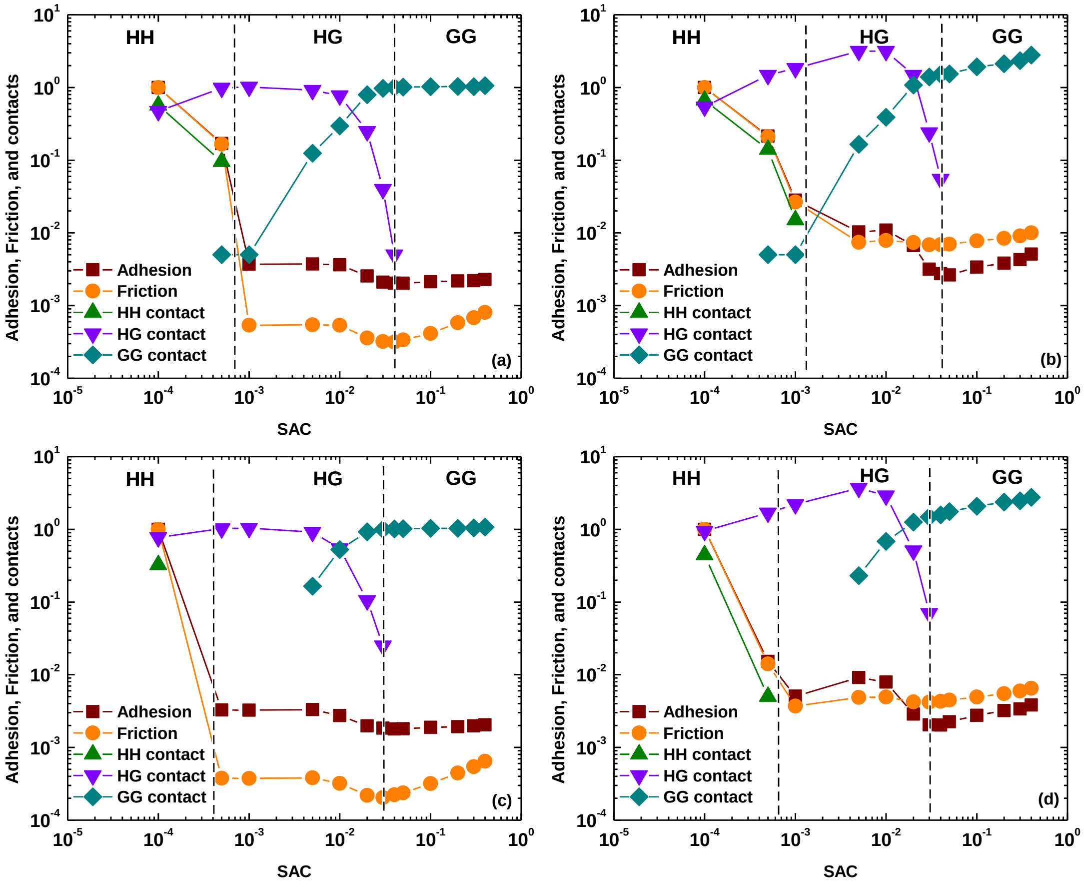

**Figure 6.3** Relationship between adhesion, friction, numbers of various types of contacts, and surface area coverage for various host and guest particle sizes and compressive forces.

## 6.4 Analytical Model

The results of simulations indicate there are three distinct regions dominated by different types of contacts. Theoretically, the total adhesion force between two dry coated particles can be computed using the following equation:

$$F_{Adh} = F_{HH} + F_{HG} + F_{GG} \tag{6.5}$$

$F_{Adh}$, $F_{HH}$, $F_{HG}$, and $F_{GG}$ represent the total adhesion forces, and adhesion forces induced by host-host, host-guest, and guest-guest contacts. From Equation 6.3, the dominating factor influencing adhesion force is the equivalent radius $R_e$. Next, Equation 6.5 can be approximately rewritten as

$$F_{Adh} \approx C\pi w(N_{HH}R_H + 2N_{HG}R_G + N_{GG}R_G) \tag{6.6}$$

where $C$ is a constant. $N_{HH}$, $N_{HG}$, $N_{GG}$ are the contact numbers of HH, HG, and GG contacts and $R_H$, $R_G$ are radius of host and guest particles. Considering that $R_H$ is usually three orders larger than $R_G$, Equation 6.6 can be simplified into two Equations 6.7a and 6.7b:

$$F_{Adh} \approx C\pi w N_{HH} R_H \quad \text{if} \;\; N_{HH} \neq 0 \tag{6.7a}$$

$$F_{Adh} \approx C\pi w R_G(2N_{HG} + N_{GG}) \quad \text{if} \;\; N_{HH} = 0 \tag{6.7b}$$

Therefore, different types of contacts can dominate adhesion force, depending upon the contact numbers of various types.

Theoretical analysis indicates that the contact type is crucial in understanding the behavior of adhesion and friction forces. Therefore, we devote our efforts in establishing a model that would predict what types of contact appear under a given SAC. We consider a micro-sized large particle coated with nanoparticles in adhesive contact with another same large particle (Figure 6.4(a)). The apertures of two cones are defined as $\theta_1$ and $\theta_2$, indicated in Figures 6.4(b) and (c). $\theta_1$ defines the maximum angle within which the contacts can occur. $\theta_2$ defines the angle that if there is at least one guest particle within it, it is not possible to have HH contact anymore. Assume the surface areas within the $\theta_1$ and the $\theta_2$ are $S_1$ and $S_2$, which are given as:

$$S_1 = 2\pi R_H^2(1 - cos\theta_1),\ cos\,\theta_1 = \frac{R_H - r}{R_H + r} \tag{6.8}$$

$$S_2 = 2\pi R_H^2(1 - cos\theta_2),\ cos\,\theta_2 = \frac{R_H}{R_H + r} \tag{6.9}$$

where $R_H$ and $r$ represent the radii of host and guest particles, respectively. According to the values of $S_1$, $S_2$, and the size of individual guest particles, the total positions $M_1$ and $M_2$ available for guest particles within the $\theta_1$ and $\theta_2$ can be computed with the assumption that all the nanoparticles are individually distributed on the surfaces of the host particles

$$M_1 = \frac{S_1}{4r^2} \tag{6.10}$$

$$M_2 = \frac{S_2}{4r^2} \tag{6.11}$$

The corresponding SAC is expressed as:

$$SAC = N_g \frac{\pi r^2}{S_1} \tag{6.12}$$

where $N_g$ is the total number of guest particles on the surface area of host particle within $\theta_1$.

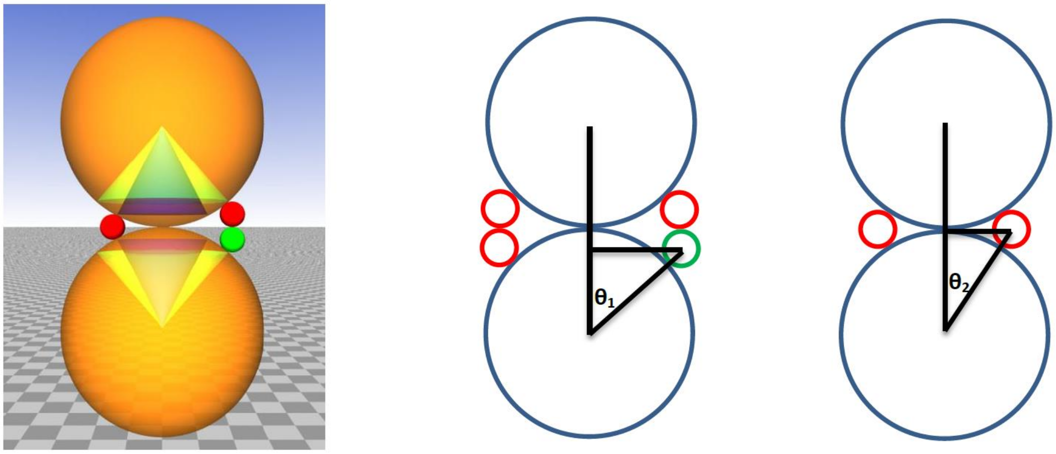

**Figure 6.4** Schematics about the maximum contact angles. Large and small particles represent the host and guest

A total of the number of ways that *Ng* guest particles deposit on the $M_1$ positions on the surfaces of two host particles can be calculated as: $C_{M_1}^{N_g} C_{M_1}^{N_g} (C_{M_1}^{N_g} = \frac{M_1!}{N_g!(M_1-N_g)!})$. In order to have HH contact, guest particles cannot be within the $M_2$ zone. In terms of the first host particle, all available positions for $N_g$ guest particles are ($M_1$-$M_2$). On the other hand, for the second host particle, the guest particles associated with it can occupy neither any position within $M_2$ nor *Ng* positions which have been occupied by *Ng* guest particles associated with the first host particle. Therefore, the probability corresponding to the HH contacts can be written as:

$$P_{HH} = \frac{C_{M1-M2}^{N_g} C_{M1-M2-N_g}^{N_g}}{C_{M1}^{N_g} C_{M1}^{N_g}} \tag{6.13}$$

Considering the GG contact, the $N_g$ guest particles associated with the first and second host particles should occupy $M_1$ and $M_2$ zone in such a way that at least two of them should be in the same positions. Therefore, the probability for GG contact can be expressed as:

$$P_{GG} = \frac{C_{M1}^{N_g}(C_{M1}^{N_g} - C_{M1-N_g}^{N_g})}{C_{M1}^{N_g} C_{M1}^{N_g}} = 1 - \frac{C_{M1-N_g}^{N_g}}{C_{M1}^{N_g}} \tag{6.14}$$

The total probability for HH, HG, and GG contacts should equal to 1. Therefore, the probability for HG contact can be calculated as:

$$P_{HG} = \frac{C_{M1}^{N_g} C_{M1-N_g}^{N_g} - C_{M1-M2}^{N_g} C_{M1-M2-N_g}^{N_g}}{C_{M1}^{N_g} C_{M1}^{N_g}} \tag{6.15}$$

Figure 6.5 shows the results of $P_{HH}$, $P_{HG}$, and $P_{GG}$ as a function of SAC for various size ratios of host to guest particles. It can be seen that the $P_{HH}$ decreases with increasing SAC while the $P_{HG}$ increases and achieves a maximum value and then begins to decrease with increasing SAC. In contrast, $P_{GG}$ always increases with increasing SAC. Previous results indicate the critical SAC for transition from *HH* to *HG* that can be calculated using $\frac{1.21}{1+2(\frac{R}{r})}$ [165]. To substitute R=20μm, r=40nm, the critical SAC equals to $1.21\times10^{-3}$. Similarly, critical SACs are $6.05\times10^{-4}$ and $3.02\times10^{-4}$ for R=20μm, r=20nm and R=40μm, r=20nm, respectively. According to Figure 6.5, for the host particle radius of 20μm and guest particle radius of 40nm, $P_{HH}$, $P_{HG}$, and $P_{GG}$ are about 6.2%, 93.5%, and 0.3%, respectively, at the SAC of $1.21\times10^{-3}$, indicating that the type of HG contacts dominate the total contacts, in agreement with the previous results.

The surprising outcomes from our current model illustrate that the predicted critical SAC for the transition from HG to GG contact is much lower in comparison with the previously accepted value of about 0.3. Moreover, this critical SAC varies with size ratios of host to guest particle size, instead of a constant for different size ratios in the previous theory [165].

The contact probabilities, defined as the number ratio of a specific contact type to the total contacts, have been calculated from simulation results as shown in Figures 6.5(b) and (c), along with their corresponding theoretical predications. As seen, the general trend for various size ratios of host to guest particles is similar. The probability for HH contact decreases into zero as the SAC increases. At the same time, the probability for HG contact rapidly increases to almost 100% and then begins to decrease to zero. In contrast, the probability for GG contact always keeps increasing with the increase of SAC until it reaches 100%. Therefore, the predications of the model indicate that with the variation of SAC, the interparticle contacts can transit from one type of contact to another. Moreover, theoretical predications quantitatively agree with the simulation results for various conditions, indicating the model captures the correct physics behind the contacts of two dry coated particles.

We noted that other factors may further impact the exact value of adhesion and friction forces in the experiment, which are not accounted for in the current model. In particular, instead of individual nanoparticles, small agglomerates tend to exist on the surface of host particles in the experiment since it is hard to completely break the agglomerates of nanoparticles [166, 167, 173]. The SAC calculated from the assumption of individual distribution of nanoparticles on the host particle surface is larger than the real SAC [173]. This also explains why the predication of SAC corresponding to transition HG to GG contacts is much lower than experimental observation [165]. Therefore, extension of the current model should further incorporate the impact of agglomerate on the SAC and improve the quality of the agreement between numerical predications and experimental measurements.

We further noted that the size ratios between host particles to guest particles are associated with the contact probabilities (Figure 6.5(a)). Therefore, it is more accurate to establish a numerical model based on experimentally-measured particle size distribution. However, the change of size ratio only quantitatively influences our results; the qualitative predications, based on more realistic size distribution, should follow the same trend with the current model. In addition, other material parameters such as Poisson's ratio, Young's modulus, and surface energy can quantitatively influence the specific values obtained from the simulations. Therefore, the exact values of those material parameters should be used in order to better compare with experimental measurements.

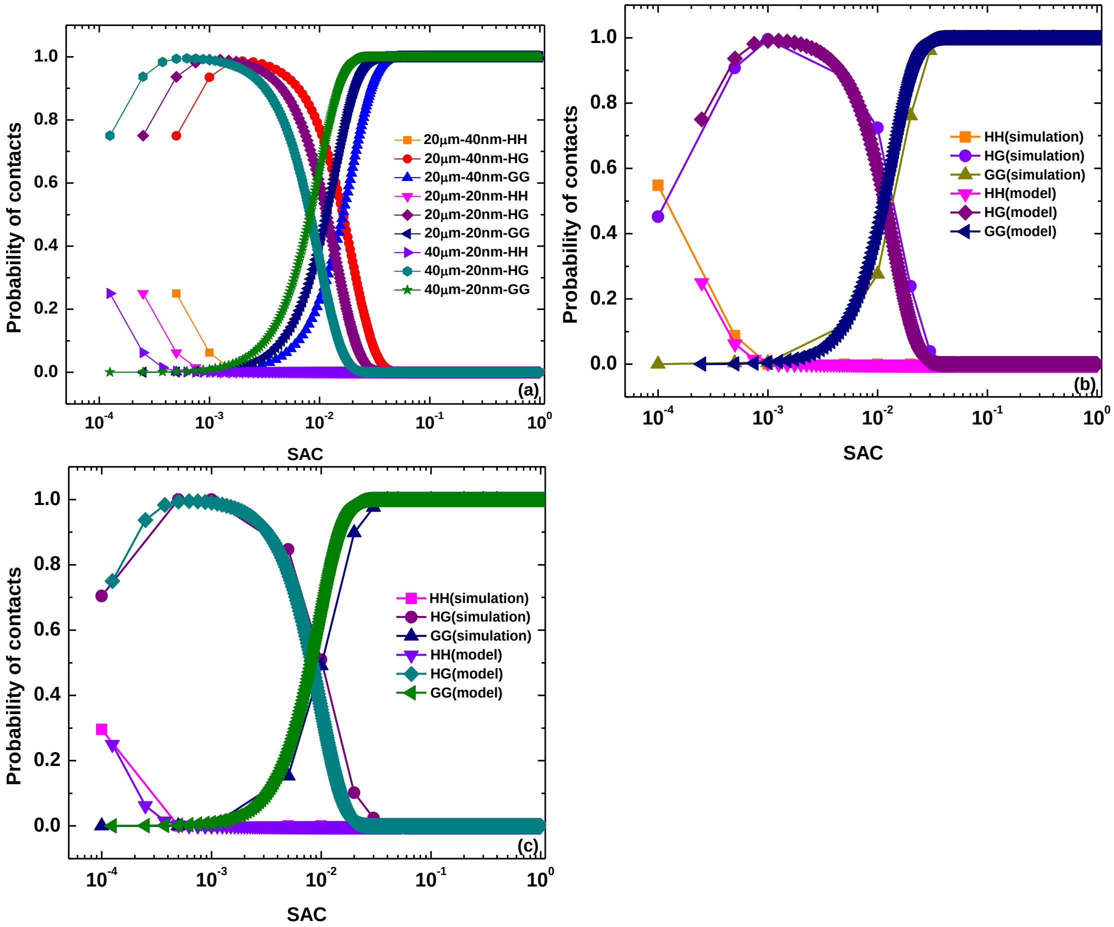

**Figure 6.5** Theoretical predictions and comparison with numerical results.

## 6.5 Conclusions

Numerical simulation has been used to investigate how the dry coating process influences the interparticle adhesion and friction force. Results obtained indicate both adhesion and friction first decrease with increasing surface area coverage (SAC), and then achieve a steady value with small fluctuations The host-host (HH) contact number decreases quickly with increasing SAC and host-guest (HG) contacts first almost keeps a steady value and then decreases to zero. In contrast, the guest-guest (GG) contacts increases and achieves a steady value with increasing SAC. By examining the number of various types of contacts and adhesion and friction force for different SACs, it can be seen that there are three different regions that are each dominated by various types of contacts. A theoretical model has been derived and the probabilities corresponding to different types of contacts predicated by the model are in good agreement with numerical simulation results.

# CHAPTER 7

# CONCLUSIONS AND FUTUTE WORK

## 7.1 Conclusions

In this thesis, numerical simulations were conducted to investigate the behaviors of assembly of individual particles, focusing on the connections between bulk properties and individual particle scale variables. In this chapter, the major conclusions of this thesis are summarized and some possible research directions based on the current research are proposed as well.

(1) For the particle packing without external compressive loading, porosity is influenced by the particle scale variables such as particle size, surface energy, and particle aspect ratio. According to the radial distribution function, microscopic packing structures as a function of particle size, surface energy, and aspect ratio are revealed, which can help understand the relationship between porosity and those particle scale variables. When particle assembly is subject to the external compressive loading, the heterogeneous force networks are developed within the jammed particle system. The simulation results show that there are about 60% of strong contacts forming the chainlike structures. In contrast, there are about 32%-45% of weak contacts that form the chainlike structures, increasing with increasing pressures.

(2) DEM modelling of particle processing devices such as conical screen mill (comil), magnetically assisted impaction mixing (MAIM) were conducted. Comil is well-known as a continuous delumping/milling and more recently, a coating device. Hence, the particular interest for comil modeling is to investigate the effect of the various operating

parameters such as impeller speed, feed rate, screen hole size, and open area, on the residence time distribution (RTD) and mean residence time (MRT). Particle scale information such as collision rate between particles, and particles and various geometries, particle number distribution inside the comil is computed based on the simulation results as well. Then the relationship between the mean residence time, collision rate, and particle number distribution is presented. MAIM is capable of mixing nanomaterials at sub-agglomerate scale. The agglomerates have been introduced in this DEM simulation in order to capture the process of breakage of agglomerates during the MAIM process. The simulation results indicate that the smaller magnets lead to the better homogeneity of mixing at fixed surface energy and mass ratio of magnets to non-magnets, in good agreement with the previously published experimental results.

(3) Flowability is another important bulk property of cohesive particles. Dry coating is an efficient method to modify the surface properties of the cohesive fine powders, thus improve the flowability. The numerical simulations, along with the theoretical analysis, are performed to help better understand the interparticle force between dry coated particles. The results show that there are three different regions that are each dominated by the host-host, host-guest, and guest-guest contacts. Moreover, the critical SAC for the transition of HG to GG contacts is lower than previously estimated value.

## 7.2 Future work

It is demonstrated in this thesis that the DEM simulation is a useful tool for modeling bulk behaviors and particle dynamics as a function of material properties and operating parameters. Based on the current research, the following aspects need to be further pursued:

(1) As mentioned in Chapters 1 and 2, the packing properties are investigated using monodisperse and bidisperse systems. However, experimental samples usually have a size distribution and more complex shape. Therefore, it is interesting to systematically investigate how the particle size distribution and complex shape impact the packing properties.

(2) Various particle processing devices are applied in industries. Therefore, it is important to simulate other particle processing devices and reveal the connections between the performance of the devices and collision dynamics inside the devices.

(3) In Chapter 6, the interparticle force between dry coated particles is investigated in this research. However, the connection between bulk properties such as angle of repose, flow function coefficient and the interaction of individual particles needs further investigation and the predicative models should be developed.

(4) Multi-scale simulation of dry-coating process. Dry coating poses a great challenge to the DEM modeling since its intrinsic multi-scale properties and various manners of inputting energy into the system depending on the devices used. Some key processes involved in the dry coating need further investigation, such as breakage of nanoparticle agglomerates induced by collision force, attachment of nanoparticles on the surface of host particles, interaction among nanoparticles, agglomerates of nanoparticles, and relatively large host particles. Combing phenomenological equations with DEM modeling perhaps can boost progress on numerical modeling of dry coating.

(5) Based on the experimental results and DEM simulations, more accurate predicative models should be developed in the future, such as a packing model accounting for shape effect and a mixing model accounting for the effect of agglomerates.

# REFERENCES

[1] I. S. Aranson, L. S. Tsimring, Patterns and collective behavior in granular media: Theoretical concepts, Reviews of Modern Physics, 78 (2006) 641-692.

[2] P. A. Cundall, O. D. L. Strack, A discrete numerical model for granular assemblies, Géotechnique, 29 (1979) 47-65.

[3] G. R. Chandratilleke, A. B. Yu, R. L. Stewart, J. Bridgwater, Effects of blade rake angle and gap on particle mixing in a cylindrical mixer, Powder Technology, 193 (2009) 303-311.

[4] Y. Kaneko, T. Shiojima, M. Horio, Numerical analysis of particle mixing characteristics in a single helical ribbon agitator using DEM simulation, Powder Technology, 108 (2000) 55-64.

[5] F. Bertrand, L. A. Leclaire, G. Levecque, DEM-based models for the mixing of granular materials, Chemical Engineering Science, 60 (2005) 2517-2531.

[6] C. A. Radeke, B. J. Glasser, J. G. Khinast, Large-scale powder mixer simulations using massively parallel gpuarchitectures, Chemical Engineering Science, 65 (2010) 6435-6442.

[7] P. Y. Liu, R. Y. Yang, A. B. Yu, DEM study of the transverse mixing of wet particles in rotating drums, Chemical Engineering Science, (2012).

[8] B. Chaudhuri, A. Mehrotra, F. J. Muzzio, M. S. Tomassone, Cohesive effects in powder mixing in a tumbling blender, Powder Technology, 165 (2006) 105-114.

[9] X. Deng, J. V. Scicolone, R. N. Davé, Discrete element method simulation of cohesive particles mixing under magnetically assisted impaction, Powder Technology, 243 (2013) 96-109.

[10] X. An, R. Yang, K. Dong, A. Yu, DEM study of crystallization of monosized spheres under mechanical vibrations, Computer Physics Communications, 182 (2011) 1989-1994.

[11] J. F. Jerier, V. Richefeu, D. Imbault, F. V. Donzé, Packing spherical discrete elements for large scale simulations, Computer Methods in Applied Mechanics and Engineering, 199 (2010) 1668-1676.

[12] R. Y. Yang, R. P. Zou, A. B. Yu, Computer simulation of the packing of fine particles, Physical Review E, 62 (2000) 3900-3908.

[13] T. Jia, Y. Zhang, J. K. Chen, Y. L. He, Dynamic simulation of granular packing of fine cohesive particles with different size distributions, Powder Technology, 218 (2012) 76-85.

[14] R. Y. Yang, R. P. Zou, A. B. Yu, S. K. Choi, Characterization of interparticle forces in the packing of cohesive fine particles, Physical Review E, 78 (2008) 031302.

[15] X. Deng, R. Davé, Dynamic simulation of particle packing influenced by size, aspect ratio and surface energy, Granular Matter, 15 (2013) 401-415.

[16] R. Dave, W. Chen, A. Mujumdar, W. Wang, R. Pfeffer, Numerical simulation of dry particle coating processes by the discrete element method, Advanced Powder Technology, 14 (2003) 449-470.

[17] W. Chen, R. N. Dave, R. Pfeffer, O. Walton, Numerical simulation of mechanofusion system, Powder Technology, 146 (2004) 121-136.

[18] Y. Tsuji, T. Tanaka, T. Ishida, Lagrangian numerical simulation of plug flow of cohesionless particles in a horizontal pipe, Powder Technology, 71 (1992) 239-250.

[19] R. D. Mindlin, Compliance of elastic bodies in contact, Journal of Applied Mechanics., 16 (1949) 259-268.

[20] K. L. Johnson, K. Kendall, A. D. Roberts, Surface energy and the contact of elastic solids, Proceedings of the Royal Society of London. A., 324 (1971) 301-313.

[21] B. V. Derjaguin, V. M. Muller, Y. P. Toporov, Effect of contact deformations on the adhesion of particles, Journal of Colloid and Interface Science, 53 (1975) 314-326.

[22] D. Maugis, Adhesion of spheres: The JKR-DMT transition using a dugdale model, Journal of Colloid and Interface Science, 150 (1992) 243-269.

[23] D. Tabor, Surface forces and surface interactions, Journal of Colloid and Interface Science, 58 (1977) 2-13.

[24] J. N. Israelachvili, Intermolecular and surface forces: Revised third edition, Elsevier Science 2011.

[25] K. L. Johnson, J. A. Greenwood, An adhesion map for the contact of elastic spheres, Journal of Colloid and Interface Science, 192 (1997) 326-333.

[26] R. Y. Yang, R. P. Zou, A. B. Yu, Effect of material properties on the packing of fine particles, Journal of Applied Physics, 94 (2003) 3025-3034.

[27] X. Z. An, R. Y. Yang, R. P. Zou, A. B. Yu, Effect of vibration condition and inter-particle frictions on the packing of uniform spheres, Powder Technology, 188 (2008) 102-109.

[28] K. Z. Y. Yen, T. K. Chaki, A dynamic simulation of particle rearrangement in powder packings with realistic interactions, Journal of Applied Physics, 71 (1992) 3164-3173.

[29] L. E. Silbert, D. Ertaş, G. S. Grest, T. C. Halsey, D. Levine, Geometry of frictionless and frictional sphere packings, Physical Review E, 65 (2002) 031304.

[30] L. E. Silbert, G. S. Grest, J. W. Landry, Statistics of the contact network in frictional and frictionless granular packings, Physical Review E, 66 (2002) 061303.

[31] J. W. Landry, G. S. Grest, L. E. Silbert, S. J. Plimpton, Confined granular packings: Structure, stress, and forces, Physical Review E, 67 (2003) 041303.

[32] G. D. Scott, D. M. Kilgour, The density of random close packing of spheres, Journal of Physics D: Applied Physics, 2 (1969) 863.

[33] K. J. Dong, R. Y. Yang, R. P. Zou, A. B. Yu, Role of interparticle forces in the formation of random loose packing, Physical Review Letters, 96 (2006) 145505.

[34] J. F. Favier, M. H. Abbaspour-Fard, M. Kremmer, Modeling nonspherical particles using multisphere discrete elements, Journal of Engineering Mechanics, 127 (2001) 971-977.

[35] R. Bharadwaj, W. R. Ketterhagen, B. C. Hancock, Discrete element simulation study of a freeman powder rheometer, Chemical Engineering Science, 65 (2010) 5747-5756.

[36] R. P. Jensen, P. J. Bosscher, M. E. Plesha, T. B. Edil, DEM simulation of granular media-structure interface: Effects of surface roughness and particle shape, International Journal For Numerical And Analytical Methods In Geomechanics, 23 (1999) 531-547.

[37] J. F. Favier, M. H. Abbaspour-Fard, M. Kremmer, A. O. Raji, Shape representation of axisymmetrical, non-spherical particles in discrete element simulation using multi-element model particles ulation using multi-element model particles, Engineering Computations, 16 (1999) 467-480.

[38] M. Kodam, R. Bharadwaj, J. Curtis, B. Hancock, C. Wassgren, Force model considerations for glued-sphere discrete element method simulations, Chemical Engineering Science, 64 (2009) 3466-3475.

[39] H. Kruggel-Emden, S. Rickelt, S. Wirtz, V. Scherer, A study on the validity of the multi-sphere discrete element method, Powder Technology, 188 (2008) 153-165.

[40] L. Meng, P. Lu, S. Li, J. Zhao, T. Li, Shape and size effects on the packing density of binary spherocylinders, Powder Technology, 228 (2012) 284-294.

[41] J. Zhao, S. Li, R. Zou, A. Yu, Dense random packings of spherocylinders, Soft Matter, 8 (2012) 1003-1009.

[42] G. D. Scott, Packing of spheres: Packing of equal spheres, Nature, 188 (1960) 908-909.

[43] K. Autumn, M. Sitti, Y.A. Liang, A.M. Peattie, W.R. Hansen, S. Sponberg, T.W. Kenny, R. Fearing, J.N. Israelachvili, R.J. Full, Evidence for van der Waals adhesion in gecko setae, Proceedings of the National Academy of Sciences, 99 (2002) 12252-12256.

[44] Y. Johno, M. Satomi, K. Nakashima, T. Shigematsu, B. Ono, Numerical simulation of particle settling and cohesion in liquid, Journal of Physics: Conference Series, 147 (2009) 012072.

[45] S. R. Williams, A. P. Philipse, Random packings of spheres and spherocylinders simulated by mechanical contraction, Physical Review E, 67 (2003) 051301.

[46] S. Li, J. Zhao, P. Lu, Y. Xie, Maximum packing densities of basic 3d objects, Chinese Science Bulletin, 55 (2010) 114-119.

[47] C. Ghoroi, L. Gurumurthy, D. J. McDaniel, L. J. Jallo, R. N. Davé, Multi-faceted characterization of pharmaceutical powders to discern the influence of surface modification, Powder Technology, (2012).

[48] T. Jia, Y. Zhang, J. K. Chen, Simulation of granular packing of particles with different size distributions, Computational Materials Science, 51 (2012) 172-180.

[49] J. L. Finney, Random packings and the structure of simple liquids. I. The geometry of random close packing, Proceedings of the Royal Society of London. Series A, Mathematical and Physical Sciences, 319 (1970) 479-493.

[50] W. Alan, R. W. Stephen, P. P. Albert, Effect of particle shape on the density and microstructure of random packings, Journal of Physics: Condensed Matter, 19 (2007) 406215.

[51] G. D. Scott, Radial distribution of the random close packing of equal spheres, Nature, 194 (1962) 956-957.

[52] G. Mason, Radial distribution functions from small packings of spheres, Nature, 217 (1968) 733-735.

[53] E. A. J. F. Peters, M. Kollmann, T. M. A. O. M. Barenbrug, A. P. Philipse, Caging of a d-dimensional sphere and its relevance for the random dense sphere packing, Physical Review E, 63 (2001) 021404.

[54] A. Wouterse, S. Luding, A. P. Philipse, On contact numbers in random rod packings, Granular Matter, 11 (2009) 169-177.

[55] P. P. Albert, The random contact equation and its implications for (colloidal) rods in packings, suspensions, and anisotropic powders, Langmuir, 12 (1996) 1127-1133.

[56] T. S. Majmudar, R. P. Behringer, Contact force measurements and stress-induced anisotropy in granular materials, Nature, 435 (2005) 1079-1082.

[57] H. A. Makse, D. L. Johnson, L. M. Schwartz, Packing of compressible granular materials, Physical Review Letters, 84 (2000) 4160-4163.

[58] J. H. Snoeijer, T. J. H. Vlugt, M. van Hecke, W. van Saarloos, Force network ensemble: A new approach to static granular matter, Physical Review Letters, 92 (2004) 054302.

[59] E. I. Corwin, H. M. Jaeger, S. R. Nagel, Structural signature of jamming in granular media, Nature, 435 (2005) 1075-1078.

[60] C. S. O'Hern, S. A. Langer, A. J. Liu, S. R. Nagel, Force distributions near jamming and glass transitions, Physical Review Letters, 86 (2001) 111-114.

[61] X. Wang, H. P. Zhu, S. Luding, A. B. Yu, Regime transitions of granular flow in a shear cell: A micromechanical study, Physical Review E, 88 (2013) 032203.

[62] H. P. Zhang, H. A. Makse, Jamming transition in emulsions and granular materials, Physical Review E, 72 (2005) 011301.

[63] M. E. Cates, J. P. Wittmer, J. P. Bouchaud, P. Claudin, Jamming, force chains, and fragile matter, Physical Review Letters, 81 (1998) 1841-1844.

[64] B. P. Tighe, A. R. T. van Eerd, T. J. H. Vlugt, Entropy maximization in the force network ensemble for granular solids, Physical Review Letters, 100 (2008) 238001.

[65] F. Radjai, D. E. Wolf, M. Jean, J. J. Moreau, Bimodal character of stress transmission in granular packings, Physical Review Letters, 80 (1998) 61-64.

[66] F. Radjai, S. Roux, J. J. Moreau, Contact forces in a granular packing, Chaos: An Interdisciplinary Journal of Nonlinear Science, 9 (1999) 544-550.

[67] D. Walker, A. Tordesillas, C. Thornton, R. Behringer, J. Zhang, J. Peters, Percolating contact subnetworks on the edge of isostaticity, Granular Matter, 13 (2011) 233-240.

[68] D. Bi, J. Zhang, B. Chakraborty, R. P. Behringer, Jamming by shear, Nature, 480 (2011) 355-358.

[69] C. H. Liu, S. R. Nagel, D. A. Schecter, S. N. Coppersmith, S. Majumdar, O. Narayan, T. A. Witten, Force fluctuations in bead packs, Science, 269 (1995) 513-515.

[70] D. M. Mueth, H. M. Jaeger, S. R. Nagel, Force distribution in a granular medium, Physical Review E, 57 (1998) 3164-3169.

[71] D. L. Blair, N. W. Mueggenburg, A. H. Marshall, H. M. Jaeger, S. R. Nagel, Force distributions in three-dimensional granular assemblies: Effects of packing order and interparticle friction, Physical Review E, 63 (2001) 041304.

[72] F. Radjai, M. Jean, J. J. Moreau, S. Roux, Force distributions in dense two-dimensional granular systems, Physical Review Letters, 77 (1996) 274-277.

[73] J. Zhou, S. Long, Q. Wang, A. D. Dinsmore, Measurement of forces inside a three-dimensional pile of frictionless droplets, Science, 312 (2006) 1631-1633.

[74] C. S. O'Hern, S. A. Langer, A. J. Liu, S. R. Nagel, Random packings of frictionless particles, Physical Review Letters, 88 (2002) 075507.

[75] A. R. T. van Eerd, W. G. Ellenbroek, M. van Hecke, J. H. Snoeijer, T. J. H. Vlugt, Tail of the contact force distribution in static granular materials, Physical Review E, 75 (2007) 060302.

[76] S. N. Coppersmith, C. h. Liu, S. Majumdar, O. Narayan, T. A. Witten, Model for force fluctuations in bead packs, Physical Review E, 53 (1996) 4673-4685.

[77] A. H. W. Ngan, Mechanical analog of temperature for the description of force distribution in static granular packings, Physical Review E, 68 (2003) 011301.

[78] R. D. Mindlin, Compliance of elastic bodies in contact, Journal of Applied Mechanics, 16 (1949) 259-268.

[79] K. L. Johnson, K. L. Johnson, Contact mechanics, Cambridge University Press 1987.

[80] R. Arévalo, I. Zuriguel, D. Maza, Topology of the force network in the jamming transition of an isotropically compressed granular packing, Physical Review E, 81 (2010) 041302.

[81] J. F. Peters, M. Muthuswamy, J. Wibowo, A. Tordesillas, Characterization of force chains in granular material, Physical Review E, 72 (2005) 041307.

[82] K. W. Desmond, P. J. Young, D. Chen, E. R. Weeks, Experimental study of forces between quasi-two-dimensional emulsion droplets near jamming, Soft Matter, 9 (2013) 3424-3436.

[83] L. Zhang, Y. Wang, J. Zhang, Force-chain distributions in granular systems, Physical Review E, 89 (2014) 012203.

[84] A. Tordesillas, D. M. Walker, G. Froyland, J. Zhang, R. P. Behringer, Transition dynamics and magic-number-like behavior of frictional granular clusters, Physical Review E, 86 (2012) 011306.

[85] R. Barrow, J. Yang, R. Dave, R. Pfeffer, Dry-mixing of sub-micron b and $BaCrO_4$ particles for use in a time delay composition, SAFE Journal, 35 (2007) 7-13.

[86] J. Scicolone, A. Mujumdar, S. Sundaresan, R. N. Davé, Environmentally benign dry mechanical mixing of nano-particles using magnetically assisted impaction mixing process, Powder Technology, 209 (2011) 138-146.

[87] N. L. Bars, P. Levitz, A. Messier, M. Francois, H. Van Damme, Deagglomeration and dispersion of barium titanate and alumina powders in an organic medium, Journal of Colloid and Interface Science, 175 (1995) 400-410.

[88] L. W. Chu, K. N. Prakash, M.-T. Tsai, I. N. Lin, Dispersion of nano-sized batio3 powders in nonaqueous suspension with phosphate ester and their applications for mlcc, Journal of the European Ceramic Society, 28 (2008) 1205-1212.

[89] P. V. Danckwerts, The definition and measurement of some characteristics of mixtures, Applied Scientific Research, Section A, 3 (1952) 279-296.

[90] C. Y. Wu, S. Watano, R. N. Davé, Magnetically enhanced powder discharge from storage under high consolidation, Powder Handling and Processing, 10 (2008) 357-361.

[91] R. Pfeffer, R. N. Dave, D. Wei, M. Ramlakhan, Synthesis of engineered particulates with tailored properties using dry particle coating, Powder Technology, 117 (2001) 40-67.

[92] L. J. Jallo, C. Ghoroi, L. Gurumurthy, U. Patel, R. N. Davé, Improvement of flow and bulk density of pharmaceutical powders using surface modification, International Journal of Pharmaceutics, 423 (2012) 213-225.

[93] Y. Tsuji, T. Kawaguchi, T. Tanaka, Discrete particle simulation of two-dimensional fluidized bed, Powder Technology, 77 (1993) 79-87.

[94] T. Mikami, H. Kamiya, M. Horio, Numerical simulation of cohesive powder behavior in a fluidized bed, Chemical Engineering Science, 53 (1998) 1927-1940.

[95] R. Balevičius, A. Džiugys, R. Kačianauskas, Discrete element method and its application to the analysis of penetration into granular media, Journal of Civil Engineering and Management, 10 (2004) 3-14.

[96] Y. Muguruma, T. Tanaka, Y. Tsuji, Numerical simulation of particulate flow with liquid bridge between particles (simulation of centrifugal tumbling granulator), Powder Technology, 109 (2000) 49-57.

[97] Y. Song, R. Turton, Study of the effect of liquid bridges on the dynamic behavior of two colliding tablets using DEM, Powder Technology, 178 (2007) 99-108.

[98] G. Lian, C. Thornton, M. J. Adams, Discrete particle simulation of agglomerate impact coalescence, Chemical Engineering Science, 53 (1998) 3381-3391.

[99] B. K. Mishra, C. Thornton, Impact breakage of particle agglomerates, International Journal of Mineral Processing, 61 (2001) 225-239.

[100] L. Liu, K. D. Kafui, C. Thornton, Impact breakage of spherical, cuboidal and cylindrical agglomerates, Powder Technology, 199 (2010) 189-196.

[101] R. Moreno-Atanasio, M. Ghadiri, Mechanistic analysis and computer simulation of impact breakage of agglomerates: Effect of surface energy, Chemical Engineering Science, 61 (2006) 2476-2481.

[102] L. Kempton, D. Pinson, S. Chew, P. Zulli, A. Yu, Simulation of macroscopic deformation using a sub-particle DEM approach, Powder Technology, 223 (2012) 19-26.

[103] G. Liu, S. Li, Q. Yao, A JKR-based dynamic model for the impact of micro-particle with a flat surface, Powder Technology, 207 (2011) 215-223.

[104] C. Thornton, K. K. Yin, Impact of elastic spheres with and without adhesion, Powder Technology, 65 (1991) 153-166.

[105] C. Thornton, Interparticle sliding in the presence of adhesion, Journal of Physics D: Applied Physics, 24 (1991) 1942-1946.

[106] A. R. Savkoor, G. A. D. Briggs, The effect of tangential force on the contact of elastic solids in adhesion, Proceedings of the Royal Society of London. A. Mathematical and Physical Sciences, 356 (1977) 103-114.

[107] M. Pasha, C. Hare, A. Hassanpour, M. Ghadiri, Analysis of ball indentation on cohesive powder beds using distinct element modelling, Powder Technology, 233 (2013) 80-90.

[108] C. Y. Wu, L. Y. Li, C. Thornton, Energy dissipation during normal impact of elastic and elastic–plastic spheres, International Journal of Impact Engineering, 32 (2005) 593-604.

[109] I. M. Hutchings, Energy absorbed by elastic waves during plastic impact, Journal of Physics D: Applied Physics, 12 (1979) 1819.

[110] N. V. Brilliantov, N. Albers, F. Spahn, T. Pöschel, Collision dynamics of granular particles with adhesion, Physical Review E, 76 (2007) 051302.

[111] N. Albers, F. Spahn, The influence of particle adhesion on the stability of agglomerates in saturn's rings, Icarus, 181 (2006) 292-301.

[112] D. Antypov, J. A. Elliott, B. C. Hancock, Effect of particle size on energy dissipation in viscoelastic granular collisions, Physical Review E, 84 (2011) 021303.

[113] R. Moreno-Atanasio, Energy dissipation in agglomerates during normal impact, Powder Technology, 223 (2012) 12-18.

[114] D. Antypov, J. A. Elliott, On an analytical solution for the damped hertzian spring, EPL (Europhysics Letters), 94 (2011) 50004.

[115] N. V. Brilliantov, T. Pöschel, Rolling friction of a viscous sphere on a hard plane, EPL (Europhysics Letters), 42 (1998) 511-516.

[116] D. Tabor, The mechanism of rolling friction. Ii. The elastic range, Proceedings of the Royal Society of London. Series A. Mathematical and Physical Sciences, 229 (1955) 198-220.

[117] I. G. Goryacheva, Contact mechanics in tribology, Springer1998.

[118] Y. C. Zhou, B. D. Wright, R. Y. Yang, B. H. Xu, A. B. Yu, Rolling friction in the dynamic simulation of sandpile formation, Physica A: Statistical Mechanics and its Applications, 269 (1999) 536-553.

[119] J. Ai, J. F. Chen, J. M. Rotter, J. Y. Ooi, Assessment of rolling resistance models in discrete element simulations, Powder Technology, 206 (2011) 269-282.

[120] L. S. Lu, S.-S. Hsiau, Mixing in vibrated granular beds with the effect of electrostatic force, Powder Technology, 160 (2005) 170-179.

[121] E. W. C. Lim, Y. Zhang, C. H. Wang, Effects of an electrostatic field in pneumatic conveying of granular materials through inclined and vertical pipes, Chemical Engineering Science, 61 (2006) 7889-7908.

[122] E. N. Nwose, C. Pei, C. Y. Wu, Modelling die filling with charged particles using DEM/CFD, Particuology, 10 (2012) 229-235.

[123] R. N. Dave, C. Y. Wu, B. Chaudhuri, S. Watano, Magnetically mediated flow enhancement for controlled powder discharge of cohesive powders, Powder Technology, 112 (2000) 111-125.

[124] W. Wang, R. Dave, B. Khusid, R. Pfeffer, Discrete element simulation of magnetically assisted impaction coating process, 2003 AIChE Annual Meeting San Francisco, CA Nov, (2003) 16-21.

[125] Duane E. Roller, R. Blum, Electricity, magnetism and light, Holden Day, San Francisco, (1981).

[126] D. J. Evans, S. Murad, Singularity free algorithm for molecular dynamics simulation of rigid polyatomics, Molecular Physics, 34 (1977) 327-331.

[127] D. Wei, R. Dave, R. Pfeffer, Mixing and characterization of nanosized powders: An assessment of different techniques, Journal of Nanoparticle Research, 4 (2002) 21-41.

[128] P. Ammendola, R. Chirone, Aeration and mixing behaviours of nano-sized powders under sound vibration, Powder Technology, 201 (2010) 49-56.

[129] D. Lepek, J. M. Valverde, R. Pfeffer, R. N. Dave, Enhanced nanofluidization by alternating electric fields, AIChE Journal, 56 (2010) 54-65.

[130] Q. Yu, R. N. Dave, C. Zhu, J. A. Quevedo, R. Pfeffer, Enhanced fluidization of nanoparticles in an oscillating magnetic field, AIChE Journal, 51 (2005) 1971-1979.

[131] R. Y. Yang, A. B. Yu, S. K. Choi, M. S. Coates, H. K. Chan, Agglomeration of fine particles subjected to centripetal compaction, Powder Technology, 184 (2008) 122-129.

[132] C. Thornton, M. T. Ciomocos, M. J. Adams, Numerical simulations of diametrical compression tests on agglomerates, Powder Technology, 140 (2004) 258-267.

[133] J. Subero, Z. Ning, M. Ghadiri, C. Thornton, Effect of interface energy on the impact strength of agglomerates, Powder Technology, 105 (1999) 66-73.

[134] M. Poux, P. Fayolle, J. Bertrand, D. Bridoux, J. Bousquet, Powder mixing: Some practical rules applied to agitated systems, Powder Technology, 68 (1991) 213-234.

[135] A. U. Vanarase, F. J. Muzzio, Effect of operating conditions and design parameters in a continuous powder mixer, Powder Technology, 208 (2011) 26-36.

[136] M. Lemieux, G. Léonard, J. Doucet, L. A. Leclaire, F. Viens, J. Chaouki, F. Bertrand, Large-scale numerical investigation of solids mixing in a v-blender using the discrete element method, Powder Technology, 181 (2008) 205-216.

[137] A. Mehrotra, M. Llusa, A. Faqih, M. Levin, F. J. Muzzio, Influence of shear intensity and total shear on properties of blends and tablets of lactose and cellulose lubricated with magnesium stearate, International Journal of Pharmaceutics, 336 (2007) 284-291.

[138] F. J. Muzzio, A. Alexander, C. Goodridge, E. Shen, T. Shinbrot, K. Manjunath, S. Dhodapkar, K. Jacob, Solids mixing, Handbook of industrial mixing, John Wiley & Sons, Inc.2004, pp. 887-985.

[139] P. M. C. Lacey, Developments in the theory of particle mixing, Journal of Applied Chemistry, 4 (1954) 257-268.

[140] I. Figueroa, H. Li, J. McCarthy, Predicting the impact of adhesive forces on particle mixing and segregation, Powder Technology, 195 (2009) 203-212.

[141] P. E. Arratia, N.-h. Duong, F. J. Muzzio, P. Godbole, S. Reynolds, A study of the mixing and segregation mechanisms in the bohle tote blender via DEM simulations, Powder Technology, 164 (2006) 50-57.

[142] M. J.J, Micro-modeling of cohesive mixing processes, Powder Technology, 138 (2003) 63-67.

[143] M. P. Mullarney, L. E. Beach, R. N. Davé, B. A. Langdon, M. Polizzi, D. O. Blackwood, Applying dry powder coatings to pharmaceutical powders using a comil for improving powder flow and bulk density, Powder Technology, 212 (2011) 397-402.

[144] S. Chattoraj, L. Shi, C. C. Sun, Profoundly improving flow properties of a cohesive cellulose powder by surface coating with nano-silica through comilling, Journal of Pharmaceutical Sciences, 100 (2011) 4943-4952.

[145] Z. Huang, J. V. Scicolone, L. Gurumuthy, R. N. Davé, Flow and bulk density enhancements of pharmaceutical powders using a conical screen mill: A continuous dry coating device, Chemical Engineering Science, 125 (2015) 209-224.

[146] Q. Zhou, L. Shi, W. Marinaro, Q. Lu, C. C. Sun, Improving manufacturability of an ibuprofen powder blend by surface coating with silica nanoparticles, Powder Technology, 249 (2013) 290-296.

[147] A. K. Samanta, K. Y. Ng, P. W. S. Heng, Cone milling of compacted flakes: Process parameter selection by adopting the minimal fines approach, International Journal of Pharmaceutics, 422 (2012) 17-23.

[148] C. O'Sullivan, L. Cui, Micromechanics of granular material response during load reversals: Combined DEM and experimental study, Powder Technology, 193 (2009) 289-302.

[149] M. Marigo, D. L. Cairns, M. Davies, A. Ingram, E. H. Stitt, A numerical comparison of mixing efficiencies of solids in a cylindrical vessel subject to a range of motions, Powder Technology, 217 (2012) 540-547.

[150] P. M. Portillo, M. G. Ierapetritou, F. J. Muzzio, Characterization of continuous convective powder mixing processes, Powder Technology, 182 (2008) 368-378.

[151] Y. Gao, A. Vanarase, F. Muzzio, M. Ierapetritou, Characterizing continuous powder mixing using residence time distribution, Chemical Engineering Science, 66 (2011) 417-425.

[152] P. M. Portillo, M. G. Ierapetritou, F. J. Muzzio, Effects of rotation rate, mixing angle, and cohesion in two continuous powder mixers-a statistical approach, Powder Technology, 194 (2009) 217-227.

[153] A. T. Harris, J. F. Davidson, R. B. Thorpe, Particle residence time distributions in circulating fluidised beds, Chemical Engineering Science, 58 (2003) 2181-2202.

[154] J. T. Adeosun, A. Lawal, Numerical and experimental studies of mixing characteristics in a T-junction microchannel using residence-time distribution, Chemical Engineering Science, 64 (2009) 2422-2432.

[155] P. V. Danckwerts, Continuous flow systems: Distribution of residence times, Chemical Engineering Science, 2 (1953) 1-13.

[156] E. L. Paul, V. A. Atiemo-Obeng, S. M. Kresta, Handbook of industrial mixing - science and practice, John Wiley & Sons, 2003.

[157] B. Nauman, Residence time theory, Industrial & Engineering Chemistry Research, 47 (2008) 3752-3766.

[158] J. V. Scicolone, R. N. Davé, Improved flowability and packing density of api powders via dry coating for continuos manufacturing of direct compressed tablets, presented at the Twenty-Seventh International Forum Process Analytical Chemistry - IFPAC,Baltimore, Maryland, USA, (2013).

[159] B. N. J. Persson, Adhesion between elastic bodies with randomly rough surfaces, Physical Review Letters, 89 (2002) 245502.

[160] S. N. Ramakrishna, P. C. Nalam, L. Y. Clasohm, N. D. Spencer, Study of adhesion and friction properties on a nanoparticle gradient surface: Transition from JKR to dmt contact mechanics, Langmuir, 29 (2012) 175-182.

[161] S. N. Ramakrishna, R. M. Espinosa-Marzal, V. V. Naik, P. C. Nalam, N. D. Spencer, Adhesion and friction properties of polymer brushes on rough surfaces: A gradient approach, Langmuir, 29 (2013) 15251-15259.

[162] P. Prokopovich, S. Perni, Multiasperity contact adhesion model for universal asperity height and radius of curvature distributions, Langmuir, 26 (2010) 17028-17036.

[163] A. G. Peressadko, N. Hosoda, B. N. J. Persson, Influence of surface roughness on adhesion between elastic bodies, Physical Review Letters, 95 (2005) 124301.

[164] R. Pohrt, V. L. Popov, Contact stiffness of randomly rough surfaces, Scientific Report, 3 (2013).

[165] Y. Chen, M. A. S. Quintanilla, J. Yang, J. M. Valverde, R. N. Dave, Pull-off force of coated fine powders under small consolidation, Physical Review E, 79 (2009) 041305.

[166] A. Castellanos, The relationship between attractive interparticle forces and bulk behaviour in dry and uncharged fine powders, Advances in Physics, 54 (2005) 263-376.

[167] M. Quintanilla, A. Castellanos, J. Valverde, Correlation between bulk stresses and interparticle contact forces in fine powders, Physical Review E, 64 (2001) 031301.

[168] J. Plagge, C. Heussinger, Melting a granular glass by cooling, Physical Review Letters, 110 (2013) 078001.

[169] R. W. Carpick, D. F. Ogletree, M. Salmeron, A general equation for fitting contact area and friction vs load measurements, Journal of Colloid and Interface Science, 211 (1999) 395-400.

[170] K. L. Johnson, Adhesion and friction between a smooth elastic spherical asperity and a plane surface, Proceedings of the Royal Society of London. A., 453 (1997) 163-179.

[171] M. A. Lantz, S. J. O'Shea, M. E. Welland, K. L. Johnson, Atomic-force-microscope study of contact area and friction on nbse2, Physical Review B, 55 (1997) 10776-10785.

[172] Y. Mo, K. T. Turner, I. Szlufarska, Friction laws at the nanoscale, Nature, 457 (2009) 1116-1119.

[173] M. A. S. Quintanilla, J. M. Valverde, A. Castellanos, Adhesion force between fine particles with controlled surface properties, AIChE Journal, 52 (2006) 1715-1728.